# Phonon Anharmonicity at the Limits of Perturbation Theory

Thesis by
Yang Shen

In Partial Fulfillment of the Requirements for the
Degree of
Doctor of Philosophy

CALIFORNIA INSTITUTE OF TECHNOLOGY
Pasadena, California

2020
Defended May 27, 2020

*To my beloved mother.*

# ACKNOWLEDGEMENTS

The year of 2020 is one of the turning points in my life, especially during the pandemic. At this moment, I would like to express my gratitude to all the wonderful people I have met during the past six years at Caltech.

First of all, I want to thank my research advisor, Brent Fultz. I have been so fortunate to have the opportunity to work with him for over five years. Brent has provided enormous encouragement, guidance, patience and support for my study. He also gives me great support during the COVID-19 pandemic. This thesis would never have been completed without his mentorship.

I appreciate the support from my committee: Professors Austin Minnich, Marco Bernardi and Olle Hellman. Their expertise and insights in physics and materials science are very valuable and greatly enrich my work. In particular, I thank Olle for developing this amazing sTDEP method, which is the main computational tool I have been using in my research.

I would like to thank the former and current members of the Fultz group, who have been a constant source of thoughts and support: Fred Yang, Claire Saunders, Camille Bernal, Dennis Kim, Cullen Quine, Stefan Lohaus, Pedro Guzman, Channing Ahn, Hillary Smith, Jiao Lin, Chen Li and Heng Yang. They are so easy-going and have lots of passion. Special thanks to Fred, who was my office mate. He gave me the initiation class on computational physics, and helped me a lot on my academic projects and job search. I also want to thank: Claire for her constant support on the NaBr project and the folding back codes we wrote together, handling the compiling issues on NERSC, and her great patience during our discussions; Camille for her help on the NaBr project and the preparation of my thesis presentation; and both of them for delivering the food and helping me after my surgery.

I wish to acknowledge the generous help and support of our collaborators at Oak Ridge National Laboratory: Mike Manley and Doug Abernathy. They made our inelastic neutron scattering experiments possible. Mike also gave me helpful advice on my career path.

Finally, nothing I have accomplished would have been possible without the unconditional love and support from my parents and my elder brother, and my fiancée and her parents. My fiancée and I have known each other for ten years, but for the most

part, we lived in different cities, or even different countries. We have already been through these years together and soon I will hold her hand forever. Ying, thank you.

# ABSTRACT

Phonons, as the building blocks of solid-state physics, have been studied for almost one hundred years. The harmonic model is helpful when introducing the concepts and offering a basic physics picture of atomic vibrations. However, there are many properties that cannot be explained by the harmonic model or its extension to the quasiharmonic approximation (QHA), which ignores the pure temperature dependence of phonon frequencies. The rapid development of materials science requests a deep understanding of the phonon behaviors at elevated temperatures, where phonon-phonon interactions, as a main source of phonon anharmonicity, account for a number of abnormal phonon behaviors and the thermodynamical properties of many materials. In this thesis, I present the phonon anharmonicity in metals of Pd and Pt, the metallic compound $FeGe_2$, and the polar material NaBr to show the limitation of the harmonic or QH model and the importance of taking anharmonic effects into consideration.

Inelastic neutron scattering (INS) was used to measure the phonon density of states (DOS) in fcc Pd and Pt metal at temperatures from 7 K to 1576 K. Both phonon-phonon interactions and electron-phonon interactions were calculated by methods based on density functional theory (DFT) and were consistent with the measured shifts and broadenings of phonons with temperature. Contributions to the entropy from phonons and electrons were assessed and summed to obtain excellent agreement with prior calorimetric data. The QH entropy is positive for both phonons and electrons but larger for phonons. The anharmonic phonon entropy is negative in Pt, but in Pd it changes from positive to negative with increasing temperature.

Phonon dispersions in a single crystal of $FeGe_2$ with the C16 structure at 300, 500, and 635 K were measured by INS. Phonon DOS were also measured on polycrystalline $FeGe_2$ from 325 to 1050 K, and the Fe partial DOS was obtained from polycrystalline $^{57}FeGe_2$ at 300 K using nuclear resonant inelastic X-ray scattering (NRIXS). The dominant feature in the temperature dependence of the phonon spectrum is thermal broadening of high-energy modes. The energy shifts of the low- and high-energy parts of the spectrum were almost the same. DFT calculations performed with the QHA gave results in moderate agreement with the experimental thermal energy shifts, although the isobaric Grüneisen parameter calculated from the quasiharmonic model was smaller than that from measurements. The thermal broadening of the phonon spectrum and dispersions, especially at high energies, indicates a cubic anharmonicity to second order that should also induce phonon shifts. There are cancellations of different anharmonic contributions to energy shifts, giving average phonon shifts in moderate agreement to calculations with the QHA. The different parts of the large phonon contribution to the entropy are separated for $FeGe_2$, showing modest but interpretable anharmonic contributions.

All phonons in a single crystal of NaBr were measured by INS at temperatures of 10, 300 and 700 K. Even at 300 K the phonons, especially the longitudinal optical (LO) phonons, showed large shifts in frequencies, and showed large broadenings in energy owing to anharmonicity. The QHA was an unqualified failure for predicting the temperature dependence of phonon frequencies, even at 300 K, and it predicted a thermal expansion that was in error by a factor of four. *Ab initio* computations that included both anharmonicity and quasiharmonicity successfully predicted both the temperature dependence of phonons and the large thermal expansion of NaBr. The frequencies of LO phonon modes decrease significantly with temperature owing to the real part of the phonon self-energy from explicit anharmonicity. The origin of the large cubic anharmonicity was identified with nearest-neighbor Na-Br bonds. Anharmonicity is not a small correction to the QHA predictions of thermal expansion and thermal phonon shifts, but anharmonicity dominates the behavior.

New spectral features were found in phonon dispersions of NaBr at 300 K. *Ab initio* calculations based on anharmonic perturbation theory also showed these spectral features as “many-body effects.” Their physical origin is better elucidated with a Langevin model, similar that in recent work in optomechanics. The transverse optic (TO) part of the new features originates from phonon intermodulation between the transverse acoustic (TA) and TO phonons. The LO spectral features originate from three-phonon coupling between the TA modes and the TO lattice modes.

# PUBLISHED CONTENT AND CONTRIBUTIONS

[1] Coherent Sideband Quasiparticles Created from Anharmonic Phonons in NaBr. *In Preparation.*
Y. S conceptualized the project, conducted the experiment, reduced and analyzed the data, performed all calculations, and conducted the writing of the manuscript.

[2] The Anharmonic Origin of the Giant Thermal Expansion of NaBr. *Submitted to PRL, under review.*
Y. S conceptualized the project, conducted the experiment, reduced and analyzed the data, performed all calculations, and conducted the writing of the manuscript.

[3] H. L. Smith, Y. Shen, D. S. Kim, F. C. Yang, C. P. Adams, C. W. Li, D. L. Abernathy, M. B. Stone, and B. Fultz. "Temperature dependence of phonons in $FeGe_2$". *Physical Review Materials* **2,** 103602 (2018). DOI: 10.1103/PhysRevMaterials.2.103602.
Y. S, as the co-first author, analyzed the experimental data, performed the calculations, analyzed the physics properties of the material, and participated in the writing of the manuscript.

[4] Y. Shen, C. W. Li, X. Tang, H. L. Smith, and B. Fultz. "Phonon anharmonicity and components of the entropy in palladium and platinum". *Physical Review B* **93,** 214303 (2016). DOI: 10.1103/PhysRevB.93.214303.
Y. S, as the co-first author, analyzed the experimental data, performed part of the calculations, and participated in the writing of the manuscript.

# TABLE OF CONTENTS

# LIST OF ILLUSTRATIONS

# LIST OF TABLES

## *Chapter 1*

# INTRODUCTION

### 1.1 Introduction to Phonons

Phonons, as building blocks of solid-state physics, have been studied for almost one hundred years[19, 20]. Phonons describe the states of atomic motions. With mutual interactions between atoms, local motional excitations lead to collective vibrations of the whole solid[21]. It is therefore appropriate to use normal coordinates for the mathematical description of atomic dynamics. The lattice vibrations can be readily quantized in this new representation; the associated quanta are elementary excitations called *phonons*.

### 1.2 Vibrational Thermodynamics of Solids

The basic model starts with an infinitely repeating lattice, in which the atoms are vibrating around their equilibrium positions. The mass of an atom is in its point-like nucleus, and the forces between nuclei are transmitted through lightweight electrons, which are typically assumed to respond instantly to nuclear displacements[22] (Born–Oppenheimer approximation).

Since most of the atom mass is in the nucleus, for lattice dynamics the Hamiltonian for nuclear motions in a crystal can be taken as

$$\mathcal{H} = \sum_{i} \frac{\mathbf{p}_i^2}{2m_i} + \Phi \ . \tag{1.1}$$

The potential energy, $\Phi$, can be expanded in powers of the atomic displacements from their equilibrium positions as

$$\Phi = \Phi_0 + \cancel{\sum_{\alpha} \Phi_i^{\alpha} u_i^{\alpha}} + \sum_{\alpha\beta} \Phi_{ij}^{\alpha\beta} u_i^{\alpha} u_j^{\beta} + \frac{1}{3!} \sum_{ijk} \sum_{\alpha\beta\gamma} \Phi_{ijk}^{\alpha\beta\gamma} u_i^{\alpha} u_j^{\beta} u_k^{\gamma} + \dots \ , \tag{1.2}$$

where the coefficients of the Taylor series are the derivatives of the potential with respect to the displacements ($\mathbf{u} = \sum_{\alpha=x,y,z} u^{\alpha}\hat{\mathbf{e}}_{\alpha}$):

$$\Phi_i^{\alpha} = \left.\frac{\partial \Phi}{\partial u_i^{\alpha}}\right|_0 = 0 \tag{1.3}$$

$$\Phi_{ij}^{\alpha\beta} = \left.\frac{\partial^2 \Phi}{\partial u_i^{\alpha}\partial u_j^{\beta}}\right|_0 \tag{1.4}$$

$$\Phi_{ijk}^{\alpha\beta\gamma} = \left.\frac{\partial^3 \Phi}{\partial u_i^{\alpha}\partial u_j^{\beta}\partial u_k^{\gamma}}\right|_0 \tag{1.5}$$

$$\cdots$$

### Harmonic Approximation

If the expansion is terminated after the first non-vanishing (quadratic) term, for each atom $\kappa$ in the unit cell $l$, it can be solved by the wave function of [23]

$$\mathbf{u}_i = \frac{1}{\sqrt{m_i}} \sum_{\mathbf{q}} A_{\mathbf{q}} \boldsymbol{\epsilon}_{\mathbf{q}}^{i} e^{i(\mathbf{q}\cdot\mathbf{R}-\omega t)} \ . \tag{1.6}$$

Here the displacements are expressed as a sum of normal modes, each with wave vector $\mathbf{q}$ and frequency $\omega$. $A_{\mathbf{q}}$ is the normal mode amplitude, and $\boldsymbol{\epsilon}$ is a polarization vector determined by

$$\omega_{\mathbf{q}}^2 \boldsymbol{\epsilon}_{\mathbf{q}} = \boldsymbol{\Phi}(\mathbf{q}) \boldsymbol{\epsilon}_{\mathbf{q}} \ , \tag{1.7}$$

where

$$\boldsymbol{\Phi}(\mathbf{q}) = \begin{pmatrix} \boldsymbol{\Phi}_{11}(\mathbf{q}) & \cdots & \boldsymbol{\Phi}_{N1}(\mathbf{q}) \\ \vdots & \ddots & \vdots \\ \boldsymbol{\Phi}_{1N}(\mathbf{q}) & \cdots & \boldsymbol{\Phi}_{NN}(\mathbf{q}) \end{pmatrix} \tag{1.8}$$

is the dynamical matrix. Each sub-matrix $\boldsymbol{\Phi}_{ij}(\mathbf{q}) = \sum_{\mathbf{R}} \frac{\boldsymbol{\Phi}_{ij}(\mathbf{R})}{\sqrt{m_i m_j}} e^{i\mathbf{q}\cdot\mathbf{R}}$ is the Fourier transform of the second-order force-constant matrix. It can be shown that the dynamical matrix is Hermitian, so the $\omega^2$ are real as the dynamical matrix is fully diagonalizable for any $q$. The eigenvectors ($\boldsymbol{\epsilon}_{\mathbf{q}j}$) and eigenvalues ($\omega_{\mathbf{q}j}^2$) of the dynamical matrix evaluated at a particular wavevector $\mathbf{q}$ then correspond to the eigenmodes of vibration of the crystal for that wavevector. Owing to the periodicity of the reciprocal lattice, it is convenient to limit the solution to only vectors $\mathbf{q}$ in the first Brillouin zone. The phonon density of states (DOS) is then

$$g_s(\omega) = \frac{(2\pi)^3}{V} \int_{\mathrm{BZ}} \delta(\omega - \omega_{\mathbf{q}j}) d\mathbf{q} \ . \tag{1.9}$$

Phonons are bosons, and their contribution to the Helmholtz free energy of the material is given by

$$F_{\mathrm{ph}} = -k_B T \ln Z = \sum_{\mathbf{q}j} \frac{\hbar\omega_{\mathbf{q}j}}{2} + k_B T \ln\left(1 - \exp\left(-\frac{\hbar\omega_{\mathbf{q}j}}{k_B T}\right)\right) \ . \tag{1.10}$$

The vibrational free energy and all other thermodynamic properties in the harmonic approximation can be determined from the phonon frequencies calculated at the equilibrium volume $V_0$. Two computational approaches usually used, 1) the supercell method, and 2) density functional perturbation theory (DFPT).

The harmonic potential is a good approximation at low energy (temperature), but it becomes inadequate as the temperature increases. There are several limitations of the harmonic approximation:

- no thermal expansion as $V$ is a constant ($V \equiv V_0$),
- phonons are independent,
- infinite phonon lifetime,
- infinite thermal conductivity,
- no effects of $T$ outside of populating fixed phonon modes

We will see how these limitations are overcame in this thesis, and the new and exciting physics that lies beyond the harmonic model.

### Quasiharmonic Approximation (QHA)

As an ‘extension’ of the harmonic approximation, the QHA introduces an explicit dependence of phonon frequencies on volume into the Helmholtz free energy as

$$F^{\mathrm{QHA}}(T,V) = U_0(V) + \sum_{\mathbf{q},j} \left\{ \frac{\hbar\omega_{\mathbf{q},j}(V)}{2} + k_{\mathrm{B}} T \ln\left[1 - \exp\left(-\frac{\hbar\omega_{\mathbf{q},j}(V)}{k_{\mathrm{B}} T}\right)\right]\right\} \ , \tag{1.11}$$

where $U_0(V)$ is the ground-state internal energy without any vibrational contribution and the term $k_{\mathrm{B}} \ln[\ldots]$ includes the entropy that depends on volume through the individual phonon frequencies $\omega_{\mathbf{q},j} = \omega_{\mathbf{q},j}(V)$ (for the $j$-th phonon branch at wavevector $\mathbf{q}$). The equilibrium volume at a given temperature $T$ was obtained by minimizing $F^{\mathrm{QHA}}(T,V)$ with respect to volume $V$, keeping $T$ as a fixed parameter. The QHA offers thermal expansion as a parameter to minimize free energy, so the phonon frequency will no longer be the same as that at 0 K. However, in the QHA, all phonons calculations are still performed with a harmonic potential energy.

### Anharmonic Phonons

Within the harmonic or quasiharmonic approximation, phonons are non-interacting elementary excitations, and therefore have infinite lifetimes. Including higher terms (anharmonic terms) in the expansion of the potential means that harmonic phonons are no longer true eigenstates of the system. This leads to interactions between phonons. As a result, a phonon from a given state will decay into other phonons after a finite time. Their frequencies will also be shifted[24].

As we discussed before, in perturbation theory, the crystal potential is expanded as a power of displacement and the Hamiltonian may be written as[24]:

$$\mathcal{H} = \mathcal{H}_0 + \lambda\mathcal{H}_3 + \lambda^2\mathcal{H}_4 + \lambda^3\mathcal{H}_5 + \dots \tag{1.12}$$

where $\mathcal{H}_0$ is the harmonic Hamiltonian and $\mathcal{H}_3, \mathcal{H}_4, \mathcal{H}_5 \dots$ are the perturbation terms involving three, four, five ... interacting phonons. The simplest case is the three-phonon interaction where a phonon decays to form two other phonons and vice-versa.

In three-phonon processes the number of phonons changes. There are four basic processes[24]: absorption of a phonon with formation of two other phonons, absorption of two phonons with formation of another, simultaneous disappearance and simultaneous creation of three phonons. The two last possibilities clearly violate energy conservation. We must however include them in our considerations as possible virtual subprocesses of multiple-step interactions. The possible interactions are shown in Fig. 1.1. The Hamiltonian for three-phonon processes reads[24]:

$$\begin{aligned} H_3 \; &= \frac{1}{3!}\sum_{\mathbf{q}\mathbf{q}'\mathbf{q}''}\sum_{jj'j''}\frac{\hbar^{3/2}}{2^{3/2}N^{1/2}}\frac{\Phi(\mathbf{q}j,\mathbf{q}'j',\mathbf{q}''j'')}{\sqrt{\omega_{\mathbf{q}j}\omega_{\mathbf{q}'j'}\omega_{\mathbf{q}''j''}}}\delta_{\mathbf{q}+\mathbf{q}'+\mathbf{q}'',\mathbf{G}} \\ &\times (a^{\dagger}_{-\mathbf{q}j} + a_{\mathbf{q}j})(a^{\dagger}_{-\mathbf{q}'j'} + a_{\mathbf{q}'j'})(a^{\dagger}_{-\mathbf{q}''j''} + a_{\mathbf{q}''j''}) \; , \end{aligned} \tag{1.13}$$

where $\Phi(\mathbf{q}j,\mathbf{q}'j',\mathbf{q}''j'')$ is the three-phonon matrix element obtained from the cubic force constants by Fourier transformation,, $\mathbf{q}, \mathbf{q}', \mathbf{q}''$ are the wave vectors of the three phonons involved in the process and $\mathbf{G}$ is the reciprocal lattice vector. The $\delta$-function guarantees momentum conservation in these processes. The last three terms of Eq.1.13 represent the different processes of creation and annihilation of the three phonons.

Using results from many-body theory, the phonon frequencies were obtained from the dynamical matrix for the quadratic force constants, and then corrected by the

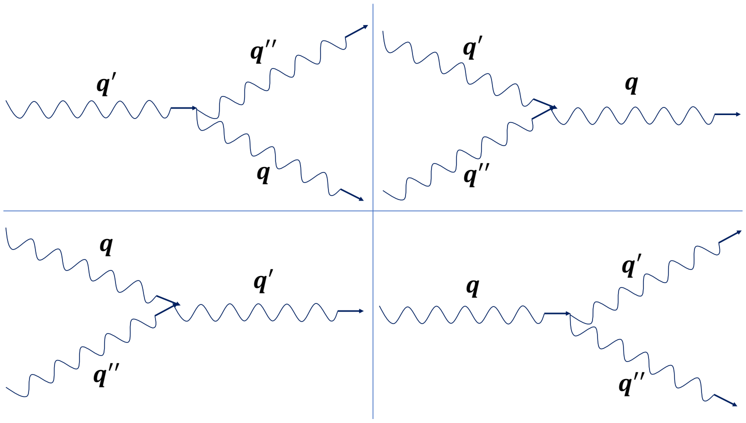

Figure 1.1: Three-phonon interaction processes that may destroy or create the phonon with wave vector **q**.

real ($\Delta$) and imaginary ($i\Gamma$) parts of the phonon self-energy. The imaginary part was calculated with the third-order force constants,

$$\Gamma_\lambda(\Omega) = \frac{\hbar\pi}{16}\sum_{\lambda'\lambda''}|\Phi_{\lambda\lambda'\lambda''}|^2\left\{(n_{\lambda'}+n_{\lambda''}+1)\times\delta(\Omega-\omega_{\lambda'}-\omega_{\lambda''})\right.$$
$$\left.+(n_{\lambda'}-n_{\lambda''})\times[\delta(\Omega-\omega_{\lambda'}+\omega_{\lambda''})-\delta(\Omega+\omega_{\lambda'}-\omega_{\lambda''})]\right\}\ , \tag{1.14}$$

where $\Omega = E/\hbar$) is the probing energy. The real part was obtained by a Kramers-Kronig transformation

$$\Delta(\Omega) = \mathcal{P}\int\frac{1}{\pi}\frac{\Gamma(\omega)}{\omega-\Omega}\mathrm{d}\omega\ . \tag{1.15}$$

Equation 1.14 is a sum over all possible three-phonon interactions, where $\Phi_{\lambda\lambda'\lambda''} \triangleq \Phi(\mathbf{q}j, \mathbf{q}'j', \mathbf{q}''j'')$, $n$ is the Bose-Einstein thermal occupation factor giving the number of phonons in each mode, and the delta functions conserve energy and momentum.

The temperature dependence of phonon frequencies are now available for more accurate calculations of vibrational thermodynamics of solids

$$F_{\mathrm{ph}}^{\mathrm{Anh}}(V,T) = \sum_{\mathbf{q},j}\left\{\frac{\hbar\omega_{\mathbf{q},j}(V,T)}{2} + k_{\mathrm{B}}T\ln\left[1-\exp\left(-\frac{\hbar\omega_{\mathbf{q},j}(V,T)}{k_{\mathrm{B}}T}\right)\right]\right\}\ . \tag{1.16}$$

### Intrinsically localized mode

An intrinsically localized mode (ILM) is another interesting vibrational phenomenon in anharmonic solids. When atoms interact with nonlinear forces, a large, local vibrational fluctuation is accompanied by a frequency shift that can stabilize the dynamics of an atom and its neighbors. The theoretical background was first investigated by Takeno, Sievers, and co-workers[25–27]. They used a classical one-dimensional monatomic chain of particles interacting by nearest-neighbor springs with harmonic and anharmonic forces plus forces from a quartic potential. With the rotating wave approximation (RWA), the lattice could sustain stationary localized vibrations when the anharmonic forces were sufficiently strong[28]. In a crystal, where the normal modes form well-defined frequency bands, these local fluctuations can develop frequencies that do not resonate with any normal modes, resulting in an ILM[29].

During the past three decades, ILMs have been investigated by simulations for various model potentials, and extended to three dimensions[30–33]. More recently, ILMs have been observed in real materials like $\alpha$-U[29], NaI[34] and PbSe[35]. They have also been reported in other systems, such as antiferromagnets[36], proteins[37] and coupled Josephson junction arrays[38]. However, the direct connection between simulations with model potentials and ILMs in real materials is largely missing. In this thesis, I introduce a new concept of intermodulation phonon sidebands (IPS) as a more general case of highly anharmonic phonon behavior. The ILM arises as one of the two sidebands. I report the observation of the upper sideband for the first time, in both inelastic neutron scattering spectra and computed phonon spectral weights of NaBr.

#### Beyond the perturbation framework

The Hamiltonian we used in Eq. 1.12 is within in the perturbation theory. What if large anharmonic terms push the system beyond the applicability of the perturbation framework? To continue, new tools should be developed, as well as new concepts. We will walk through the example of NaBr in Ch. 5 to see the exciting findings beyond perturbation theory.

## 1.3 Computational Method

To simulate anharmonic phonons by perturbation theory, O. Hellman, et al., have developed the stochastic Temperature Dependent Effective Potential (sTDEP) method[39–41].

With harmonic forces, the instantaneous position ($\mathbf{u_i}$) and velocity ($\dot{\mathbf{u}}_i$) of the $i$th atom are the sums of contributions from $3N$ normal modes

$$\mathbf{u}_i = \sum_{s=1}^{3N} \boldsymbol{\epsilon}_{is} A_{is} \sin(\omega_s t + \delta_s) \ , \tag{1.17}$$

$$\dot{\mathbf{u}}_i = \sum_{s=1}^{3N} \boldsymbol{\epsilon}_{is} A_{is} \omega_s \cos(\omega_s t + \delta_s) \ , \tag{1.18}$$

where $A_s$ is the normal mode amplitude, $\delta_s$ is the phase shift, $\omega_s$ and $\boldsymbol{\epsilon}_s$ are eigenvalue and eigenvector corresponding to mode $s$.

To obtain a set of positions and velocities that correspond to a canonical ensemble, we choose the $A_s$ and $\delta_s$ so they are normally distributed around their mean value. Each mode $s$ should contribute, on average, $k_\mathrm{B}T/2$ to the internal energy. Then

$$\langle A_{is} \rangle = \sqrt{\frac{\hbar(2n_s + 1)}{2m_i\omega_s}} \approx \frac{1}{\omega_s}\sqrt{\frac{k_\mathrm{B}T}{m_i}} \ , \tag{1.19}$$

where the approximate result is in the classical limit, $\hbar\omega \ll k_\mathrm{B}T$. The appropriate distribution of atomic positions and velocities are

$$\mathbf{u}_i = \sum_{s=1}^{3N} \boldsymbol{\epsilon}_{is} \langle A_{is} \rangle \sqrt{-2\ln\xi_1} \sin 2\pi\xi_2 \ , \tag{1.20}$$

$$\dot{\mathbf{u}}_i = \sum_{s=1}^{3N} \omega_s \boldsymbol{\epsilon}_{is} \langle A_{is} \rangle \sqrt{-2\ln\xi_1} \cos 2\pi\xi_2 \ , \tag{1.21}$$

where $\xi_n (n = 1, 2)$ represent a uniform distribution of random numbers between $(0, 1)$, which are transformed to a normal distribution using the standard Box-Muller transform. The Box-Mueller transform gives a Gaussian distribution of atom displacements, but the displaced atoms still see the full anharmonicity from DFT[40, 41].

In this procedure, the Born-Oppenheimer surface is sampled by a Monte Carlo sampling of atomic positions and momentum near equilibrium positions. By performing DFT calculations for various configurations of displaced atoms generated by a stochastic sampling of a canonical ensemble, with Cartesian displacements ($u_i^\alpha$) normally distributed around the mean thermal displacement, the forces on atoms were fitted to a model Hamiltonian

$$\hat{H} = U_0 + \sum_i \frac{\mathbf{p}_i^2}{2m_i} + \frac{1}{2!}\sum_{ij}\sum_{\alpha\beta} \Phi_{ij}^{\alpha\beta} u_i^\alpha u_j^\beta + \frac{1}{3!}\sum_{ijk}\sum_{\alpha\beta\gamma} \Phi_{ijk}^{\alpha\beta\gamma} u_i^\alpha u_j^\beta u_k^\gamma \ , \tag{1.22}$$

Here, $U_0$ is a fit parameter for the baseline of the potential energy surface. The quadratic force constants $\Phi_{ij}$ from the thermally-displaced atoms capture not only harmonic properties but also temperature-dependent nonharmonic effects, and are used to calculate phonon frequencies. The cubic force constants $\Phi_{ijk}$ capture phonon-phonon interactions (PPI) that contribute to the broadening and additional shifts of phonon modes.

In practice, we perform first-principles calculations on a temperature-volume grid covering, for example, five temperatures and five volumes. We choose the five volumes linearly spaced within ±5% around the equilibrium volumes. We iterate for 3 to 5 times until the force constants were converged.

More terms in the Taylor expansion of the energy can capture the full anharmonicity at low and high T, but this is difficult to implement.

### Experiments

So far, we have discussed different models of lattice dynamics and the corresponding computational methods. To support the theoretical work that pushes beyond the realm of phonon perturbation theory, we need experimental results. In my work, phonons were mainly measured by inelastic neutron scattering (INS) experiments[42] on powders or single crystals. The INS data were acquired with the time-of-flight Wide Angular-Range Chopper Spectrometer (ARCS) at the Spallation Neutron Source at Oak Ridge National Laboratory. Fig. 1.2 shows the structure of the ARCS instrument[43].

The technical details vary for different experimental measurements. In the following chapters, I present studies of anharmonic phonons in the metals Pd and Pt, the intermetallic compound $FeGe_2$ and the polar material NaBr. These different studies address the differences between harmonic, quasiharmonic and anharmonic phonon behaviors, showing the importance of phonon anharmonicity in the thermodynamic properties. Last but not least, I present the discovery of a new phonon branch in NaBr driven by phonon-phonon interactions. Paired with an intrinsic localized mode, this new pair of features turns out to be phonon intermodulation sidebands, a totally new concept in phonon physics that parallels recent developments in laser-cavity experiments.

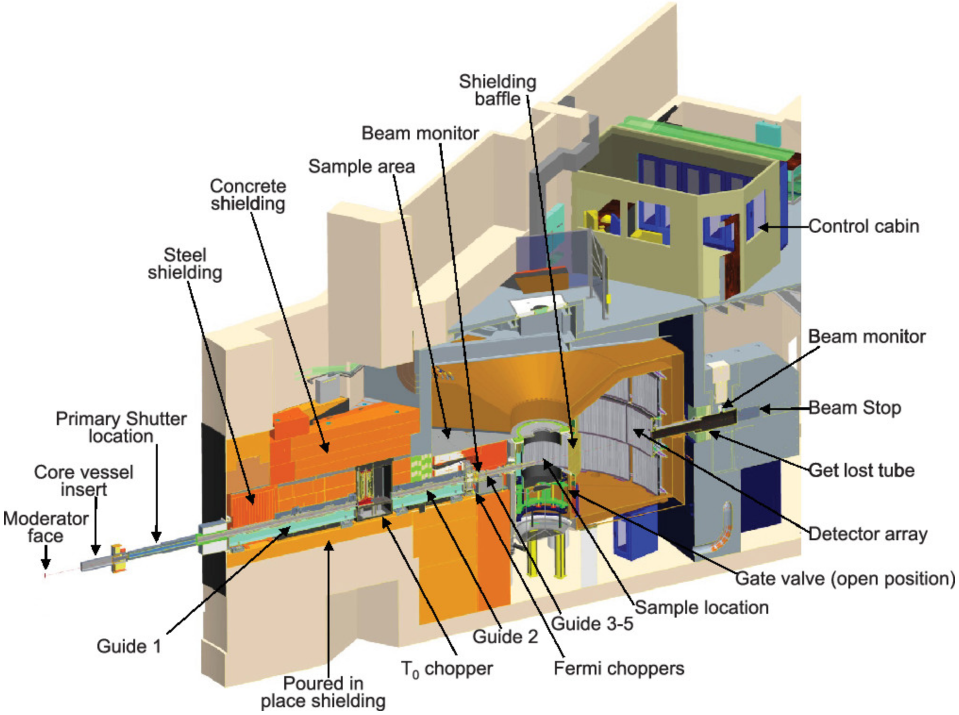

Figure 1.2: Overview rendering of ARCS with components labeled.

## Chapter 2

# PHONON ANHARMONICITY AND COMPONENTS OF THE ENTROPY IN PALLADIUM AND PLATINUM

### 2.1 Introduction

Phonon scattering has long been a subject of interest for transport properties and thermodynamics of solids. In insulators, phonon-phonon scattering is the dominant mechanism, but electron-phonon scattering is also important for metals[44–46]. The interplay between the scattering of phonons and electrons originates with the basic electronic and phonon structures of a metal, but leads to thermodynamic behavior that is challenging to understand. In previous studies of nearly-free electron metals with low electron densities of states near the Fermi level[18, 47, 48], electron-phonon interactions were weak, so phonon-phonon interactions were primarily responsible for the lifetime broadening of phonon energies. Transition metals, with their much higher densities of states near the Fermi level, generally have stronger electron-phonon interactions at low temperatures[49–53], giving these metals and alloys high critical temperatures for conventional superconductivity, for example. Electron-phonon interactions persist well above the superconducting transition temperature, however, and their effects on high temperature thermodynamics can be significant[54–56]. Phonon-phonon interactions increase with more thermal phonons, and the effects of temperature on thermodynamics can involve a number of competing mechanisms beyond the harmonic or quasiharmonic approximations of phonon behavior[57].

Effects of phonon-phonon scattering can be observed by inelastic neutron scattering experiments. These anharmonic effects cause shifts and broadenings of the measured phonon spectra[45, 46, 58, 59]. Unfortunately, it is usually not possible to decouple the effects of phonon-phonon interactions from effects of electron-phonon using measurements alone[46]. First-principles calculations of the scattering rate of each mechanism are useful for identifying the dominant scattering mechanism, and for better understanding the materials physics at the atomic level.

Palladium and platinum have commercial and technological importance for chemical engineering, electronics, dentistry, medicine, and fashion[60–62]. Their thermal physics is interesting to compare because they lie in the same column of the periodic table, with similar electronic and phonon band structures. Both have strong electron-phonon interactions owing to their high densities of electronic states at the Fermi level. However Pd was believed to have an electron-phonon coupling strength twice that of Pt[44]. A previous first-principles study[63] of electron-phonon interactions in Pd gave phonon linewidths comparable to the measured linewidth at 4.5 K, indicating that electron-phonon interactions dominate the linewidth. However, a parallel calculation for Pt is no yet available. Furthermore, the temperature dependences of electron-phonon and phonon-phonon interactions have received little study.

Here we report results from a combined experimental and theoretical study on the phonon dynamics of face-centered-cubic Pd and Pt metals. Inelastic neutron scattering experiments were performed to measure the phonon density of states of Pd and Pt at temperatures from 7 K to 1576 K. The contributions of electron-phonon and phonon-phonon scattering to the phonon linewidths were calculated by perturbation theory using methods based on density functional theory (DFT). We present the measured phonon density of states of Pd and Pt at several temperatures, then show the calculated phonon linewidths from both electron-phonon and phonon-phonon interactions and their variations with temperature. We find slightly stronger electron-phonon interactions in Pd than Pt, but slightly stronger phonon-phonon interactions in Pt. With some care to define the different contributions to the entropy[45], we report the temperature dependences of the entropic contributions from thermal expansion, phonon anharmonicity and the adiabatic electron-phonon interaction. The sum of all contributions is compared with the entropy from calorimetric measurements, with excellent results.

### 2.2 Experiment

Platinum and palladium metals of 99.9% or higher purity were formed into plates with thicknesses of 0.82 and 2.25 mm respectively, giving ratios of multiply- to singly-scattered neutrons of 9.0% and 9.6%. Neutron inelastic scattering measurements were performed with the time-of-flight Fermi chopper spectrometer, ARCS, at the Spallation Neutron Source at Oak Ridge National Laboratory. The incident neutron energy was 50.0 meV, and each measurement included a total of approximately 6.0 C proton charge on the spallation target. For temperatures of 7 and 300 K, the sample was mounted in a closed-cycle helium refrigerator. For temperatures of 326, 576, 876, 976, 1176, 1376, and 1576 K, the sample was mounted in a high temperature, electrical resistance furnace (MICAS furnace) designed for vacuum operation in the ARCS spectrometer.

Data reduction was performed with a standard software package for the ARCS instrument[64]. The raw data of individual neutron detection events were first binned to get $I(E, 2\theta)$, where $2\theta$ is the scattering angle and $E$ is the energy transfer, and normalized by the proton current on target. Bad detector pixels were identified and masked, and the data were corrected for detector efficiency using a measurement from vanadium. The $I(E, 2\theta)$ were then rebinned into intensity, $I(Q, E)$, where $\hbar Q$ is the momentum transfer to the sample. The $E$ ranged from –49.75 to 50.25 meV, with a bin width of 0.5 meV. The elastic peak was removed below 3.0 meV and replaced by a function of energy determined from the inelastic scattering just past the elastic peak [65]. The phonon DOS curves were obtained after corrections for multiphonon and multiple scattering, as described previously [65]. The averaging over all $Q$ for a given $E$ will eliminate effects of coherent interference between single- and two-phonon scattering.

## 2.3 Computational Methodology

The contribution to the phonon linewidth from phonon-phonon scattering ($2\Gamma_{\mathrm{ph-ph}}$) is[58, 59]

$$\begin{aligned} 2\Gamma_{\mathrm{ph-ph}}(\mathbf{q}, j) &= \frac{\pi\hbar}{8N} \sum_{\mathbf{q}_1,\mathbf{q}_2,j_1,j_2} \Delta(\mathbf{q}_1 + \mathbf{q}_2 - \mathbf{q}) \frac{|\Phi(-\mathbf{q}j;\, \mathbf{q}_1 j_1;\, \mathbf{q}_2 j_2)|^2}{\omega(\mathbf{q}j)\,\omega(\mathbf{q}_1 j_1)\,\omega(\mathbf{q}_2 j_2)} \\ &\times \big[(n_1 + n_2 + 1)\,\delta(\omega - \omega_1 - \omega_2) \\ &\quad +2(n_1 - n_2)\,\delta(\omega + \omega_1 - \omega_2)\big] , \end{aligned} \tag{2.1}$$

where $N$ is the number of unit cells, $\hbar$ is the Planck constant over $2\pi$, and $n$ is the Planck distribution function. Here $\Phi$ is the phonon-phonon coupling matrix element for a three-phonon process.

The contribution to the phonon linewidth from electron-phonon scattering ($2\Gamma_{\mathrm{e-ph}}$) is

$$\begin{aligned} 2\Gamma_{\mathrm{e-ph}}(\mathbf{q}, j) &= 2\pi\omega_{\mathbf{q},j} \sum_{\mathbf{k},\mathrm{i},\mathrm{f}} |g(\mathbf{k}_\mathrm{i}, \mathbf{k}_\mathrm{f}, \mathbf{q}, j)|^2 \\ &\times \delta(E_{\mathbf{k}_\mathrm{i}} - E_F)\delta(E_{\mathbf{k}_\mathrm{f}} - E_F) , \end{aligned} \tag{2.2}$$

where $\omega_{\mathbf{q},j}$ is the phonon frequency. The $g(\mathbf{k}_\mathrm{i}, \mathbf{k}_\mathrm{f}, \mathbf{q}, j)$ is the electron-phonon matrix element, where the phonon $(\mathbf{q}, j)$ scatters an electron from the initial state $\mathbf{k}_\mathrm{i}$ with energy $E_{\mathbf{k}_\mathrm{i}}$ to the final state $\mathbf{k}_\mathrm{f}$ with energy $E_{\mathbf{k}_\mathrm{f}}$.

All calculations were performed in the local density approximation with pseudopotentials and a plane-wave basis set. The phonon-phonon coupling matrix $\Phi$ of Eqn.

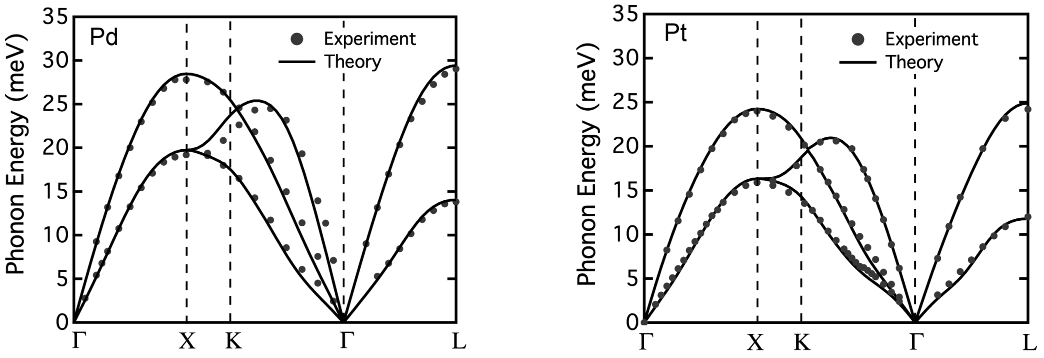

Figure 2.1: Calculated phonon dispersions of (a) Pd and (b) Pt along high symmetry directions, with points from experimental data of Refs. [1, 2].

2.1 was calculated using the small-displacement supercell method with forces from density functional theory implemented in VASP code [66–68]. Details of implementation can be found in our previous study[48]. This real-space method used 256-atom supercells, with both positive and negative displacements of 0.02 Å to cancel effects from higher-order anharmonicities. Phonon linewidths were calculated with Eqn. 2.1 using a $q$-point grid of 24 × 24 × 24 for the Brillouin zone integration.

For the electron-phonon linewidth $2\Gamma_{\text{e-ph}}$ at 0 K, the electron-phonon matrix element $g(\mathbf{k}_\text{i}, \mathbf{k}_\text{f}, \mathbf{q}, j)$ was calculated using density functional perturbation theory as implemented in the QUANTUM-ESPRESSO package [69]. The first-order Hermite Gaussian smearing technique with a width of 0.022 Ryd was used to account for the presence of a Fermi surface. A $k$-space sampling grid of 24 × 24 × 24 was used for the Brillouin zone integration of Eqn. 2.2. Since both $2\Gamma_{\text{ph-ph}}$ and $2\Gamma_{\text{e-ph}}$ are calculated with respect to the phonon energy itself, the inconsistency of using two different ab-initio computing engines is minimized by choosing the PAW-LDA pseudopotentials that yield comparable phonon and electron bandstructures.

## 2.4 Results and Discussion

### Phonon dispersions and DOS, Kohn anomalies

Figures 2.4 and 2.4 show the calculated phonon dispersions along high symmetry directions at 0 K, along with previous inelastic neutron scattering measurements at 296 K for Pd[1] and 90 K for Pt[2]. The agreement is excellent. The dispersion curves of Pd and Pt have similar features, but the energies are shifted upwards for Pd compared to Pt. The shifts are about 50 to 65% of what is expected from the mass difference alone, indicative of stronger interatomic forces in Pt. This is also

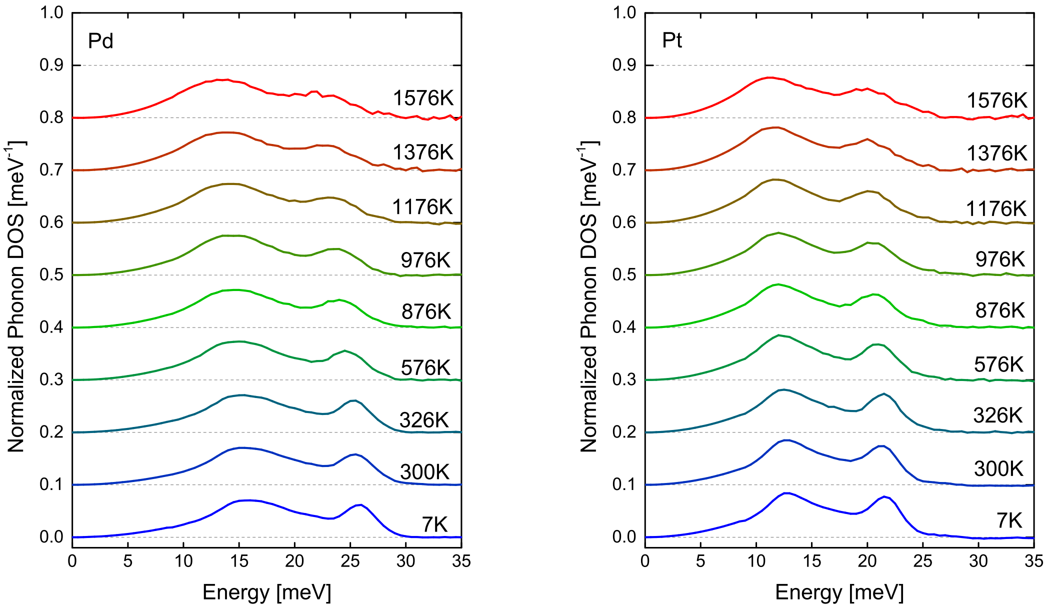

Figure 2.2: Experimental phonon DOS curves of Pd (a) and Pt (b) normalized to unity. Curves are offset for clarity.

seen in Figs. 2.4 and 2.4 that show the phonon densities of states (DOS) of Pd and Pt measured in this work at temperatures from 7 K to 1576 K. With increasing temperature, features of the DOS shift downwards in energy (soften) and the features broaden in energy.

Kohn anomalies were previously reported in the phonon dispersions of both Pd and Pt along the [011] direction[1, 2, 70]. They are also reproduced by our calculations at $\mathbf{q}_{\text{cal}} \simeq \frac{2\pi}{a}[0.31, 0.31, 0]$, slightly lower than the experimental result of $\mathbf{q}_{\text{exp}} \simeq \frac{2\pi}{a}[0.35, 0.35, 0]$. Effects of Kohn anomalies are also seen around 8 meV in our experimental phonon DOS for both Pd and Pt at 7 K (Fig. 2.2). These features are diminished with temperature, and are no longer visible at temperatures around 900 K or so.

### Measured phonon shifts and broadenings

Temperature causes the peaks in the experimental phonon DOS of both Pd and Pt to broaden, and shift to lower energy (Fig. 2.2). The thermal softening of phonons in Pd is more rapid than in Pt. This may reflect the stiffer interatomic forces in Pt. The thermal shift was approximated by rescaling all energies with a constant multiplier, $\eta$,

$$E' \longmapsto \eta E' \ . \tag{2.3}$$

The thermal broadening, which was more prominent than the thermal shift, was modeled with the spectral weight function of a damped harmonic oscillator[71], centered about energy $E'$ with the quality factor $Q$. The broadening function $B\left(Q;E,E'\right)$ is

$$B\left(Q;E,E'\right)=\frac{1}{\pi QE'}\frac{1}{\left(\frac{E'}{E}-\frac{E}{E'}\right)^2+\frac{1}{Q^2}}. \tag{2.4}$$

Using Eqns. 2.3 and 2.4, the measured phonon DOS at temperature $T$, $g_T(E)$, was fit to an convolution-like integral transform of $g_{7\mathrm{K}(E)}$, the rescaled phonon DOS measured at the lowest temperature of 7 K

$$\begin{aligned} g_T(E) &= \int B(Q;E,E')g_{7\mathrm{K}}\left(\eta E'\right)dE' \\ &\triangleq B(Q;E,E')\odot g_{7\mathrm{K}}\left(\eta E'\right)\ . \end{aligned} \tag{2.5}$$

In principle, each phonon mode has a unique thermal shift and broadening, but it has proved useful and more practical to work with averaged values of $\eta$ and $Q$ for the full phonon DOS, as was previously reported for Al[65]. This approach is demonstrated in Fig. 2.3a, and it is evident that the calculated broadening is too large for the low-energy peak of the DOS, and the broadening is too small for the high-energy peak. The high quality of our experimental phonon DOS for Pd and Pt made it practical to fit separately the two main features of the DOS, which originate primarily from transverse and longitudinal modes, by rewriting Eqn. 2.5 as

$$\begin{aligned} g_T(E) &= B(Q^{\mathrm{TA}};E,E')\odot g_{7\,\mathrm{K}}^{\mathrm{TA}}\left(\eta^{\mathrm{TA}}E'\right) \\ &+ B(Q^{\mathrm{LA}};E,E')\odot g_{7\,\mathrm{K}}^{\mathrm{LA}}\left(\eta^{\mathrm{LA}}E'\right). \end{aligned} \tag{2.6}$$

The $g_{7\,\mathrm{K}}^{\mathrm{TA}}$ and $g_{7\,\mathrm{K}}^{\mathrm{LA}}$ were obtained by fitting the two features of the DOS curve at 7 K to Lorentzian functions. For each temperature, the four factors $\{Q^{\mathrm{TA}}$, $\eta^{\mathrm{TA}}$; $Q^{\mathrm{LA}}$, $\eta^{\mathrm{LA}}\}$ were determined through a least-squares algorithm implemented with gradient descent. A resulting fit is shown in Fig. 2.3b, giving better agreement than when the transverse and longitudinal features are not differentiated as in Fig. 2.3a.

Figures 2.4a and 2.4b show the temperature dependence of the shift and broadening parameters $\{Q^{\mathrm{TA}}$, $\eta^{\mathrm{TA}}$; $Q^{\mathrm{LA}}$, $\eta^{\mathrm{LA}}\}$. The transverse modes soften faster with temperature than the longitudinal modes in both Pt and Pd, but all are linear with temperature, $\eta \propto T$. An approximately linear temperature dependence is also seen for the broadening of the longitudinal modes as shown in Fig. 2.4 b for $1/Q$ vs. $T$. However, the thermal broadening of the transverse modes is distinctly nonlinear, at least for temperatures below 1000 K.

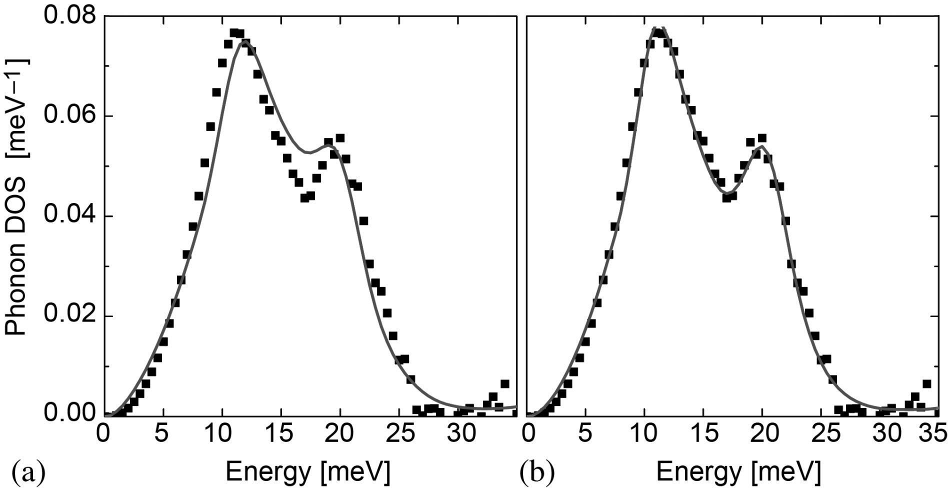

Figure 2.3: Fittings of Pt phonon DOS at 1576 K using broadened, shifted DOS curve from 7 K. (a) Fit using Eq. 2.5. (b) Fit using Eq. 2.6 with separate transverse and longitudinal components.

### Electron-phonon and phonon-phonon interactions, phonon linewidths

Figures 2.5 and 2.6 present $2\Gamma_{\mathrm{e-ph}}$ and $2\Gamma_{\mathrm{ph-ph}}$ for phonons along high symmetry directions for both Pd and Pt at 0 K. The phonon linewidths of Pd are in the range of 0 to 0.3 meV, similar to those of a previous study[63], and comparable to experimental measurements[70]. Although a substantial difference in electron-phonon scattering strength of Pd and Pt was suggested previously[44], we found that $2\Gamma_{e-p}$ is comparable for Pd and Pt.

The overall electron-phonon coupling strength can be described by a dimensionless parameter

$$\lambda = \sum_{\mathbf{q},j} \pi N_{\mathrm{F}} \omega_{\mathbf{q},j}^2 \Gamma_{\mathbf{q},j} \ , \tag{2.7}$$

where $N_{\mathrm{F}}$ is the electron density of states at the Fermi energy, and $\omega_{\mathbf{q},j}$ and $\Gamma_{\mathbf{q},j}$ are the phonon angular frequency and linewidth. The Fermi surface was broadened in energy with Gaussian functions as implemented in the QUANTUM-ESPRESSO package [69], so electron-phonon coupling strengths $\lambda$ were calculated as a function of broadening, $\sigma$. The converged value of $\lambda$ was $\sigma = 0.25$ Ryd, which is the minimal possible broadening that still achieves convergence[72]. Our calculated values of $\lambda$ are 0.41 and 0.59 for Pd and Pt respectively, which are close to the empirical values[73] of 0.47 and 0.66.

Figure 2.6 shows $2\Gamma_{\mathrm{ph-ph}}$ at 0 K, which is similar for both Pd and Pt. At 0 K the TA modes are an order-of-magnitude narrower than the higher energy LA modes.

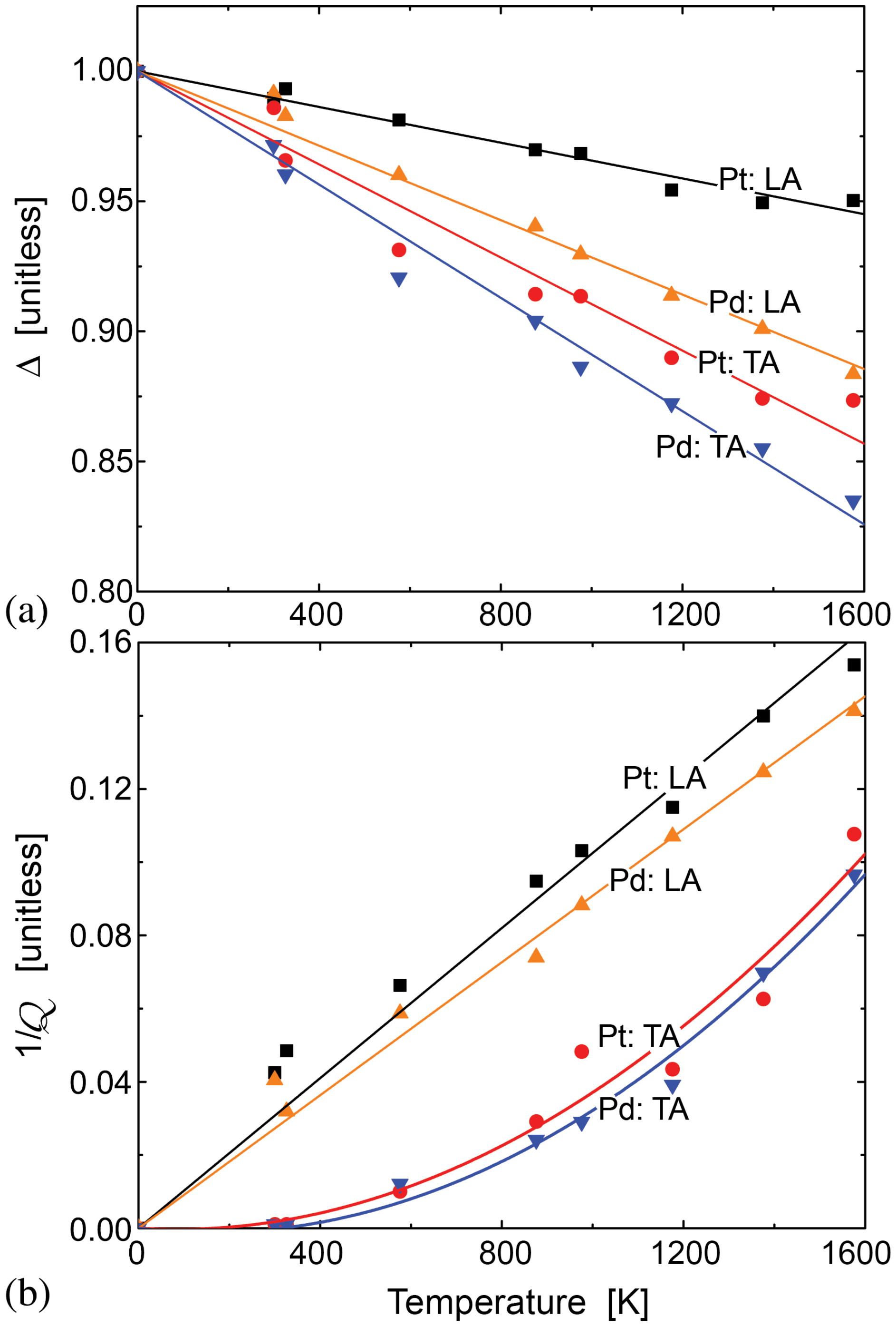

Figure 2.4: Temperature dependences from data of Fig. 2.2 for (a) phonon shift $\eta$ vs. $T$, and (b) broadening $1/Q$ vs. $T$ for Pd and Pt.

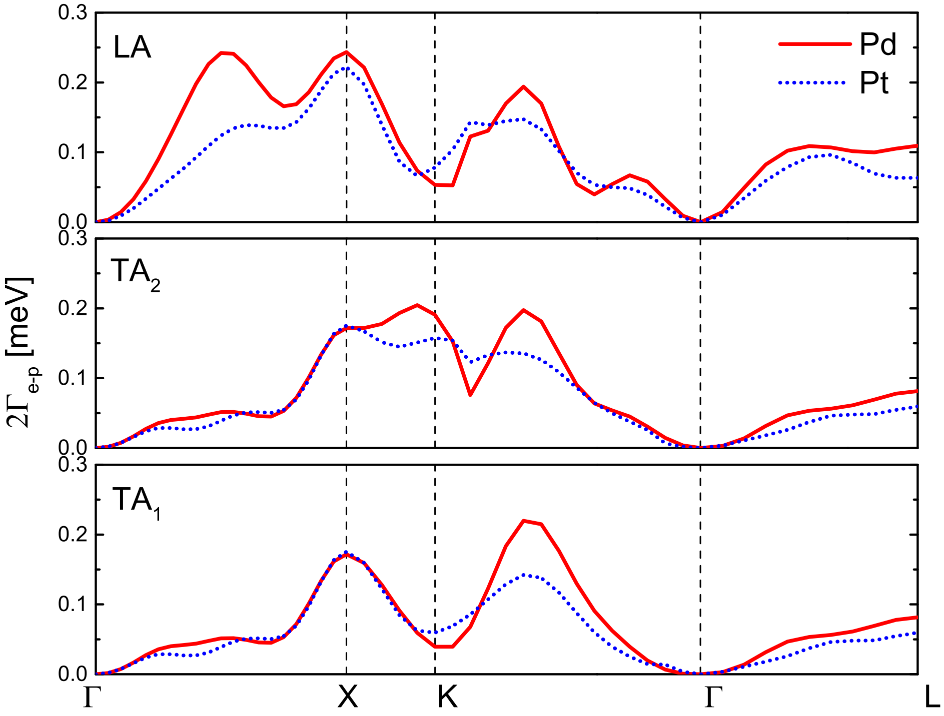

Figure 2.5: Electron-phonon contributions to phonon linewidth of Pd (solid line) and Pt (dotted line) at 0 K.

Comparing Fig. 2.5 with Fig. 2.6, the $2\Gamma_{\text{e-ph}}$ and $2\Gamma_{\text{ph-ph}}$ are comparable for LA modes, but the $2\Gamma_{\text{e-ph}}$ are much larger than the $2\Gamma_{\text{ph-ph}}$ for TA modes. At 0 K, LA phonons are effectively scattered by both electrons and other phonons, whereas TA phonons are scattered mostly by electrons. Figure 2.7 shows the phonon linewidths at 900 K. Here the $2\Gamma_{\text{ph-ph}}$ at 900 K are nearly 10 times larger than $2\Gamma_{\text{e-ph}}$ at 0 K, showing the dominance of phonon-phonon interactions at high temperatures.

The trends of Fig. 2.4b are supported by Figs. 2.6 and 2.7. At low temperatures only down-conversion processes are possible, and there are more down-scattering channels for LA than TA modes. The broadening of transverse modes by up-scattering involves the annihilation of phonons, and does not occur unless enough thermal phonons are available. Figure 2.4 shows that the thermal broadenings of phonons in Pd and Pt are very similar, however, consistent with experimental results from Sect. 2.4. At higher temperatures, three-phonon processes dominate the broadening. These are quite similar for Pd and Pt, consistent with their rather similar phonon dispersions shown in Fig. 2.1. Approximately, at 900 K the broadening of the longitudinal feature of the Pd phonon DOS has a breadth of $1/Q = 0.09$ from Fig. 2.4b, and an energy of 24 meV from Fig. 2.2, giving a broadening of 2.2 meV. This

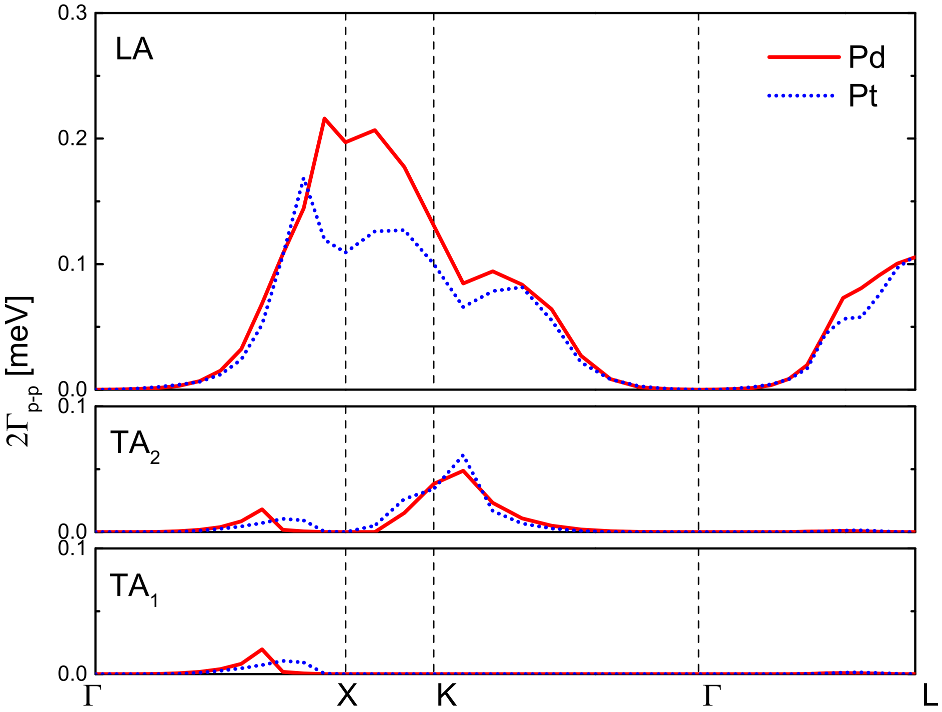

Figure 2.6: Phonon-phonon contributions to phonon linewidth of Pd (solid line) and Pt (dotted line) at 0 K.

is in agreement with the broadenings calculated from phonon-phonon interactions shown in Fig. 2.7.

### Entropy

For Pd and Pt, the contributions to the entropy[74] are from phonons ($S_{\text{ph}}$), electrons ($S_{\text{el}}$), their interactions ($S_{\text{ep}}$), and the lattice configurations ($S_{\text{cf}}$)

$$S_{\text{tot}} = S_{\text{ph}} + S_{\text{el}} + S_{\text{ep}} + S_{\text{cf}} \ . \tag{2.8}$$

The entropy from the nonadiabatic electron-phonon interaction, $S^{\text{na}}_{\text{ep}}$, is from the mixing of the electron ground states from the nuclear motion. It dominates at low temperatures[45], but the adiabatic electron-phonon entropy $S^{\text{ad}}_{\text{ep}}$ is larger at higher temperatures. This $S^{\text{ad}}_{\text{ep}}$ accounts for the thermal shifts of electron states caused by average nuclear motions[45]. The total entropy is now

$$S_{\text{tot}} = S_{\text{ph}} + S_{\text{el}} + S^{\text{na}}_{\text{ep}} + S^{\text{ad}}_{\text{ep}} + S_{\text{cf}} \ . \tag{2.9}$$

We obtained the total phonon entropy from the experimental phonon DOS shown

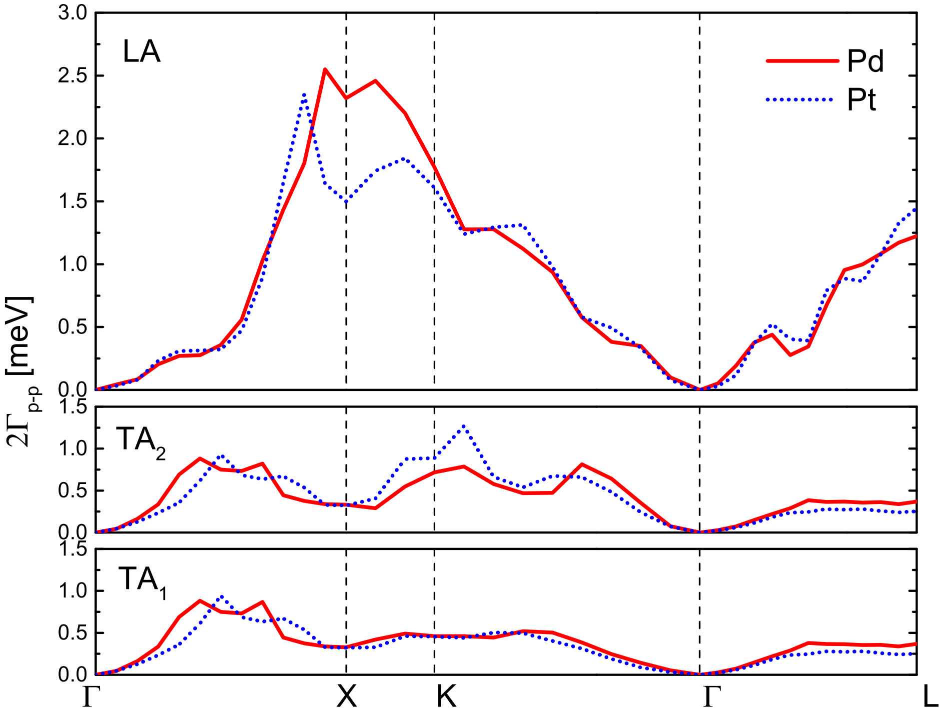

Figure 2.7: Phonon-phonon contributions to phonon linewidth of Pd (solid line) and Pt (dotted line) at 900 K.

in Fig. 2.2 using the expression

$$\begin{aligned} S_{\text{ph}}(T) &= 3k_{\text{B}} \int \mathrm{d}E\; g_T(E) \\ &\times \left[ \left(n_T + 1\right) \ln \left(n_T + 1\right) - n_T \ln \left(n_T\right) \right], \end{aligned} \tag{2.10}$$

where $g_T(E)$ is the phonon DOS and $n_T(E)$ is the Planck distribution, both at the temperature of interest, $T$. When $g_T(E)$ is measured at the temperature of interest, Eq. 2.10 is rigorously correct for the effect of harmonic and quasiharmonic vibrations on the entropy, and for the effects of electron-phonon interactions on these vibrations. It also provides a good accounting for the anharmonic shifts of vibrational frequencies[46, 57, 74].

For identifying the different types of non-harmonic behavior, an ideal harmonic crystal is a convenient reference. The harmonic entropy $S_{\text{ph,H}}$ is obtained by assuming the low-temperature phonon DOS is unaltered by temperature, so to obtain $S_{\text{ph,H}}$ we used the DOS measured at 7 K in Eq. 2.10, with the Planck occupancy $n_T(E)$ for the (higher) temperatures of interest.

Thermal expansion gives the quasiharmonic contribution to the phonon entropy,

$\Delta S_{\mathrm{ph,QH}}$

$$\Delta S_{\mathrm{ph,QH}}(T) = 9\int_0^T B v \alpha^2 \mathrm{d}T', \tag{2.11}$$

where $B$ is the isothermal bulk modulus, obtained from the literature[75–79], $v$ is the specific volume[80, 81] and $\alpha$ is the linear coefficient of thermal expansion[80, 81], and all must be taken at the temperature $T'$. [45] The anharmonic contribution to the phonon entropy ($\Delta S_{\mathrm{ph,Anh}}$) and the nonharmonic contribution ($\Delta S_{\mathrm{ph,NH}}$) are

$$\begin{aligned} \Delta S_{\mathrm{ph,Anh}} &= S_{\mathrm{ph}} - S_{\mathrm{ph,H}} - \Delta S_{\mathrm{ph,QH}} && (2.12)\\ \Delta S_{\mathrm{ph,NH}} &= S_{\mathrm{ph}} - S_{\mathrm{ph,H}} && (2.13)\\ \Delta S_{\mathrm{ph,NH}} &= \Delta S_{\mathrm{ph,QH}} + \Delta S_{\mathrm{ph,Anh}}. && (2.14) \end{aligned}$$

As fermions, the entropy from the electrons is

$$\begin{aligned} S_{\mathrm{el}}(T) &= -k_{\mathrm{B}} \int \mathrm{d}E\ N_T(E) \\ &\times \left[ \left(1 - f_T\right) \ln\left(1 - f_T\right) + f_T \ln\left(f_T\right) \right], \end{aligned} \tag{2.15}$$

where $N_T(E)$ is the electronic DOS and $f_T(E)$ is the Fermi distribution function, both at the temperature of interest, $T$. To separate the effect of thermal expansion, we define the "ground state" electronic entropy, $S_{\mathrm{el,G}}(T)$ by using the electronic DOS at $T_0 = 0\,\mathrm{K}$, $N_{\mathrm{G}}(E)$, but using the Fermi distribution at temperature $T$ in Eq. 2.15. Taking dilation into account, the electronic DOS, $N_D(E)$, was calculated for volumes consistent with thermal expansion. The dilation effect is separated from the ground state electronic entropy as

$$\Delta S_{\mathrm{el,D}} = S_{\mathrm{el}}\left(N_{\mathrm{D}}\right) - S_{\mathrm{el}}\left(N_{\mathrm{G}}\right). \tag{2.16}$$

Once $\Delta S_{\mathrm{el,D}}$ is calculated at a low-temperature volume and a high-temperature volume, an interpolation can be performed for intermediate temperatures[82].

The adiabatic electron-phonon interaction (EPI) causes a thermal broadening of electron levels. Following Thiessen[83], we used an electronic broadening function of Lorentzian form with full-width-at-half-maximum $2\Gamma = 2\pi\lambda k_B T$, and modified the electronic DOS by the convolution

$$N_{\mathrm{ep}}(E) = N_G(E) * \mathcal{L}\left(2\Gamma = 2\pi\lambda k_B T\right). \tag{2.17}$$

The chemical potential changes with temperature to conserve electrons. The adiabatic EPI contribution to the change in the electronic entropy is

$$\Delta S^{\mathrm{ad}}_{\mathrm{el,ep}} = S_{\mathrm{el}}\left(N_{\mathrm{ep}}\right) - S_{\mathrm{el}}\left(N_{\mathrm{G}}\right). \tag{2.18}$$

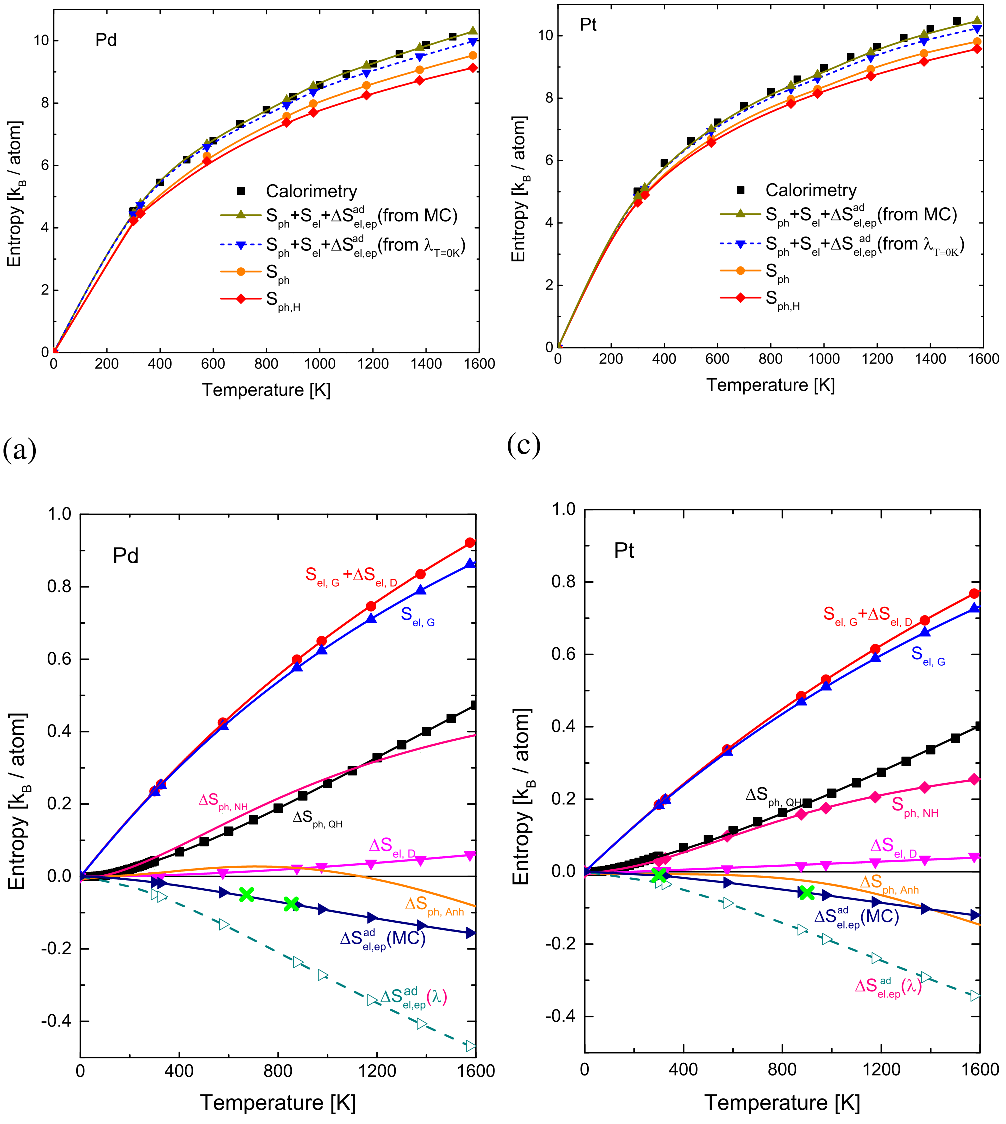

(a) (c)

(b) (d)

Figure 2.8: The origins of entropy of (a,b) Pd and (c,d) Pt. (a,c) “Calorimetry” points are from Arblaster[3, 4], $S_{\text{ph}}$ are from data of Fig. 2.2 and Eq. 2.10, $S_{\text{ph,H}}$ was calculated with Eq. 2.10 and the measured phonon DOS at 7 K, and $S_{\text{el}}$ is the sum of $S_{\text{el,G}}$ and $\Delta S_{\text{el,D}}$. (b,d) The different minor contributions make up less than 10% of the total entropy. They are from the lattice dilation influence on phonons and electrons ($\Delta S_{\text{ph,QH}}$, $\Delta S_{\text{el,D}}$), the anharmonicity ($\Delta S_{\text{ph,Anh}}$) and the adiabatic EPI induced thermal broadening in electron DOS ($\Delta S^{\text{ad}}_{\text{el,ep}}$). The $\Delta S^{\text{ad}}_{\text{el,ep}}$ was first calculated using the electron-phonon coupling parameter, $\lambda$ at $T = 0$ K ($\Delta S^{\text{ad}}_{\text{el,ep}}(\lambda)$), and then rescaled by Monte Carlo calculations to give our preferred $\Delta S^{\text{ad}}_{\text{el,ep}}$(MC).

As temperature increases, the thermal excitation of $d$-band electrons shifts the chemical potential to higher energies and away from the peak in the electronic DOS, reducing the contribution of the $d$-band electrons to the electron-phonon coupling strength. Hence $\lambda$ should decrease at higher temperatures. To correct for this, we calculated electronic bandstructures for an ensemble of supercells with atom displacements appropriate for a few high temperatures, and used their electronic structures to obtain accurate values of $\Delta S_{\mathrm{el,ep}}^{\mathrm{ad}}$. These points were used to rescale the adiabatic EPI obtained from Eq. 2.18 as shown in Fig. 2.8.

More specifically, we prepared ensembles of ten supercells with atoms displaced with a Monte Carlo algorithm[84] for phonons calculated with experimental force constants[2, 85, 86]. For each configuration of displaced atoms, the electronic DOS ($N_{\mathrm{MC}}$) was calculated, and an $\Delta S_{\mathrm{el,ep}}^{\mathrm{ad}}$ was calculated as

$$\Delta S_{\mathrm{el,ep}}^{\mathrm{ad}} = S_{\mathrm{el}}\left(N_{\mathrm{MC}}\right) - S_{\mathrm{el,G}} - \Delta S_{\mathrm{el,D}}. \tag{2.19}$$

These ten values of the adiabatic EPI were averaged, and used to rescale the curves of $\Delta S_{\mathrm{el,ep}}^{\mathrm{ad}}(\lambda)$ from Eq. 2.18 at the temperatures of the calculations, (673, 853) K for Pd and (300, 900) K for Pt. This gave our preferred curves of $\Delta S_{\mathrm{el,ep}}^{\mathrm{ad}}$(MC) in Fig. 2.8.

The entropy of Pd and Pt is mainly from phonons, which can be accounted for by the harmonic approximation. Other contributions provide about 10% of the total entropy, but this 1 $k_{\mathrm{B}}$/atom at high temperatures is important thermodynamically. The contribution from the anharmonic phonons, $\Delta S_{\mathrm{ph,Anh}}$ is negative at all temperatures in Pd, but in Pt it changes with temperature from positive to negative. This trend is consistent with the report from Wallace [82], but our crossover temperature is somewhat higher (at 1100 K versus 800 K). Overall, the relationship

$$S_{\mathrm{ph,H}} \gg \Delta S_{\mathrm{ph,QH}} > \Delta S_{\mathrm{ph,Anh}} \tag{2.20}$$

holds for both Pd and Pt.

For Pd and Pt, the dilation contribution to the electron entropy, $S_{\mathrm{el,D}}$, is always positive, while that from the adiabatic EPI is negative. The broadening of the electron DOS from the adiabatic EPI has a more significant influence on the electronic entropy than the dilation from thermal expansion. This differs from Al[65] or V[87], since the Fermi level in Pd or Pt is at a peak in the density of $d$-electron states. With lattice dilation, the chemical potential remains pinned at the top of the sharp peak. Alternatively, the EPI-induced thermal broadening moves the chemical potential to

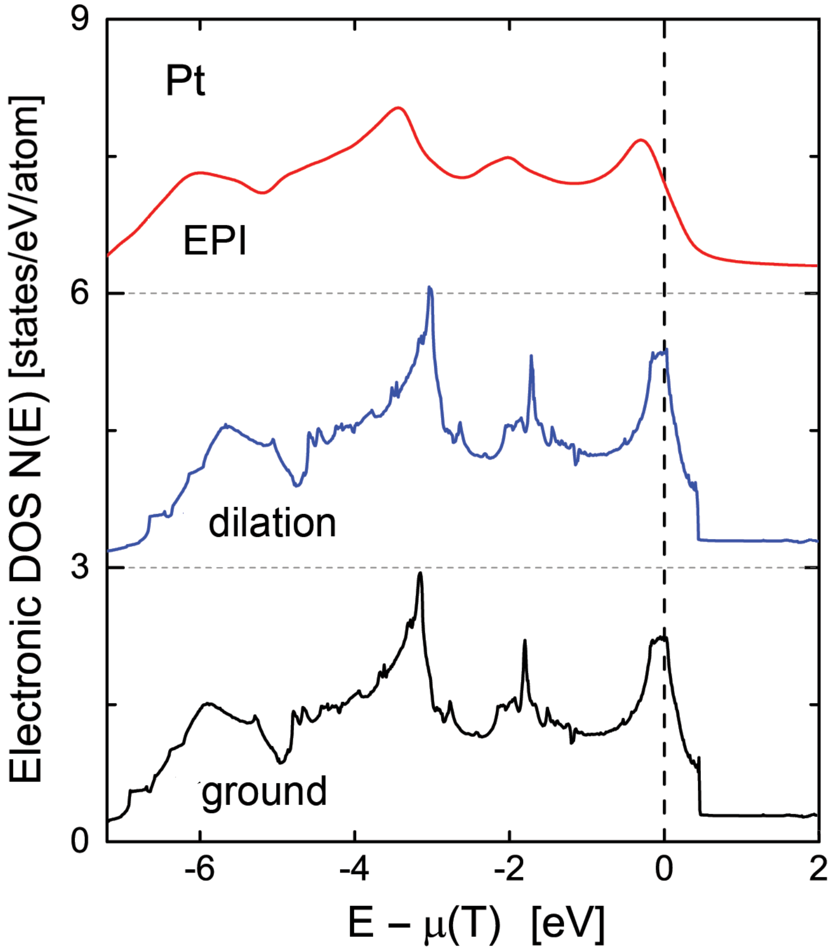

Figure 2.9: The electronic DOS of Pt at the ground state, with dilation, and with thermal broadening by the adiabatic electron-phonon interaction. Curves are offset for clarity.

a higher energy and away from the peak, giving a stronger temperature dependence to $\Delta S^{\mathrm{ad}}_{\mathrm{el,ep}}$. Examples of these effects are shown in Figure 2.9 for Pt.

We considered, but neglected, the configurational entropy of thermal vacancies, since it is quite small $S_{\mathrm{vac}} < 1.8 \times 10^{-3}$ $k_{\mathrm{B}}$/atom (assuming a vacancy formation energy[88] $E_{\mathrm{vac}} > 1.15\,\mathrm{eV}$). We also neglected $\Delta S^{\mathrm{na}}_{\mathrm{ep}}$, expecting it to be small, especially at high temperatures. Finally, entropic contributions from paramagnons[89] are possible in Pd, but the final discrepancies of total entropies are similarly small for both Pt and Pd, so such a contribution is likely to be small for Pd.

Figures 2.8 a,c compare the total entropy from our measured phonon DOS and DFT calculations ($S_{\mathrm{ph}} + S_{\mathrm{el}} + \Delta S^{\mathrm{ad}}_{\mathrm{el,ep}}$) with calorimetry results reported by Arblaster[3, 4]. The agreement is excellent.

## 2.5 Conclusions

An experimental and computational study was performed on the lattice dynamics and statistical mechanics of palladium and platinum from 7 K to 1576 K. Phonon densities of states, measured by inelastic neutron scattering experiments, softened and broadened with temperature. Calculations showed that electron-phonon scattering is the dominant mechanism for the phonon lifetime broadening at low temperatures, whereas phonon-phonon scattering dominates at high temperatures. The peaks in the phonon DOS from longitudinal and transverse phonons showed distinctly different thermal broadenings. The requirement for a population of thermal phonons for upscattering suppressed the characteristic lifetime broadening of transverse phonons until the temperature exceeded 500 or 600 K, whereas the characteristic broadening of longitudinal phonons was approximately linear with temperature.

The individual components to the total entropy of palladium and platinum were assessed. The dilation from thermal expansion makes positive contributions to the entropy from both phonons and electrons. For phonons, the contribution from thermal expansion (quasiharmonicity) is larger than that from the anharmonicity. In Pt, the anharmonic contribution to phonon entropy is negative, whereas in Pd it is positive at low temperature and becomes negative above approximately 1100 K. For electrons, the effect of the adiabatic electron-phonon interaction (EPI) is negative for both Pd and Pt. For electrons, the adiabatic EPI has a larger effect on the entropy than the effect of thermal expansion. At $T = 0\,\mathrm{K}$, the Fermi level is at a sharp peak of DOS from the $d$-band, making the electronic entropy more sensitive to thermal effects on the adiabatic EPI. With measured phonon densities of states, and with calculations of the important electronic contributions to the entropy, statistical mechanics gave total entropies of Pd and Pt metal in excellent agreement with entropies from classical thermodynamics based on heat capacity measurements.

### *Chapter 3*

# THE TEMPERATURE DEPENDENCE OF PHONONS IN IRON GERMANIDE

## 3.1 Introduction

Germanium-based alloys are of interest for applications in spin-based electronic devices[90]. Beginning in 1961[91], $FeGe_2$ has been the focus of numerous experimental and theoretical studies to describe its magnetic properties [5–11]. This material exhibits two zero-field magnetic phase transitions at temperatures of $T_N = 289$ K and $T_c = 263$ K. The first transition corresponds to a second-order Néel transition from a paramagnetic high-temperature phase to an incommensurate spin-density-wave state (intermediate-temperature phase, ITP). The second transition corresponds to a first-order transition to the anti-ferromagnetic low-temperature phase[10]. The phonon properties of $FeGe_2$ have received less attention, but provide an excellent opportunity to determine how well the thermodynamic functions of anharmonic materials can be understood.

$FeGe_2$ has the same body-centered tetragonal C16 crystal structure[92] (see Fig. 3.1) as $\theta$-phase $Al_2Cu$ in which an anomalously large vibrational entropy was reported by Wolverton and Ozoliņš[93]. The calculated electronic energy of the equilibrium $\theta$-phase (C16 structure) was found to be 15 meV/atom larger than that of the $\theta'_c$-phase (C1 fluorite structure). The authors concluded that the $\theta$-phase is stabilized at finite temperature by vibrational entropy, and this entropic stabilization of the $\theta$-phase may originate with features of its low-symmetry structure.

$FeGe_2$ is also a likely candidate for large phonon anharmonicity related to phonon-phonon interactions because of the absence of inversion symmetry at Ge atoms[94]. The phonon energies can have a temperature dependence from a number of competing mechanisms beyond the harmonic or quasiharmonic approximations, as observed in other transition-metal systems[12].

Here we report results from a combined experimental and computational study on the phonon dynamics of $FeGe_2$. Phonon dispersions and phonon density of states (DOS) were measured by inelastic neutron scattering (INS), and Fe partial DOS were measured by nuclear resonant inelastic X-ray scattering (NRIXS). First-principles calculations based on density functional theory (DFT) with the quasiharmonic ap-

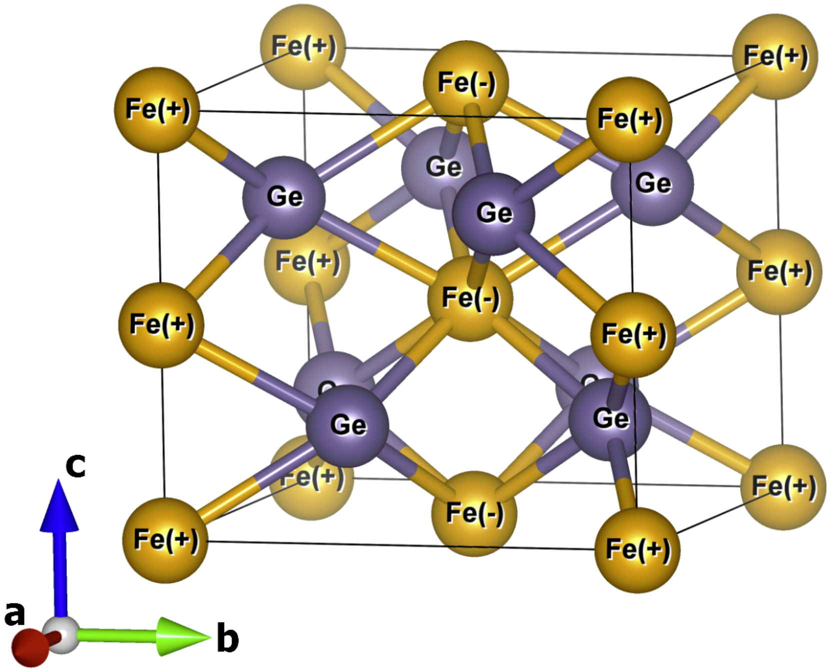

Figure 3.1: Crystal structure of $FeGe_2$. It is a tetragonal C16 structure with alternating layers of Fe and Ge atoms. The positions of atoms are[5]: Fe (orange) at $(0,0,0)$, $(0,0,\frac{1}{2})$ and Ge (blue) at $(x,\frac{1}{2}+x,\frac{1}{4})$, $(\bar{x},\frac{1}{2}-x,\frac{1}{4})$, $(\frac{1}{2}+x,\bar{x},\frac{1}{4})$, $(\frac{1}{2}-x,x,\frac{1}{4})$, where $x = 0.1547$ is the atomic parameter for Ge positions. Bonds are only drawn between first nearest-neighborhoods (1NN). Plus and minus signs identify the collinear spin structure of the anti-ferromagnetic low-temperature phase[5–11].

proximation (QHA) were performed between 325-1050 K, and small-displacement method was used to calculate the phonons. Separately, a fully anharmonic calculation was performed at 635 K using the stochastically initialized temperature-dependent effective potential method (s-TDEP) [40]. The DFT calculations with QHA, which only consider the volume expansion without thermal effects, are in close agreement with the phonon DOS data in the low-energy region, but discrepancies between the QHA calculations and the experimental data are found in the high-energy region, indicating a strong anharmonicity of the high-energy phonon modes. The difference between the calculated and measured isobaric Grüneisen parameter shows that the QHA alone is insufficient to model the softening of individual phonons with temperature, even though the average behavior is semi-quantitatively correct.

## 3.2 Experiment

The sample of $FeGe_2$ was a semi-cylindrical crystal 15 mm in radius and 40 mm in length with a mass of 110 g. This crystal was loaned from Oak Ridge National Laboratory and previously measured by Adams, et al[11]. Polycrystalline samples of $FeGe_2$ were prepared from a mixture of the elements of 99.99% purity by arc-melting in a Ti-gettered argon atmosphere, followed by annealing under vacuum. Samples at isotopically-enriched $^{57}FeGe_2$ were prepared similarly.

Inelastic neutron scattering (INS) measurements were performed on both single crystal and powder samples with the time-of-flight Wide Angular-Range Chopper Spectrometer, ARCS, at the Spallation Neutron Source at Oak Ridge National Laboratory. An incident energy of 70 meV was used for all measurements. The powder sample was placed in a Nb foil sachet and mounted in a low-background electrical resistance vacuum furnace for measurements at temperatures of 325, 476, 650, 850 and 1050 K. The lattice constants were obtained from elastic scattering, acquired simultaneously, and integrated over a range of ±1 meV. The single crystal was mounted inside the same furnace with the [HK0] crystallographic plane horizontal, and measurements were performed at 300, 500, and 635 K.

Data reduction was performed with DGS reduction in Mantid [95]. The single crystal and powder data were normalized by the proton current on target. Bad detector pixels were identified and masked, and the data were corrected for detector efficiency using a measurement from vanadium. The phonon DOS curves from powder data were obtained after corrections for multiphonon and multiple scattering using the *getdos* package [96]. The single crystal neutron data from 240 rotations in increments of 0.5° about the vertical axis were reduced to create the 4-dimensional $S(\mathbf{Q}, E)$. Single crystal data analysis was performed with DAVE [97].

Nuclear resonant inelastic X-ray scattering (NRIXS) measurements were performed on $^{57}FeGe_2$ at beamline 16ID-D at the Advanced Photon Source at Argonne National Laboratory [98, 99]. The powder sample was secured in Kapton tape and placed at a grazing angle to the incident X-ray beam. Incoherently reradiated photons were measured by two avalanche photodiode detectors (APD) positioned normal to the incident beam. The energy was scanned from –160 to +160 meV around the nuclear resonance energy of $^{57}Fe$ 14.413 keV. Several scans were combined for final analysis. The energy resolution of all NRIXS measurements was measured to be 2.1858 meV (FWHM) at the elastic line. NRIXS data was reduced using the PHOENIX code[100].

## 3.3 Computation

The *ab initio* DFT calculations were performed with the VASP package[66–68] on a plane-wave basis set, using the projector augmented wave (PAW) pseudopotentials[101] with the Perdew-Burke-Ernzerhof (PBE) exchange correlation functional[102]. The energy cutoff was 600 eV for all calculations. The phonon DOS with QHA was calculated on a supercell of 216 atoms with a 2×2×2 $k$-point mesh using the small-displacement method as implemented in the PHONOPY code[103]. Except for the ground states discussed in Sect. 3.5, all the phonon-related calculations are non-spin-polarized.

The QHA for phonon behavior was obtained from the thermal expansion at elevated temperatures, using lattice parameters obtained from the neutron scattering experiments. The neutron-weighting arising from the efficiency for phonon scattering of neutrons by different modes was taken into consideration when comparing the computations with the experimental results. For $FeGe_2$, the neutron-weighted DOS[104] is

$$\begin{aligned} g^{\mathrm{NW}}(\epsilon) &= A^{-1}\sum_i g_i(\epsilon)\frac{\sigma_{sc,i}}{m_i}x_i \\ &\simeq 0.47 g_{\mathrm{Fe}}(\epsilon) + 0.53 g_{\mathrm{Ge}}(\epsilon)\ , \end{aligned} \tag{3.1}$$

where $g_i(\epsilon)$ is the phonon partial DOS of atom $i$ (i.e. Fe pDOS or Ge pDOS), $\sigma_{sc,i}$ is the total scattering cross section, $m_i$ is the atomic mass, $x_i$ is the mole fraction, and A is a normalization factor.

Beyond the QHA, the finite temperature phonons at 635 K were calculated with the s-TDEP method[41, 105, 106]. In this procedure, the Born-Oppenheimer surface of $FeGe_2$ at 635 K was sampled by a Monte Carlo sampling of atomic positions and momentum near equilibrium positions. By using DFT with various configurations of displaced atoms by a stochastic sampling of a canonical ensemble, with Cartesian displacements ($u_i^\alpha$) normally distributed around the mean thermal displacement, the forces on atoms were fitted to a model Hamiltonian

$$\begin{aligned} \hat{H} = \quad U_0 &+ \sum_i \frac{\mathbf{p}_i^2}{2m_i} + \frac{1}{2!}\sum_{ij}\sum_{\alpha\beta}\Phi_{ij}^{\alpha\beta}u_i^\alpha u_j^\beta \\ &+ \frac{1}{3!}\sum_{ijk}\sum_{\alpha\beta\gamma}\Phi_{ijk}^{\alpha\beta\gamma}u_i^\alpha u_j^\beta u_k^\gamma \ldots, \end{aligned} \tag{3.2}$$

Here, $U_0$ is a fit parameter for the baseline of the potential energy surface. The quadratic force constants $\Phi_{ij}$ from the thermally-displaced atoms capture not only harmonic properties but also temperature-dependent nonharmonic effects, and are used to calculate phonon frequencies. The cubic force constants $\Phi_{ijk}$ capture phonon-phonon interactions (PPI) that contribute to the broadening and additional shifts of phonon modes. For first-principle force constants calculations, the supercell of 2×2×3 conventional unitcell with 144 atoms were used with a 3×3×2 Monkhorst-Pack $k$-point grid and a plane wave energy cutoff 650 eV. The exchange-correlation energy was also calculated with the Perdew-Burke-Ernzerhof (PBE) functional.

From many-body interactions, the temperature-dependent renormalized phonon frequencies were corrected by calculated the linewidths $\Gamma_\lambda$ and shifts $\Delta_\lambda$ arising from anharmonicity, or phonon-phonon interactions. This required the calculation of the real and imaginary parts of the phonon self-energy

$$\Sigma(\Omega) = \Delta(\Omega) + i\Gamma(\Omega)\,, \tag{3.3}$$

where $\Omega(= E/\hbar)$ is the probing energy. Phonon lifetimes $\tau$ are related to the imaginary part of the self-energy by

$$1/\tau = 2\Gamma_\lambda, \tag{3.4}$$

for mode $\lambda$ evaluated at the harmonic frequency. Given the third order force constants, the imaginary part of the phonon self-energy can be calculated,

$$\begin{aligned}\Gamma_\lambda(\Omega) = \frac{\hbar\pi}{16}\sum_{\lambda'\lambda''} &|\Phi_{\lambda\lambda'\lambda''}|^2 \left\{(n_{\lambda'} + n_{\lambda''} + 1)\right.\\ &\times \delta(\Omega - \omega_{\lambda'} - \omega_{\lambda''}) + (n_{\lambda'} - n_{\lambda''})\\ &\times \left.[\delta(\Omega - \omega_{\lambda'} + \omega_{\lambda''}) - \delta(\Omega + \omega_{\lambda'} - \omega_{\lambda''})]\right\}\end{aligned}\,, \tag{3.5}$$

and the real component is obtained by a Kramers-Kronig transformation

$$\Delta(\Omega) = \mathcal{P}\int \frac{1}{\pi}\frac{\Gamma(\omega)}{\omega - \Omega}\mathrm{d}\omega\,. \tag{3.6}$$

The imaginary component of the self-energy is a sum over all possible three-phonon interactions, where $\Phi_{\lambda\lambda'\lambda''}$ is the three-phonon matrix element determined from the cubic force constants $\Phi_{ijk}$ by the Fourier transform, $n$ is the Bose-Einstein thermal occupation factors counting the number of phonons in each mode, and the delta functions conserve energy and momentum. $\Gamma_\lambda$ and $\Delta_\lambda$ were calculated with a $16 \times 16 \times 16$ $q$-grid.

Compared with the QH model, this s-TDEP method includes higher-order phonon-phonon interactions at elevated temperatures by renormalizing terms in the model

Hamiltonian, adding shifts ($\Delta_\lambda$) of the frequencies perturbatively to the harmonic frequencies. It also reveals the phonon broadening from the imaginary part of the phonon self-energy, which is purely an anharmonic effect.

## 3.4 Results

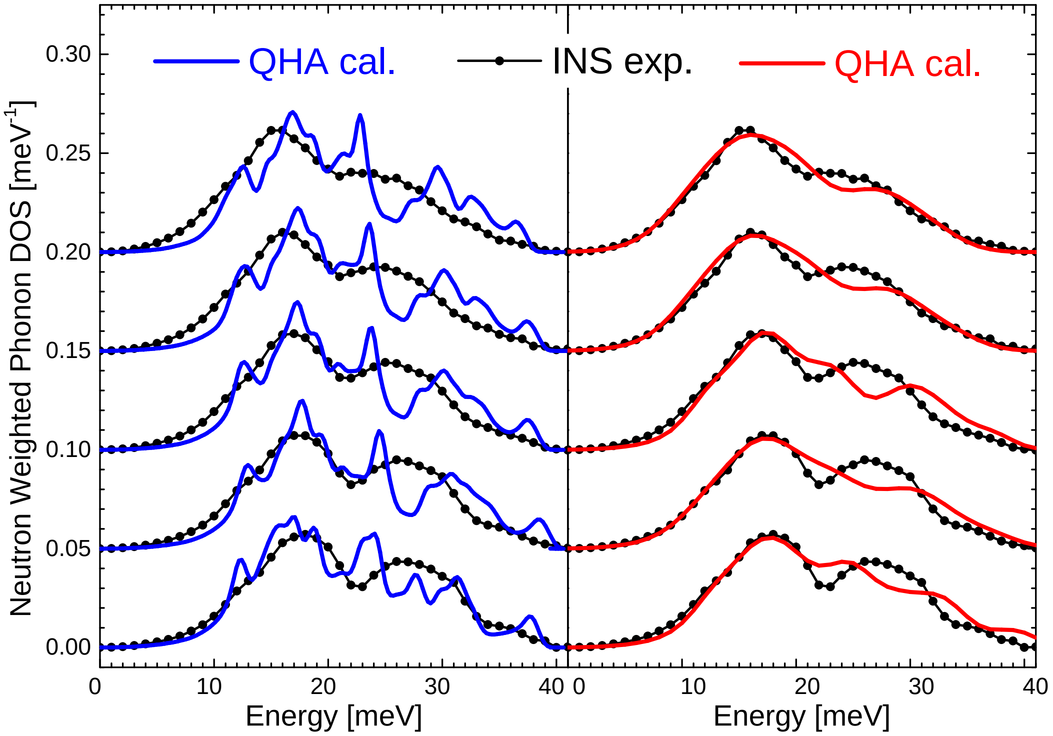

Figure 3.2: Neutron-weighted phonon DOS of $FeGe_2$. Experimental data from INS (black circles) is overlaid with the DOS calculated with the QHA (a, left) before convolution (blue line) and (b, right) after convolution (red line). Curves are normalized to unity and offset for clarity.

Phonon DOS curves measured with INS are shown in Fig. 3.2 (black symbols). By fitting the two main DOS peaks to Lorentzian functions, the temperature dependences of the positions and linewidths of these peaks are shown in Fig. 3.3. They were fitted to linear functions, but the phonon broadening of the high-energy modes included a quadratic term. The low-energy and high-energy modes both soften similarly with temperature. However, the width of the low-energy modes shows little change with temperature, whereas the high-energy modes broaden superlinearly with temperature, indicating shorter phonon lifetimes.

Neutron powder diffraction patterns, obtained from integration of the elastic scattering from the powder samples, were analyzed to obtain lattice constants as function of temperature. Linear thermal expansion of the lattice constants is observed, in agreement with previously reported room temperature data [13]. Lattice parameters and coefficients of thermal expansion are reported in the Supplemental Material.

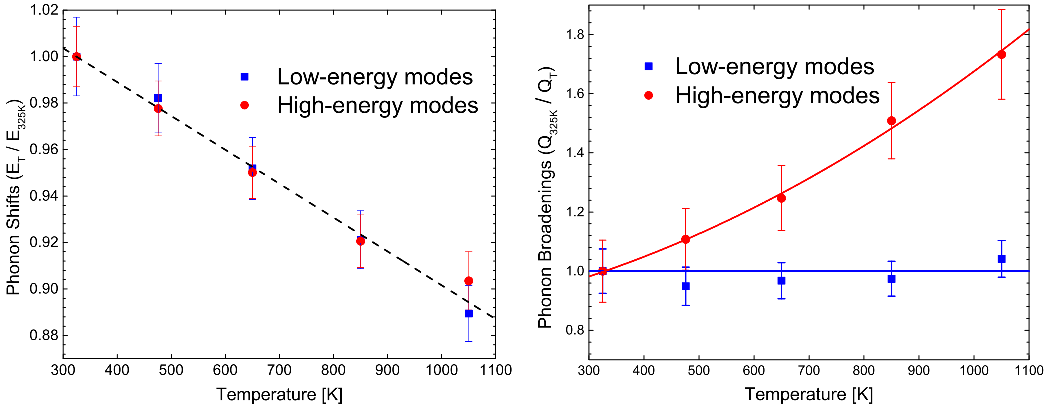

Figure 3.3: Temperature dependence of phonon modes. (a) Phonon shifts and (b) phonon broadenings are shown as functions of temperature. The low- and high-energy modes refer to the two main peaks in the phonon DOS curves shown in Fig 3.2. They are all linear with temperature, except for the phonon broadening of the high-energy modes. Error bars are from the fitting procedure.

Using the experimental lattice constants, the phonon DOS of $FeGe_2$ was calculated with the quasiharmonic approximation as described in Sect. 3.3. By applying the proper weights on the calculated pDOS using Eq. 3.1, and by the convolution with a Gaussian function approximating the instrument resolution, the simulated neutron-weighted phonon DOS was obtained as shown in Fig. 3.2(b, red line). More details on the partial phonon DOS are shown in the Supplemental Material. The calculated, neutron-weighted DOS curves are in good agreement with the experimental measurements in the low-energy region, but there is a noticeable discrepancy in the high-energy modes. The discrepancies become larger with temperature. This is shown more directly by the QHA-calculated phonon DOS before convolution in Fig. 3.2(a), though the discrepancies at high energies, including one gap and a few peaks above 21 meV, are smoothed out by the convolution (Fig. 3.2(b)).

The Fe partial DOS from NRIXS measurements at 325 K is shown in Fig. 3.4. Normalized NRIXS and INS data were used with Eq. 3.1 to obtain the Ge pDOS. The neutron-weight corrected phonon DOS was then obtained at 325 K as shown in Fig. 3.4. It is found that neutron weighting has a negligible influence on the shapes of phonon DOS curves of $FeGe_2$, simplifying interpretations from the neutron-weighted phonon DOS curves at other temperatures.

Figure 3.5 shows phonon dispersions along the [100] direction at 300, 500, and 635 K (a-c). The gray stripe indicates the region at 4 r.l.u. where a cut of intensity as a function of $E$ is taken and shown in (d). Fits to the experimental data with Gaussian functions give the peak positions in (e). The shaded regions in (e) represent the FWHM of the fitted peak. The energy of the high energy mode calculated with the QH approximation is also plotted in (d) in black. Figure 3.6 shows phonon dispersions along the [110] direction at 300, 500, and 635 K (a-c). Again the gray strips indicate the positions of cuts along $E$ that are shown in (d) and (f). The peak energies from Gaussian fits are shown in (e) and (f), with the peak energy from the QH approximation plotted in (g) in black. As is clear from the quasiharmonic DFT calculation overlaying the data in Fig. 3.7, there are many modes present. Acoustic modes can be identified, but their steep slope makes it difficult to see changes in them. As a result, Fig. 3.5(e) and Fig. 3.6(g) show a comparison between the data and the model for only the higher-energy optical modes.

The phonon dispersions are particularly informative for understanding the dynamic behavior of specific modes as a function of temperature. The phonon dispersions are analyzed at r.l.u. $> 2$ to avoid spectral weight from magnon scattering. A closer inspection of the phonons along the [110] direction, shown in Fig. 3.6, shows several modes between 3 and 6 r.l.u. with the highest energy mode near 31 meV. Both high-energy and low-energy modes show similar shifts with temperature, but the high-energy mode broadens more rapidly with temperature than the lower energy mode, becoming more difficult to discern at 635 K. The phonons along the [100] direction (Fig. 3.5) show similar behavior. A distinctive low energy-band does not appear to broaden significantly with temperature, but exhibits a similar thermal shift as the high-energy modes.

## 3.5 Discussion

### Stabilization of the ground state

The electronic energies of $FeGe_2$ were calculated for C16 and C1 (fluorite) crystal structures with non-magnetic, ferromagnetic and anti-ferromagnetic states. The minimum energies for each structure are listed in Table 3.1. The ground state of $FeGe_2$ is found to be the C16 structure in the anti-ferromagnetic state. Magnetism decreases the ground-state energy of the C16 structure significantly compared to the non-magnetic states – the energy of the anti-ferromagnetic state is about 9 meV/atom lower than the ferromagnetic state in the C16 structure, consistent with the calculations by Grechnev, et al[107].

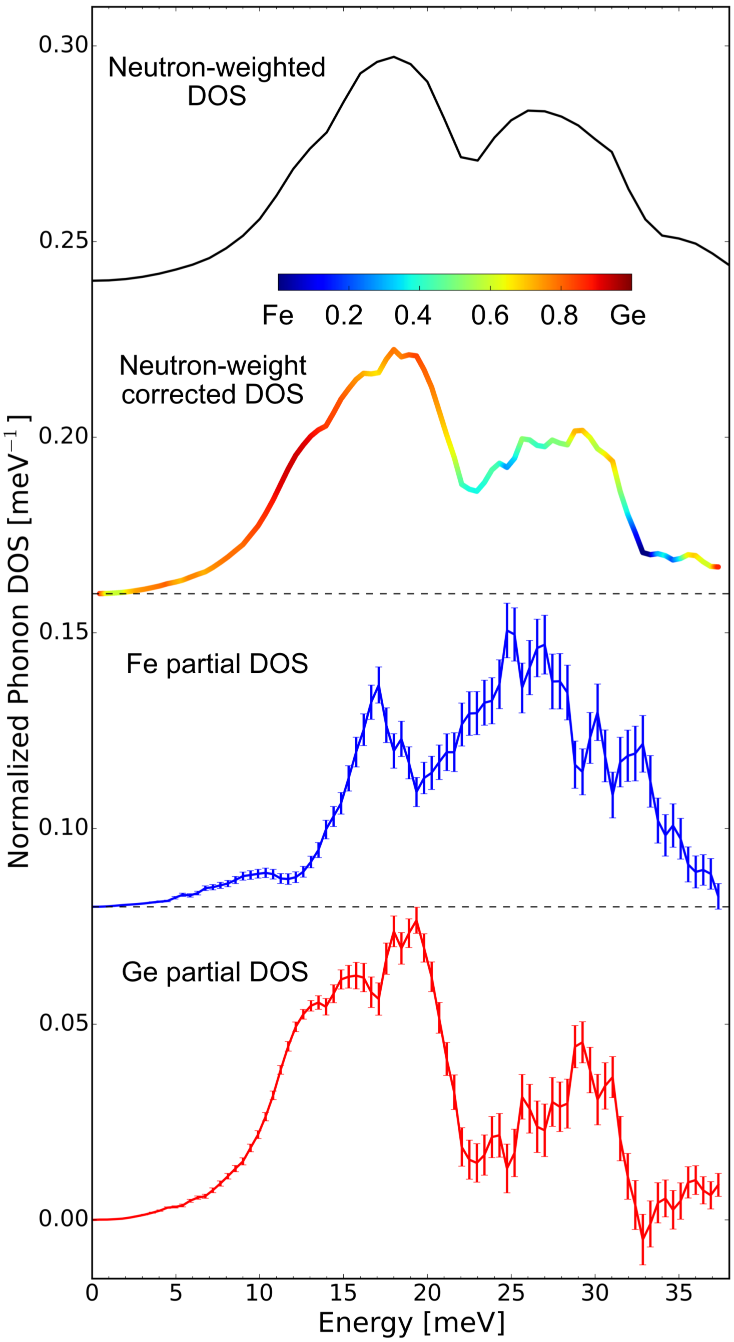

Figure 3.4: Correcting the neutron weighting using Eq. 3.1 by measuring the Fe partial DOS from NRIXS experiments. All data are normalized to unity and at the temperature of 325 K. Error bars are from counting statistics.

### Quasiharmonic approximation

The mode Grüneisen parameter is defined as

$$\gamma_i \equiv -\frac{V}{\epsilon_i}\frac{\partial \epsilon_i}{\partial V} \ , \tag{3.7}$$

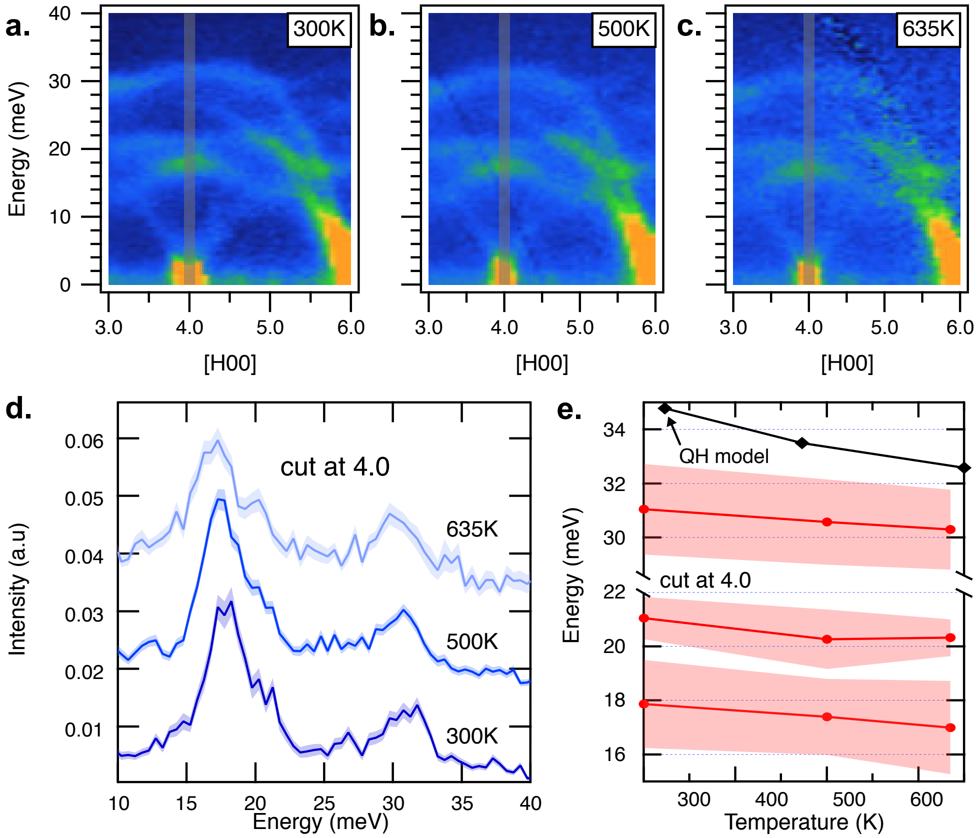

Figure 3.5: Single crystal $FeGe_2$ along the [H00] direction. **(a.)-(c.)** The [H00] direction at 300, 500, and 635K, respectively. The gray stripe indicates the region of the cut shown in (d.) **(d.)** Cut of data at 4.0 r.l.u. is shown for 300K (dark blue), 500K (blue), and 635K (light blue), offset for clarity, with error bars represented by the width of the curve. **(e.)** Positions of low and high energy modes from fits to the experimental data in d. are in red with the shaded region showing the line width approximated by the peak FWHM. The position of the high energy mode predicted by the quasiharmonic model is shown in black.

Table 3.1: Minimum energies for C16 and C1 structure from DFT calculations for non-magnetic, ferromagnetic (FM) and anti-ferromagnetic (AFM) states.

| Crystal structure | Energy [eV/atom] | | |
|---|---|---|---|
| | non-magnetic | FM | AFM |
| C16 | –5.756 | –5.798 | –5.807 |
| fluorite | –5.680 | –5.684 | –5.688 |

where $\epsilon_i$ is the energy of phonon mode $i$, and a mean Grüneisen parameter $\bar{\gamma}$ averages the thermal behavior of all phonons in the Brillouin zone[108]

$$\bar{\gamma} \equiv -\left\langle \frac{V}{\epsilon_i}\frac{\partial \epsilon_i}{\partial V} \right\rangle = -\left\langle \frac{\partial \ln \epsilon_i}{\partial \ln V} \right\rangle . \tag{3.8}$$

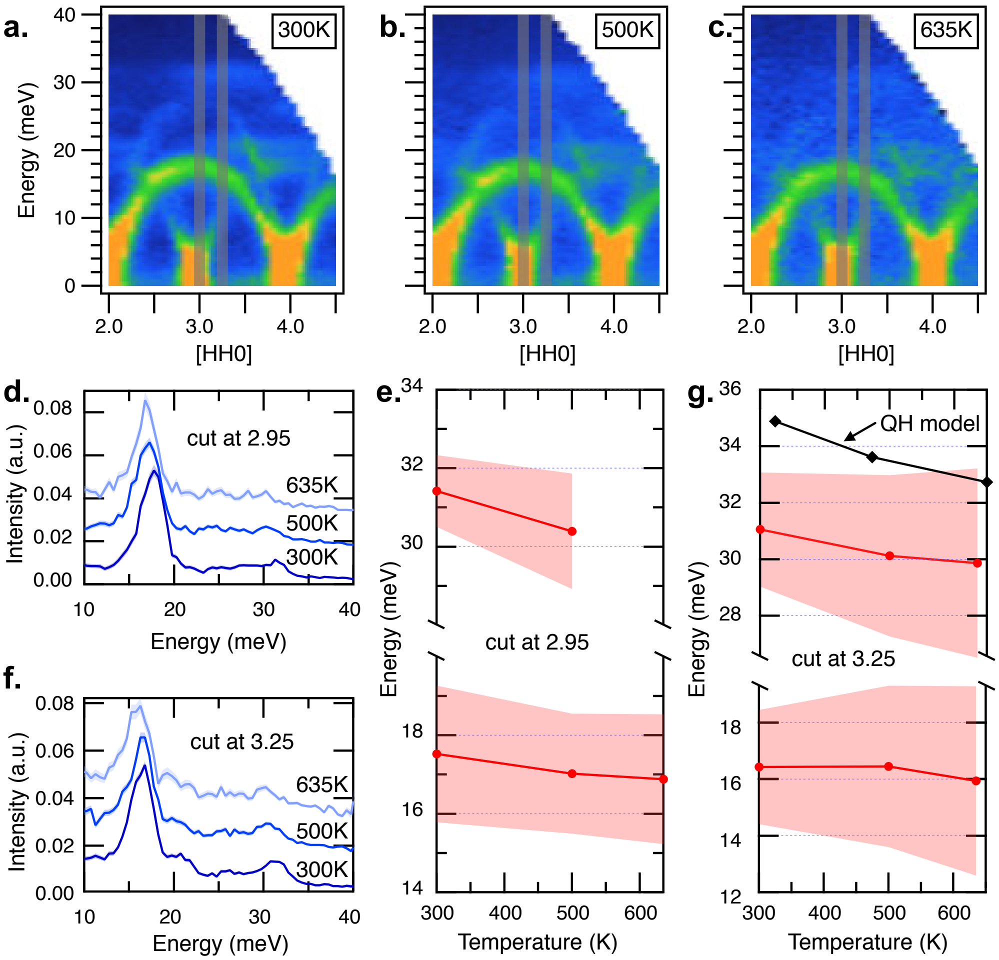

Figure 3.6: Single crystal FeGe$_2$ along the [HH0] direction. (a-c) The [HH0] direction at 300, 500, and 635K, respectively. White spaces indicate regions without detector coverage. The gray stripes indicates the region of the cuts shown in (d) and (f) (d) and (f) Cuts of data at 2.95 and 3.25 r.l.u., respectively, at 300K (dark blue), 500K (blue), and 635K (light blue), offset for clarity, with error bars represented by the width of the curve. (e) and (g) Positions of low and high energy modes from fits to the experimental data in (d) and (f), respectively, are shown in red. The shaded regions show the line width approximated by the peak FWHM. The position of the high energy mode predicted by the QH model is shown in black.

These two conventional Grüneisen parameters are used describe the phonon energy shifts with respect to volume, while the isobaric Grüneisen parameter $\bar{\gamma}_P(T)$ quantifies the temperature dependence of the phonon energy shifts,

$$\bar{\gamma}_P(T) \equiv -\frac{1}{3\alpha(T)} \left\langle \frac{\partial \ln \epsilon_i}{\partial T} \right\rangle \Big|_P . \tag{3.9}$$

A weighted average of the contributions from the low- and high-energy phonon

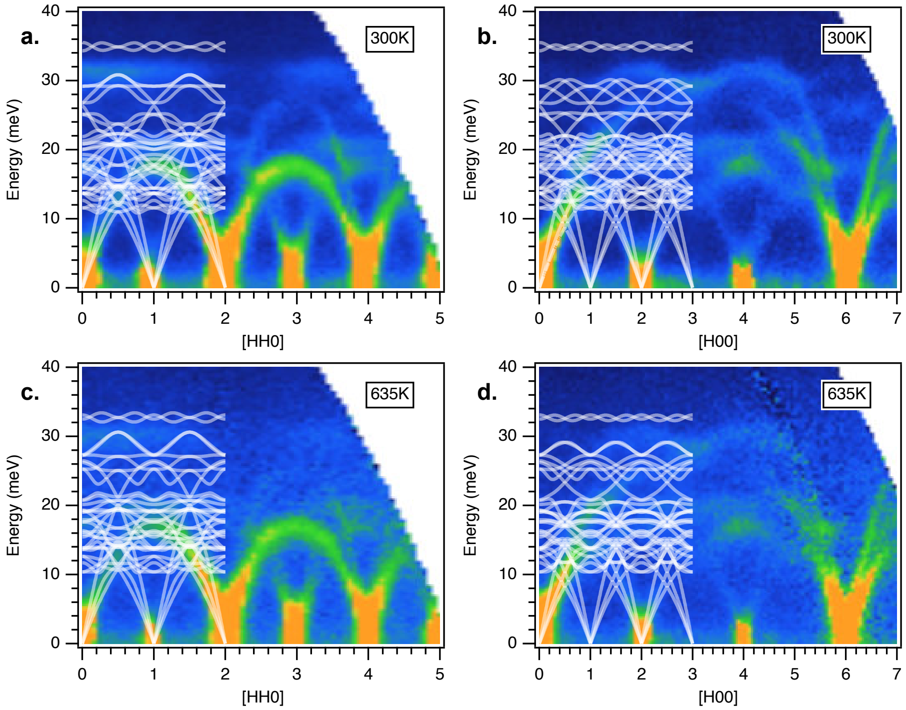

Figure 3.7: Single crystal $FeGe_2$ overlaid with QH calculation. Phonon dispersion curves from the QH calculation are mapped over the measured $S(\mathbf{Q}, E)$. The calculated dispersions are truncated for clarity, but extend further in reciprocal lattice units with the same periodicity. (a) and (b) show the [HH0] and [H00] direction at 300 K, respectively. (c) and (d) show the [HH0] and [H00] direction at 635 K, respectively.

modes (Eq. 3.10) can be used to evaluate $\bar{\gamma}_P(T)$. The positions of the fitted peak centers were used to approximate the phonon mode energies in the low- and high-energy regions as

$$\begin{aligned} \bar{\gamma}_P^{\text{Exp.}}(T) &\simeq -\frac{1}{3\alpha(T)} \left\langle \sum_{i\in\text{low}} \frac{1}{\epsilon_i}\frac{\partial \epsilon_i}{\partial T} + \sum_{i\in\text{high}} \frac{1}{\epsilon_i}\frac{\partial \epsilon_i}{\partial T} \right\rangle \Bigg|_P \\ &\equiv \left\langle n_{\text{low}} \cdot \bar{\gamma}_{P,\text{low}}^{\text{Exp.}} + n_{\text{high}} \cdot \bar{\gamma}_{P,\text{high}}^{\text{Exp}} \right\rangle , \end{aligned} \tag{3.10}$$

where the weights, $n_{\text{low}}$ and $n_{\text{high}}$, were from the areas under the two fitted Lorentzian functions as described at the beginning of Sect. 3.4.

The $\bar{\gamma}_P^{\text{Exp.}}$ was also obtained from the first moment of the phonon DOS curves,

$$\bar{\gamma}_P^{\text{Exp.}} = -\frac{1}{3\alpha(T)} \frac{1}{\bar{\epsilon}} \frac{\partial \bar{\epsilon}}{\partial T}\bigg|_P , \tag{3.11}$$

where $\bar{\epsilon}$ is defined as

$$\bar{\epsilon} = \frac{\int \epsilon g(\epsilon)\, d\epsilon}{\int g(\epsilon)\, d\epsilon}\ . \tag{3.12}$$

Table 3.2 lists the Grüneisen parameters at 650 K from experiment and calculations with the quasiharmonic approximation. There is a non-trivial discrepancy between the experimental and calculated $\bar{\gamma}_P$, implying that the measured isobaric Grüneisen parameter of $FeGe_2$ contains contributions not only from the quasiharmonic model, which is a static volume-dependent approximation, but also from anharmonicity beyond the quasiharmonic model.

Measured phonon dispersion curves are shown along two crystallographic directions in Fig. 3.7, overlaid with dispersions calculated with the quasiharmonic approximation. The quasiharmonic predictions for the highest energy phonon branches differ from the experimental results, perhaps owing to anharmonic effects or magnetic short-range order. The temperature dependences predicted by the quasiharmonic approximation are of the correct magnitude, but not accurate in detail. Similar discrepancies with the quasiharmonic approximation are found for high-energy phonon peaks in the energy cuts shown in Fig. 3.6(e) and Fig. 3.5(g). The quasiharmonic model predicts many low-energy phonon branches, some of which are in agreement with the experiment result. The large number of low-energy modes in $FeGe_2$ impedes the identification of the low-energy modes in Fig. 3.6(e) and Fig. 3.5(e), however. More analyses of phonon dispersions along additional crystallographic directions are given in the Supplemental Material.

### Anharmonic behavior

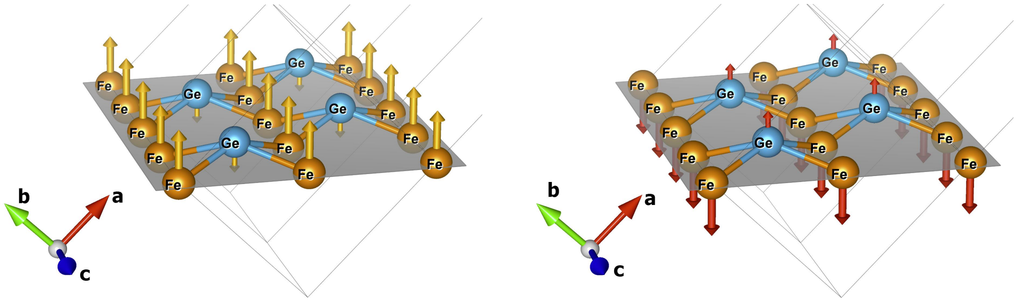

Figure 3.8: Displacement pattern for LO phonons in the [110] direction. The Fe-Ge bonds undergo asymmetrical stretching when Fe (orange) and Ge (blue) atoms move towards (a, green arrows) and away from (b, red arrows) each other.

Table 3.2: Measured and calculated Grüneisen parameter of $FeGe_2$ at 650 K. The calculation used the QHA. The experimental results were obtained from peak positions and the first moment of the measured phonon DOS curves.

| T = 650 K | Calculation | Experiment | | | |
|---|---|---|---|---|---|
| | QHA model | From peak positions | Low-energy modes contribution | High-energy modes contribution | From $\bar{\epsilon}$ |
| $\bar{\gamma}_P$ | 2.37 | 2.69 | 2.75 | 2.60 | 2.46 |

To assess the importance of different contributions to phonon anharmonicity, consider their order with respect to the harmonic contribution $\Phi^{(2)}u^2$ (where $\Phi$ is a potential and $u$ is a displacement)

$$O(\Sigma) = \frac{\Phi^{(3')}}{\Phi^{(2)}}\,u + \frac{\Phi^{(4)}}{\Phi^{(2)}}\,u^2 + \left(\frac{\Phi^{(3)}}{\Phi^{(2)}}\right)^2 u^2 + \ldots \,, \tag{3.13}$$

which shows the well-known result that the cubic term to second order (with $(\Phi^{(3)})^2$ ) is comparable to the quartic term. Equation 3.13 shows that the cubic term to first order (with $\Phi^{(3')}$) could dominate at small displacements. If the phonon potential is an even function of amplitude, this cubic term to first order is forbidden. In a low-symmetry C16 structure of $FeGe_2$, however, this first-order cubic term is allowed for some phonon modes. Its contribution to the phonon self energy is real, and therefore contributes only to the energy shift and not to the broadening [94].

The experimental phonon DOS shows distinctly more broadening of the high-energy part of the spectrum. This could be caused by either lifetime broadenings of individual phonons, or to a distribution of phonon frequency shifts. Examinations of dispersions shown in this text, the Supplemental Material, and many others showed that the dominant thermal effect is the energy broadening of the high-energy phonon modes, although there is also a greater distribution of phonon frequency shifts at high energies than low. The lowest-order term in the phonon self energy having an imaginary part is the cubic to second order [58], and this term is expected to dominate the lifetime broadening.

For a crystallographic site without inversion symmetry, a first-order cubic anharmonicity is possible, and may be important for small displacements. Such a contribution is possible for the LO modes shown in Fig. 3.8 for the C16 structure. The phonon potential is not symmetric under inversion. For first-neighbor Fe-Ge bonds, the Fe-Ge bond length is different if Fe and Ge atoms are moving towards or away from each other, and the change in Fe-Ge bond length differs for the same displacements in the two directions. Anharmonicity of the Fe-Ge bonds is suggested by the measured partial phonon DOS curves. At 325 K, the discrepancy between the phonon modes in experiment and in the quasiharmonic model is greatest around 29 meV (Fig. 3.2). Around 29 meV, both Fe and Ge have a significant contribution to the total phonon DOS (Fig. 3.4).

For further study of the anharmonic behavior, the phonon spectrum function along [HH0] and [H00] directions at 635 K was investigated by *ab initio* DFT calculations

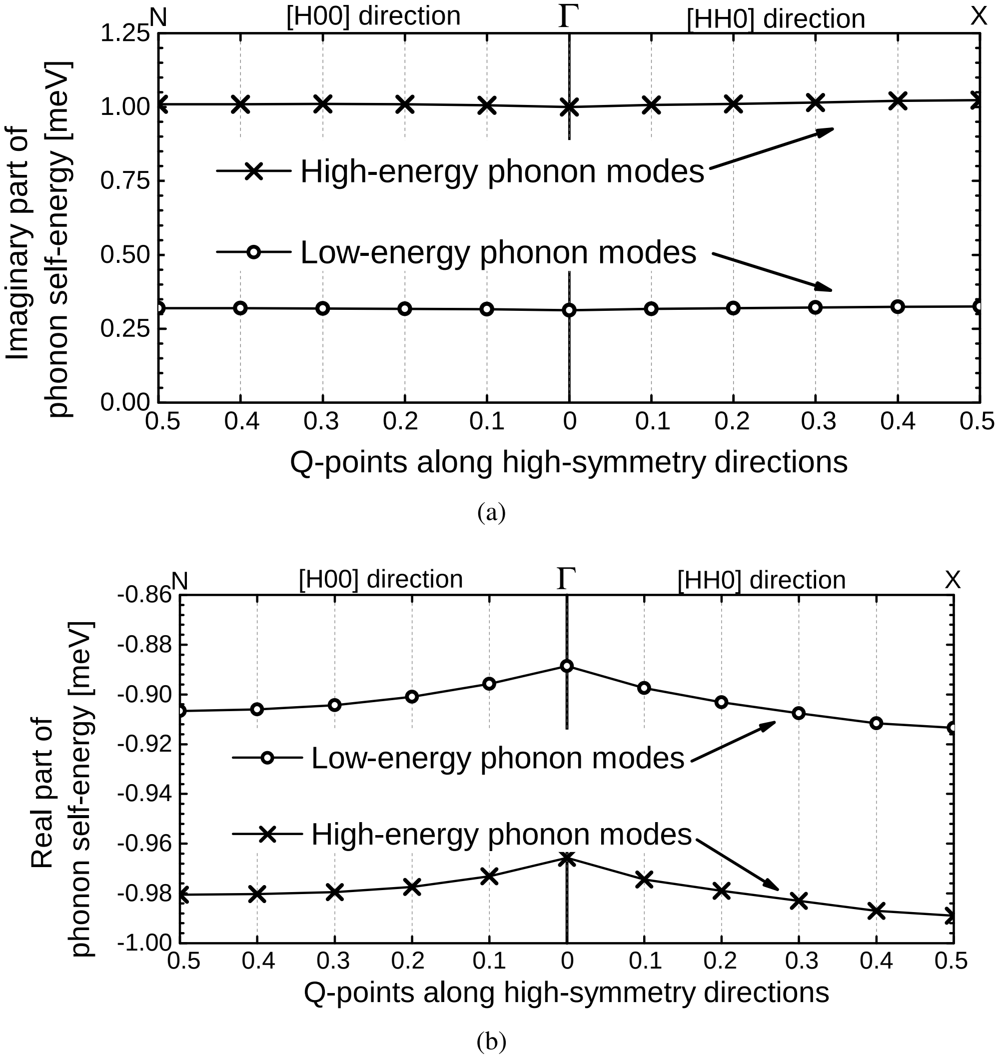

(a)

(b)

Figure 3.9: Phonon self-energy of $FeGe_2$ along [HH0] and [H00] directions at 635 K. (a) Imaginary part of the phonon self-energy which gives the spectral linewidth. (b) Real part of the phonon self-energy which accounts for the phonon energy shifts. It is shown that the high-energy phonon modes (above 21 meV) have much shorter phonon lifetimes than the low-energy modes ($\Gamma_{\mathrm{high}}/\Gamma_{\mathrm{low}} \simeq 4$), while the softening in the high- and low-energy phonon modes are almost the same ($\left|(\Delta_{\mathrm{high}} - \Delta_{\mathrm{low}})/\Delta_{\mathrm{high}}\right| \simeq 7.5\%$).

with the stochastic temperature-dependent effective potential technique (sTDEP). Third-order force constants were used to calculate the imaginary and real part of the phonon self-energy. As shown in Fig. 3.9, they do not vary much. The imaginary part shows that the high-energy phonon modes (above ~ 21 meV) have much shorter phonon lifetimes than the low-energy phonon modes, which is indicated by Eq. 3.4, while the real part shows that their averaged energy shifts are almost the same. This is consistent with the results obtained from the phonon DOS measurements and single crystal data. Beyond the QHA, the cubic anharmonicity plays an important role in the phonon broadening in the high-energy modes of $FeGe_2$. More details on the phonon spectrum function and phonon self-energy at specific **Q**-points along these two directions can be found in the Supplemental.

### Heat capacity and entropy

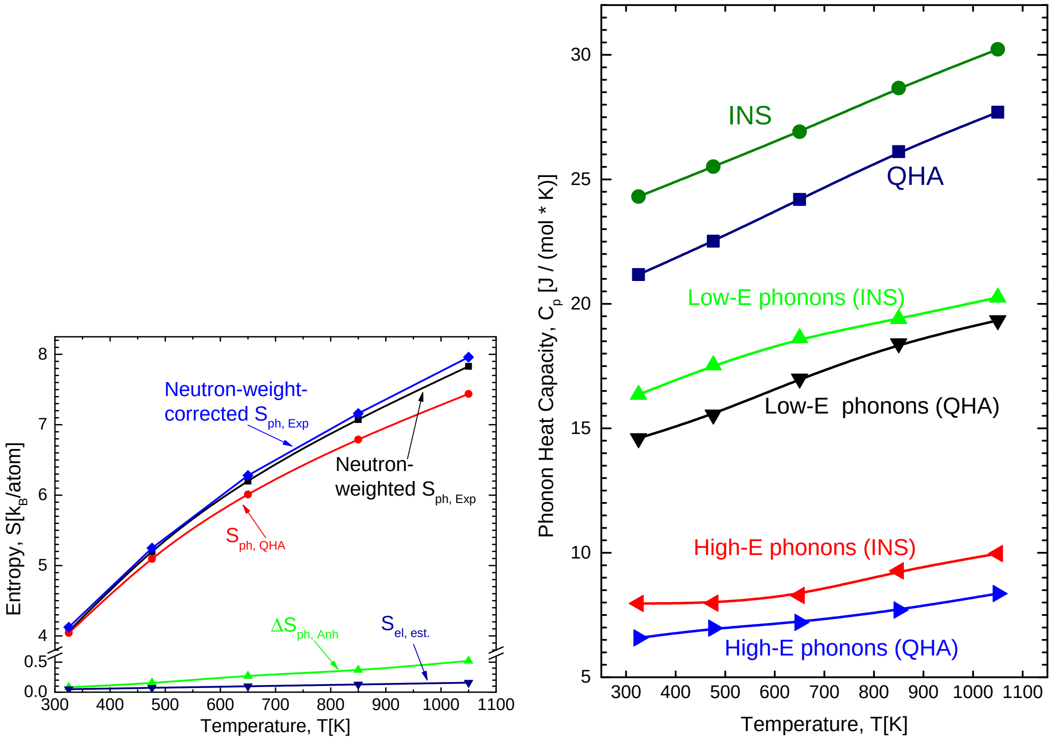

Figure 3.10: Temperature dependence of the entropy in $FeGe_2$ and the phonon contribution to its heat capacity. (a) Components of the entropy[12] of $FeGe_2$ and their temperature dependence. $S_{\text{ph,Exp}}$ are from the neutron-weighted (in black) and neutron weight-corrected (in blue) phonon DOS respectively. $S_{\text{ph,QHA}}$ (in red) are from the calculated phonon DOS using the quasiharmonic approximation. The anharmonic contribution ($\Delta S_{\text{ph,Anh}}$, in green) was obtained by $\Delta S_{\text{ph,Anh}} = S^{\text{nw}-\text{corrected}}_{\text{ph,Exp}} - S_{\text{ph,QHA}}$. The small entropy from electrons ($S_{\text{el,est.}}$, in navy) was estimated with $S_{\text{el,est.}} = \frac{\pi}{3} k_B T n(\epsilon_F)$, where $n(\epsilon_F)$ is the electronic DOS at the Fermi level in the ground state. (b) Temperature dependence of the phonon contribution to the heat capacity, calculated from measured phonon DOS by the INS experiments and QH approximation. Magnetic contributions, not shown here, are expected at low temperatures.

Figure 3.10 shows the temperature dependence of the thermal properties of $FeGe_2$.

The phonon entropy $S_{\mathrm{ph}}$ was obtained from the phonon DOS $g(E)$ by

$$S_{\mathrm{ph}} = 3k_{\mathrm{B}} \int dE g(E) \left[(n+1)\mathrm{ln}(\mathrm{n}+1) - \mathrm{nlnn}\right], \tag{3.14}$$

where $n$ is the Planck distribution at the temperature $T$,

$$n = \frac{1}{e^{E/(k_{\mathrm{B}}T)} - 1}. \tag{3.15}$$

The heat capacity is then derived from

$$C_{\mathrm{P}} = T \left.\frac{\partial S}{\partial T}\right|_{\mathrm{P}}. \tag{3.16}$$

Components of the phonon entropy (calculated from the phonon DOS as described previously [12]) are presented in Fig. 3.5. The phonon entropy was calculated from the neutron-weighted DOS at all temperatures, and the neutron weight-corrected DOS at 300 K, which has a somewhat higher ratio of high-energy modes to low-energy modes. The small discrepancy between these two results at 300 K was scaled to other temperatures, assuming the same number of modes in the high-energy and low-energy regions of the phonon DOS. The results are compared to quasiharmonic calculations with a phonon DOS that changes with thermal expansion in the Supplemental Material. The agreement is good at 300 K, but the effect of anharmonicity is to increase the phonon entropy by approximately 0.5 $k_{\mathrm{B}}$/atom at 1050 K, much larger than the estimated electronic contribution.

At 325 K, the phonon contribution to the heat capacity is 25.0 J/(mol · K), while the magnetic and electronic contributions are 7.3 J/(mol · K) and 1.4 J/(mol · K) respectively[9]. The majority of the heat capacity comes from the phonons, but the magnetic and electronic parts are not negligible. As the temperature increases, however, the static magnetic order in $\mathrm{FeGe_2}$ will disappear and the magnetic heat capacity will decrease to near zero. For example, at 1020 K, the magnetic contribution is almost zero, while the estimated electronic heat capacity is 4.4 J/(mol · K) and the phonon heat capacity is 31.6 J/(mol · K) as shown in Fig. 3.10. As a result, phonons contribute a growing fraction of the heat capacity of $\mathrm{FeGe_2}$ as the temperature increases (from 74% at 325 K to 87% at 1020 K).

Phonons were also divided into the low- and high-energy parts such that their numbers of states were in the ratio 2:1, approximated by the weights used in Eq. 3.10. The phonon heat capacities calculated from these two parts are shown separately in Fig. 3.5. The QH model fails to predict the heat capacity for both energy regions, although the gap of the low-energy part is narrowing with temperature.

## 3.6 Conclusion

Phonon anharmonicity was studied in paramagnetic $FeGe_2$ between 300 and 1050 K. Inelastic neutron scattering was used to measure the phonon spectrum from a powdered sample from 300 to 1050 K, and $^{57}$Fe nuclear resonant inelastic X-ray scattering was used to measure the partial phonon DOS of $^{57}$Fe to correct for differences in the neutron weights for phonon scattering by Fe and Ge. Comparisons with phonon calculations by DFT in the quasiharmonic approximation were successful for the low-energy part of the vibrational spectrum, but the high-energy part showed obvious discrepancies. Thermal shifts of the phonon DOS were measured, and agreed in part with the DFT calculations in the quasiharmonic approximation. There was a modest difference in the average isobaric Grüneisen parameters from computation and experiment, however.

Phonon dispersions were measured by inelastic neutron scattering on a single crystal of $FeGe_2$ at 300, 500, and 635 K. The large number of dispersions made detailed analysis challenging, but some thermal shifts and broadenings of individual phonons were identified. The high-energy phonon dispersions showed more broadening and variations in their thermal shifts than the low-energy modes. Some of this energy shift of high-energy modes could be caused by a cubic anharmonicity to first order, for which the Fe-Ge first neighbor bond can have an asymmetrical potential in the C16 structure. Nevertheless, the average thermal trends of phonons in $FeGe_2$ do not differ dramatically from the predictions of the quasiharmonic approximation, and this approximation may be useful for understanding some thermophysical properties even though it does not predict correctly the individual phonon frequency shifts, and of course, the lifetime broadening of the phonon energies. Below 700 K $FeGe_2$ is modestly anharmonic, but the anharmonic contributions were interpretable.

## 3.7 Supplemental Material

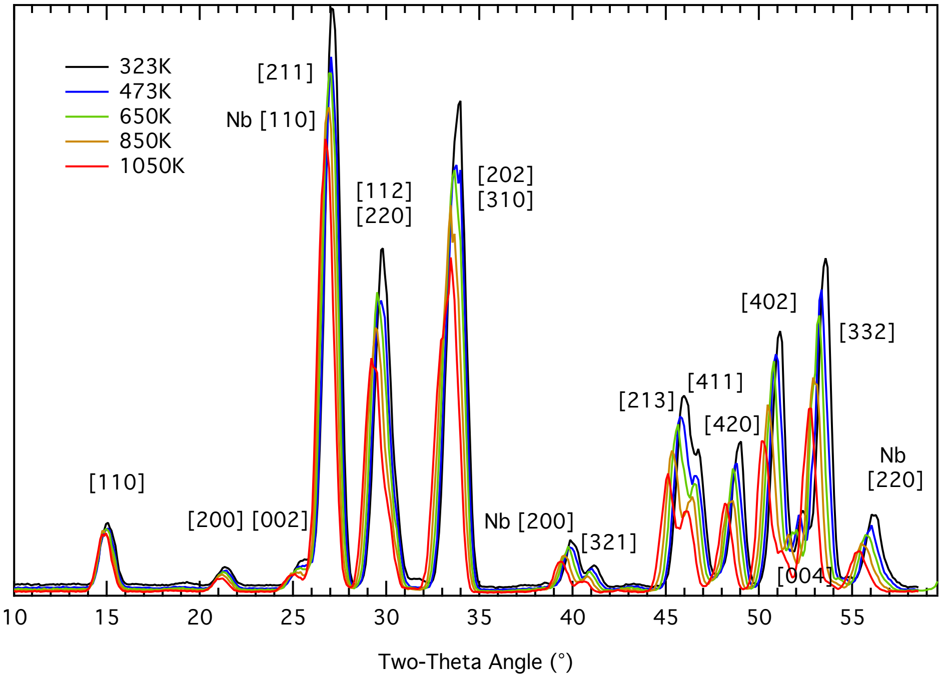

Figure 3.11: Neutron powder diffraction patterns of polycrystalline $FeGe_2$ at 323, 476, 650, 850 and 1050 K. Diffraction patterns were obtained from elastic scattering in the experimental data sets containing the inelastic neutron scattering measurements used for the phonon densities of states. Intensity is plotted as a function of $Q$, with each colored curve corresponding to a different temperature. The [hkl] index of each peak is labeled. Three peaks from the Nb sample holder are indexed.

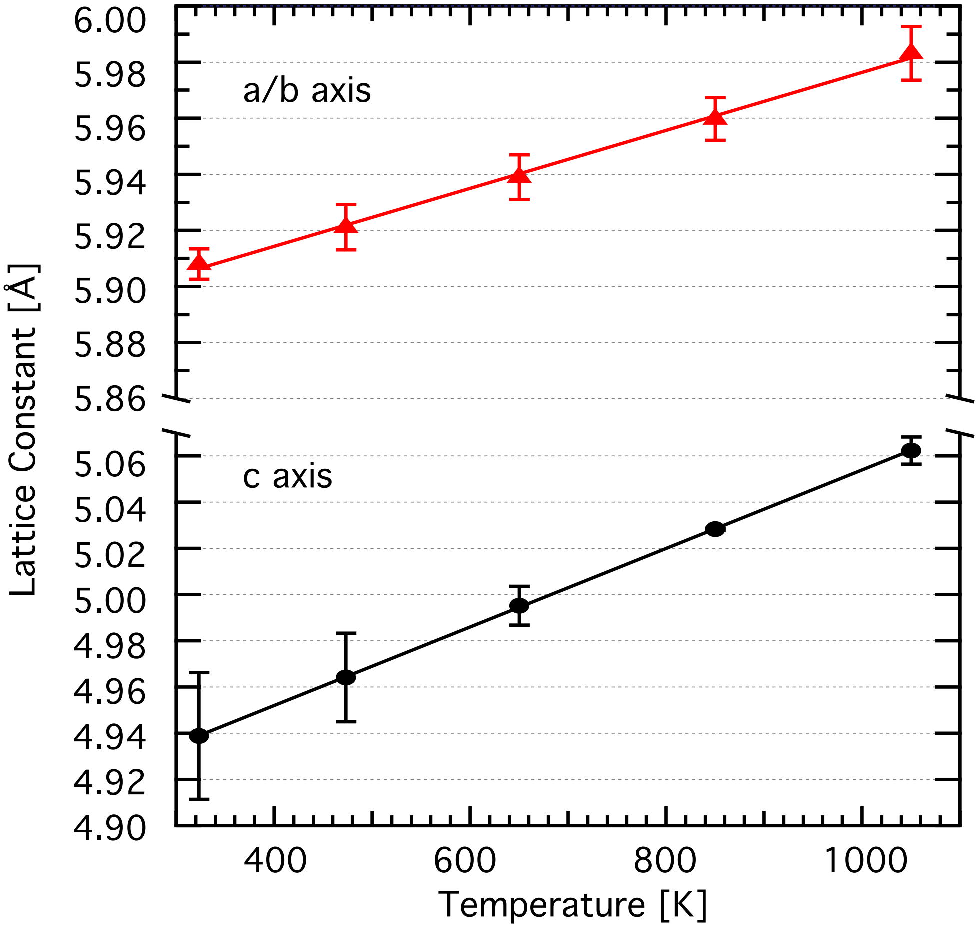

Figure 3.12: Lattice constants of $FeGe_2$. The lattice constants for $a = b > c$ are shown as functions of temperature. A linear thermal expansion of the lattice constants is observed, in agreement with previously reported room temperature data [13].

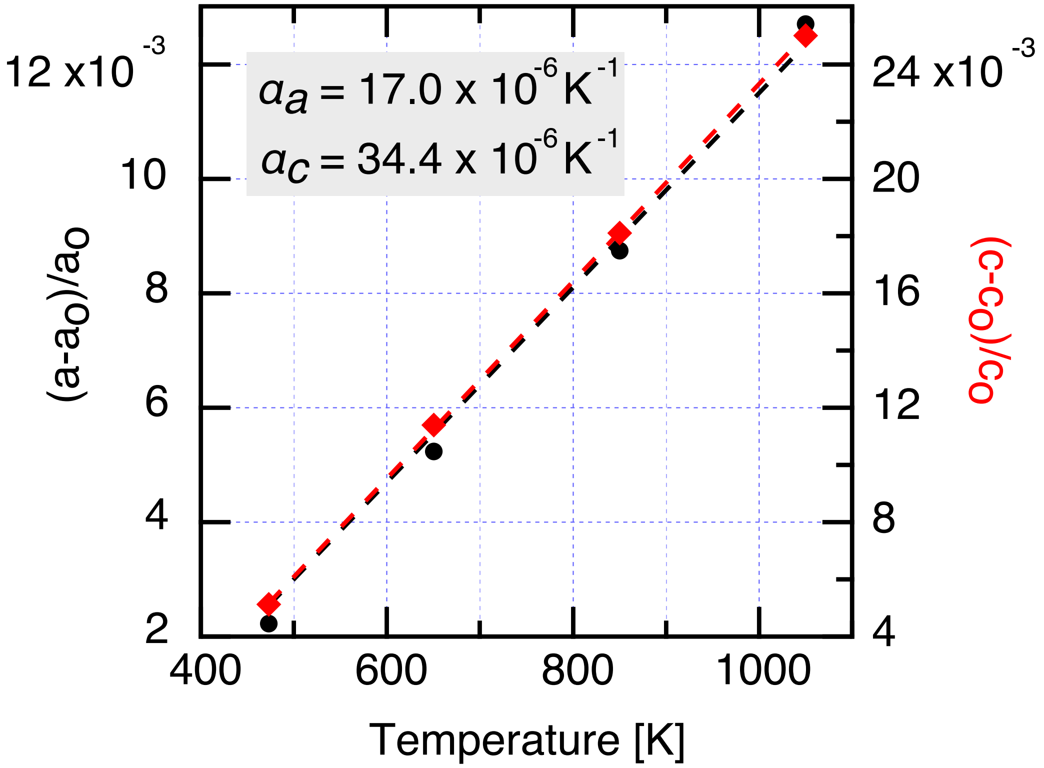

Figure 3.13: Thermal Expansion of FeGe$_2$. The coefficient of thermal expansion is obtained by fitting the data in Fig. 3.12 to $\frac{a_T - a_o}{a_o} = \alpha_a \cdot (T - T_o)$ where $a_o$ represents the lattice parameter at $T = T_o$ ($T_o$=323 K) and $\alpha_a$ is the linear thermal expansion coefficient of the lattice parameter in the $a$ direction. This is a first order temperature independent approximation of the thermal expansion coefficient. The linear thermal expansion in the $c$ direction is found by application of the same equation with $a$ replaced by $c$.

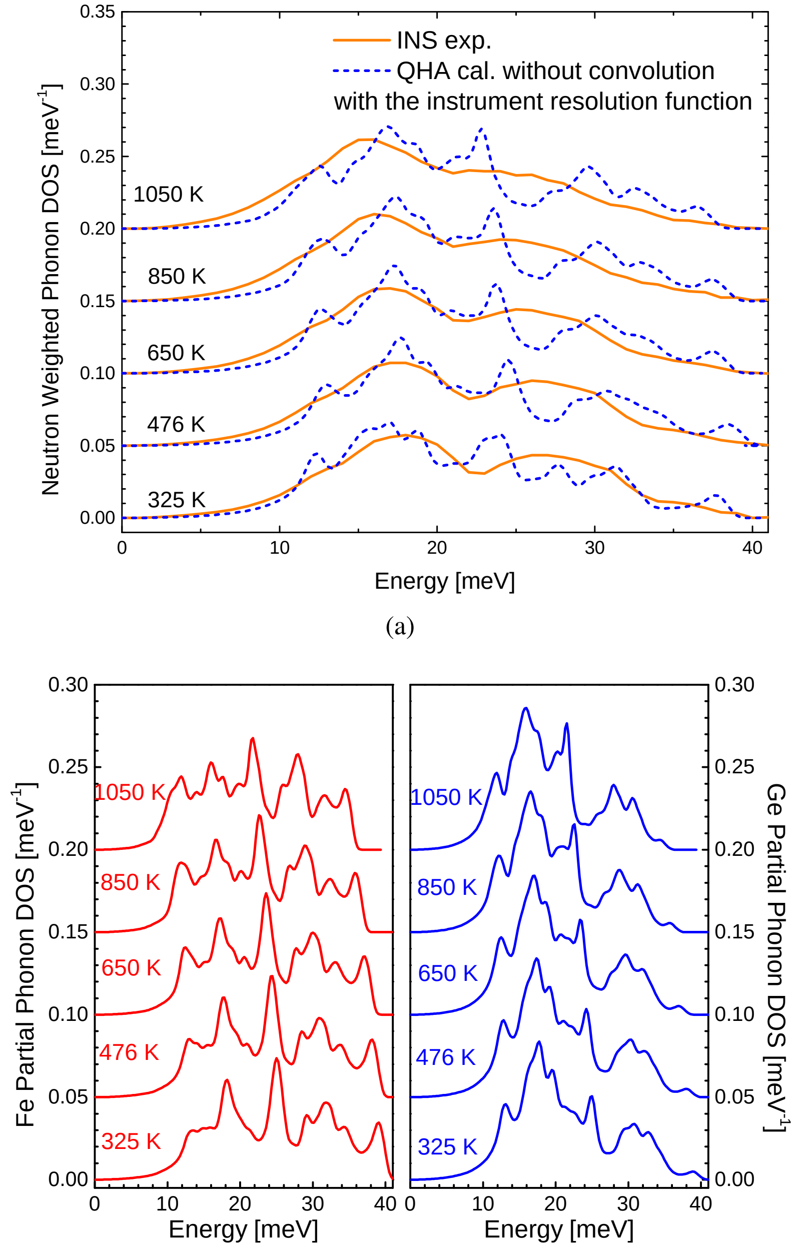

(a)

(b)

Figure 3.14: Detailed computational results with quasiharmonic approximation. (a) Calculated phonon DOS (dash line) without convolution with the instrument resolution function. Experimental data from INS (solid line) is also presented for comparison. (b) Calculated Fe (left panel, in red) and Ge (right panel, in blue) partial phonon DOS. Curves are normalized to unity and offset for clarity.

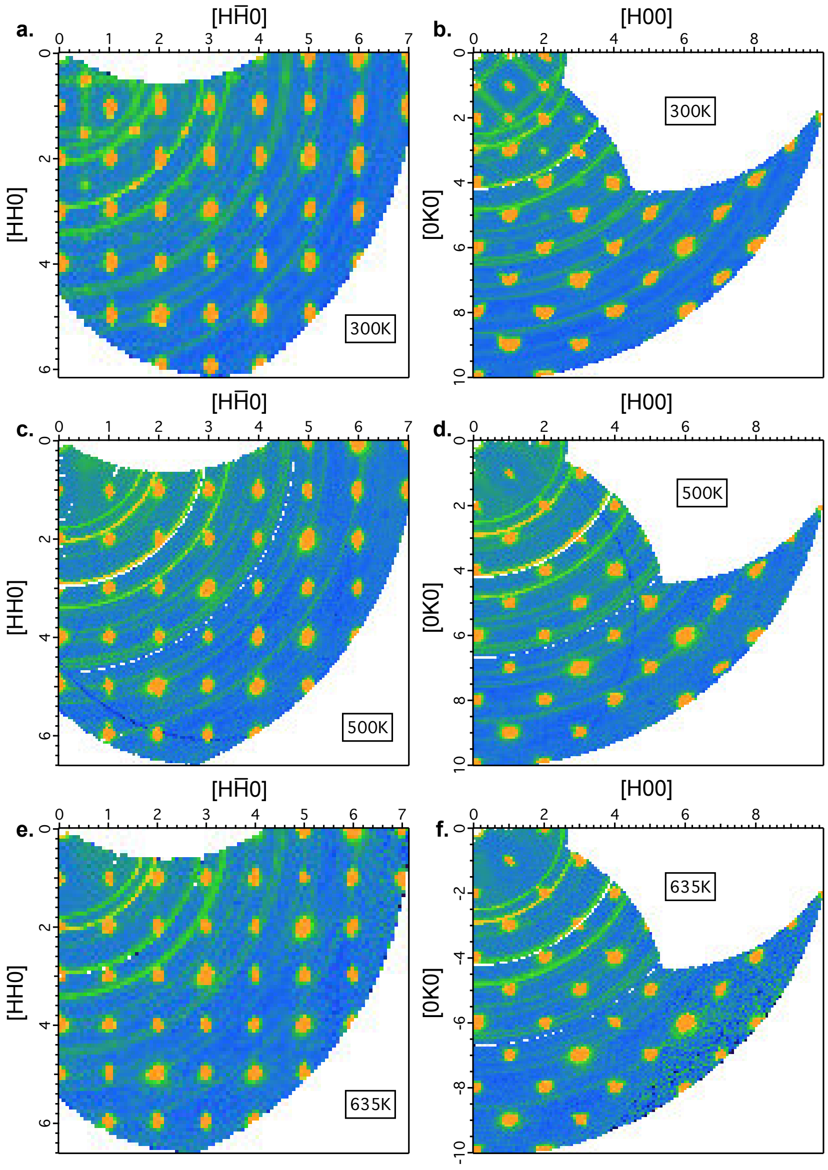

Figure 3.15: Elastic scattering from single crystal FeGe$_2$. The crystal was oriented in the [00L] zone axis, with the [HK0] crystallographic plane horizontal. Slices of the elastic plane were obtained by integrating from -1 to 1 meV in energy, and over the L-direction from -0.15 to 0.15. For the tetragonal symmetry of the crystal, the [0K0] and [H00] directions are crystallographically equivalent, as are the [HH0] and [H$\overline{H}$0] directions. (a) and (b) 300 K, (c) and (d) 500 K (e) and (f) 635 K.

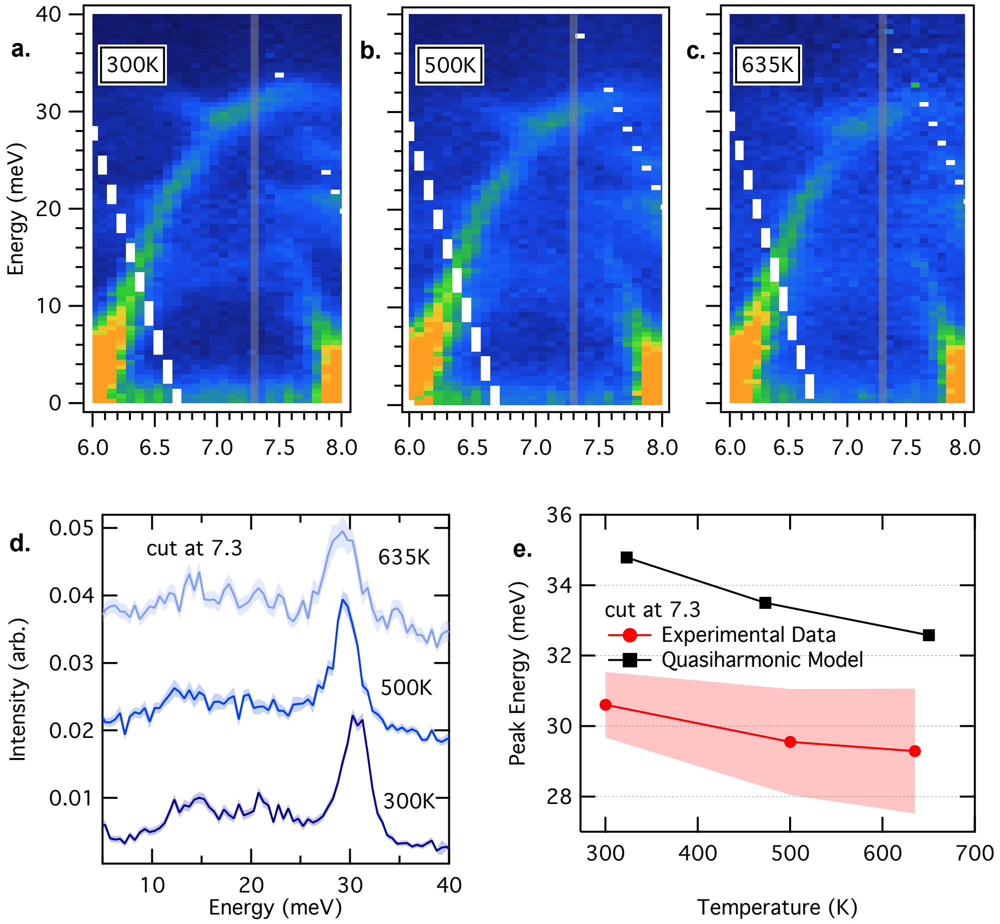

Figure 3.16: Inelastic scattering from single crystal $FeGe_2$ along the [0K0] direction. (a-c) The [0K0] direction at 300, 500, and 635 K, respectively. The gray stripe shows the region of the cut shown in panel (d). (d) Cut of data at 7.3 r.l.u. is shown for 300 K (dark blue), 500 K (blue), and 635 K (light blue), offset for clarity, with error bars shown by the width of the curve. (e) Centers of the high-energy modes from fits to the experimental data in panel (d) are in red, with the shaded region showing the peak FWHM. The center of the high-energy mode predicted by the quasiharmonic model is shown in black.

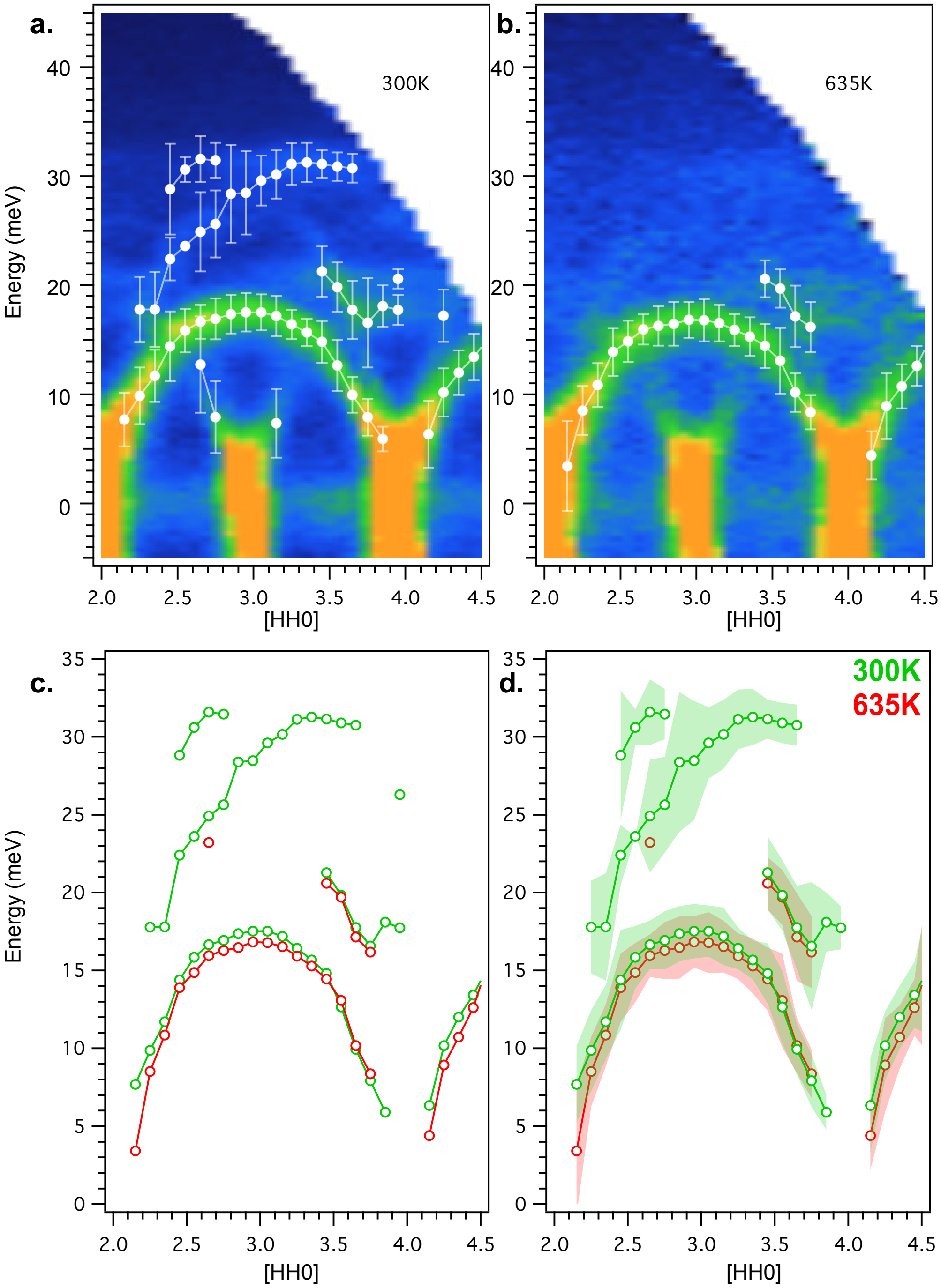

Figure 3.17: Inelastic scattering from single crystal $FeGe_2$ along the [HH0] direction. (a) and (b) The [HH0] direction at 300 and 635 K with the positions of the peaks indicated by white circles and bars showing the FWHM from the fits. (c) The peak centers at 300 and 635 K, showing thermal shifts of the dispersions. (d) The same peak centers in (c), but with shaded regions indicating the FWHM, showing approximately the change in thermal broadening with temperature.

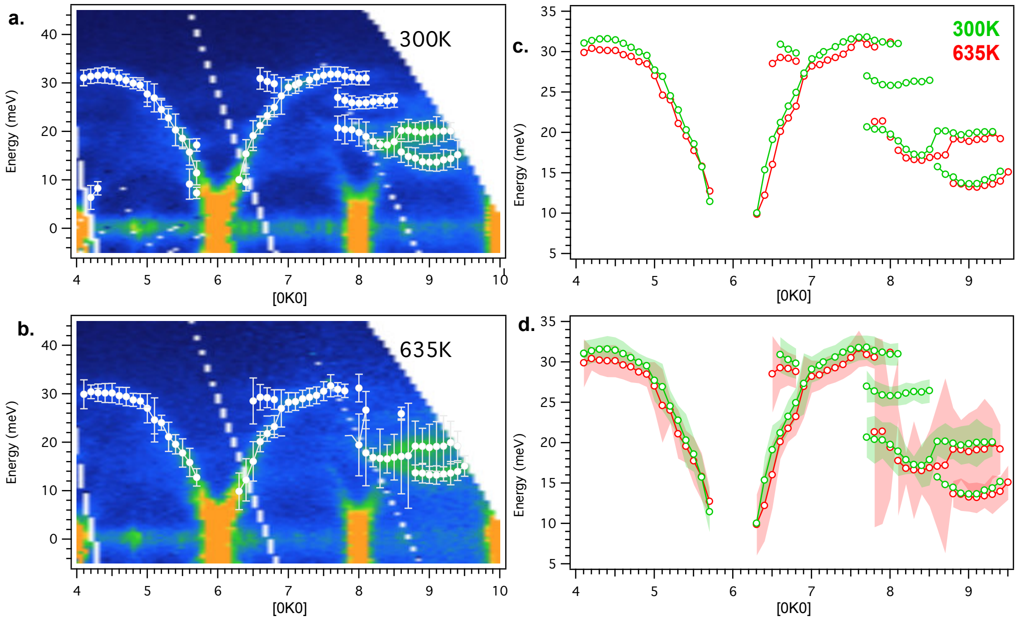

Figure 3.18: Inelastic scattering from single crystal $FeGe_2$ along the [0K0] direction. (a) and (b) The [0K0] direction at 300 and 635 K, with peak centers indicated with white circles, and bars showing the FWHM obtained from the fits. (c) The peak centers at 300 and 635 K, showing thermal shifts of the dispersions. (d) The same peak centers in (c), but with shaded regions indicating the FWHM, showing approximately the change in thermal broadening with temperature.

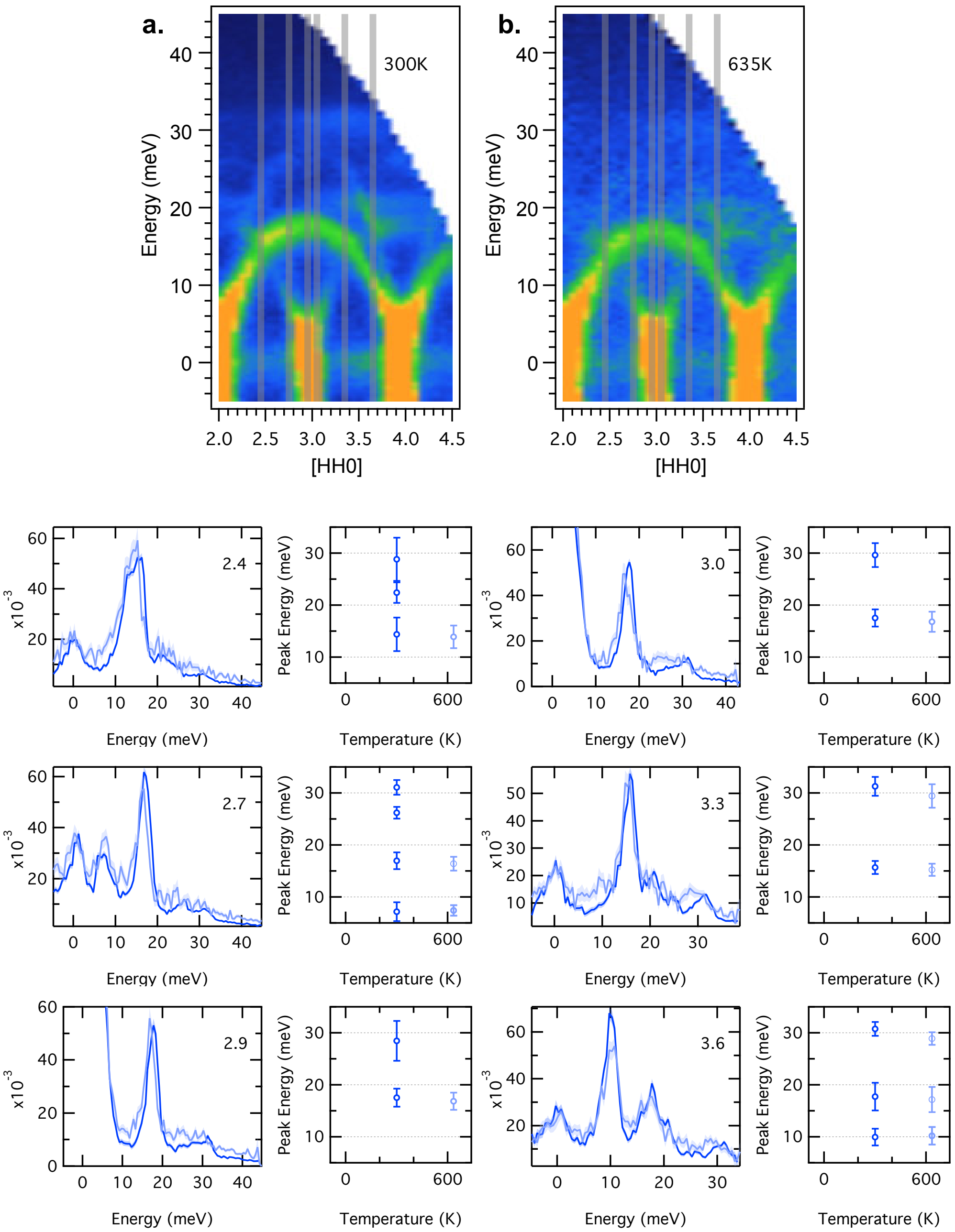

Figure 3.19: Inelastic scattering from single crystal $FeGe_2$ along the [HH0] direction. (a) and (b) The [HH0] dispersions at 300 and 635 K. The gray stripes indicate the regions of the cuts below. Cuts of data at the r.l.u. indicated on the plots are shown for 300 K (dark blue) and 635 K (light blue). To the right of each plot are shown centers of the peaks (identified in corresponding color), with bars showing the FWHM of the peaks.

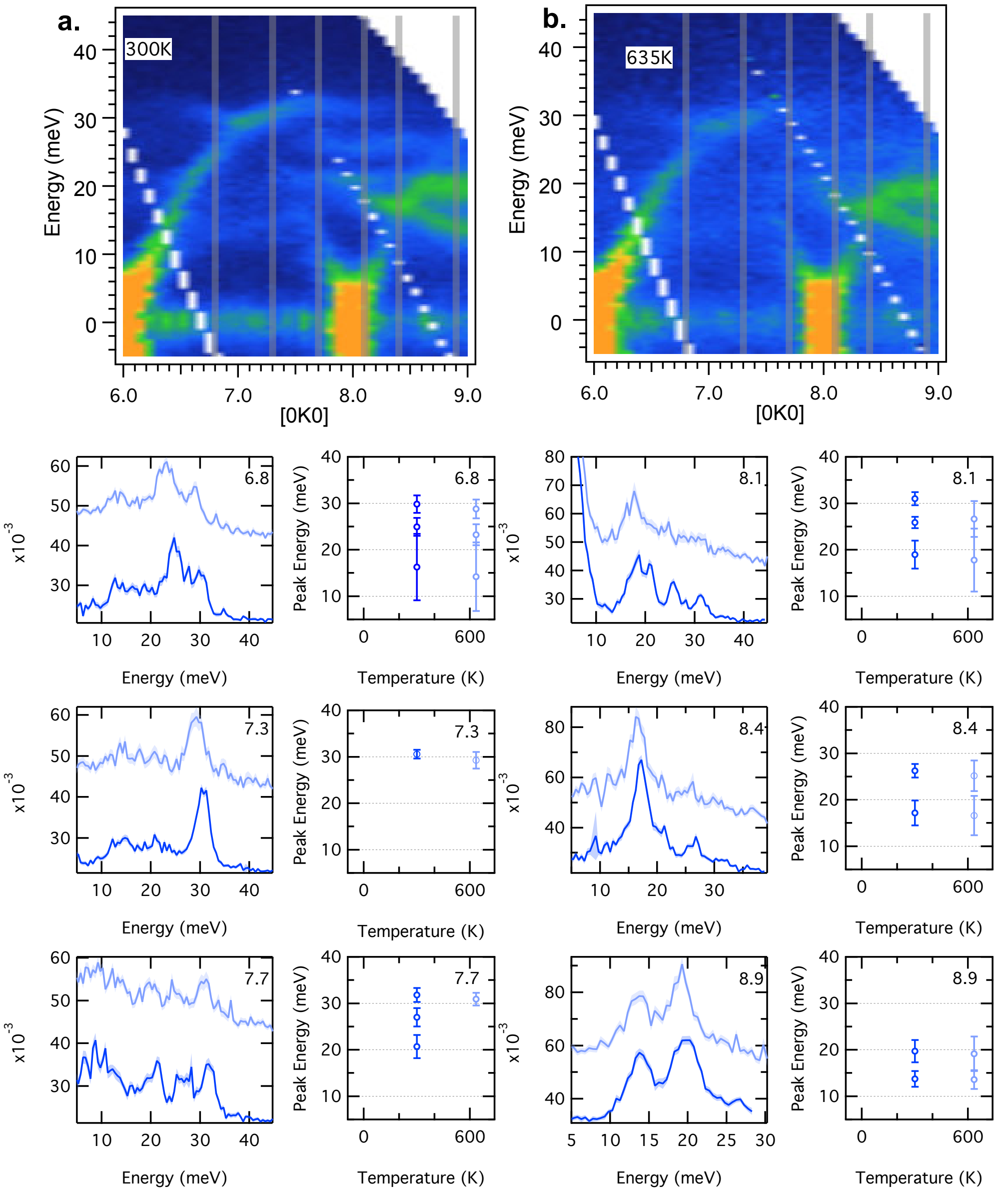

Figure 3.20: Inelastic scattering from single crystal FeGe$_2$ along the [0K0] direction. (a) and (b) The [0K0] dispersions at 300 and 635 K. The gray stripes indicate the regions of the cuts below. Cuts of data at the r.l.u. indicated on the plots are shown for 300 K (dark blue) and 635 K (light blue). To the right of each plot are shown centers of the peaks (identified in corresponding color), with bars showing the FWHM of the peaks.

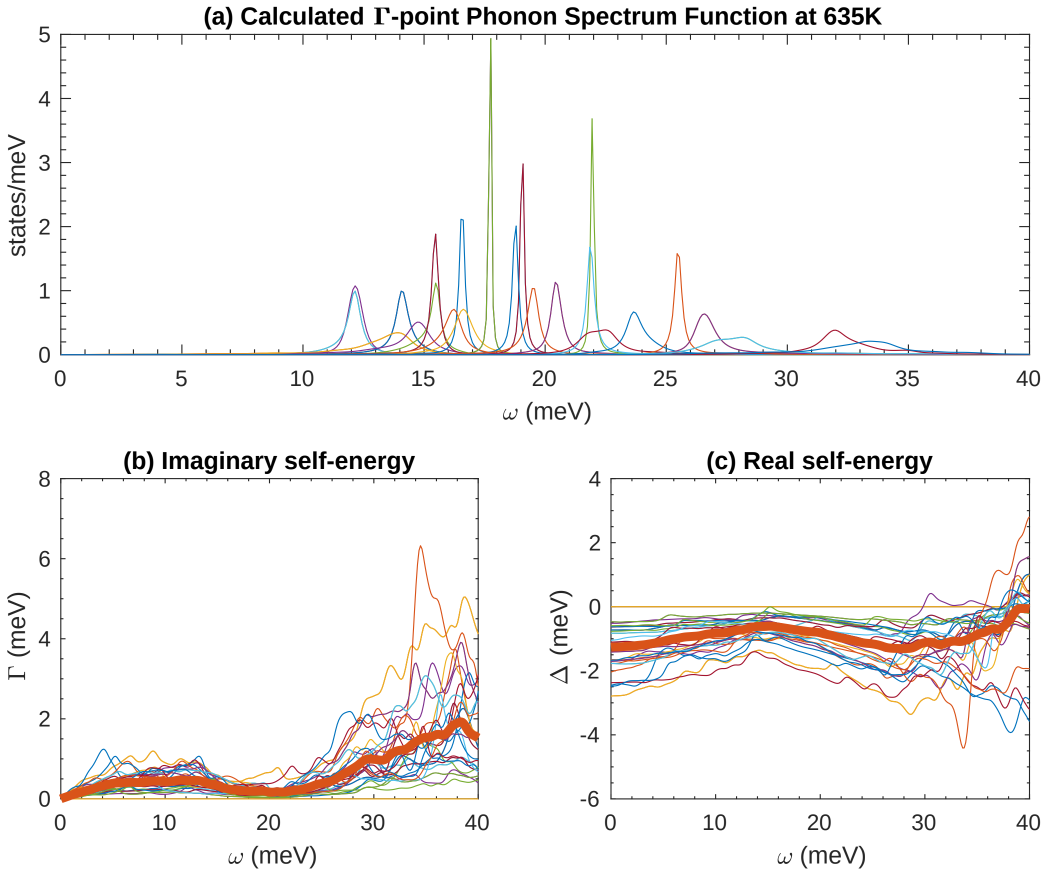

Figure 3.21: Calculated phonon self-energy of Γ-point phonons in $FeGe_2$ at 635 K. (a) The phonon spectrum at Γ at 635 K was calculated by *ab initio* stochastically initialized temperature-dependent effective potential method (s-TDEP) method. Colors represent different phonon branches. (b, c) Third-order force constants were used to calculate the imaginary part and the real part of the phonon self-energy. The averaged values are shown by the bold red line. This is consistent with the results in our main text obtained from the phonon DOS measurements and single crystal data. And it shows that QHA is not enough, because the cubic anharmonicity plays an important role in the phonon broadening in the high-energy modes of $FeGe_2$. More results are shown in the next figure.

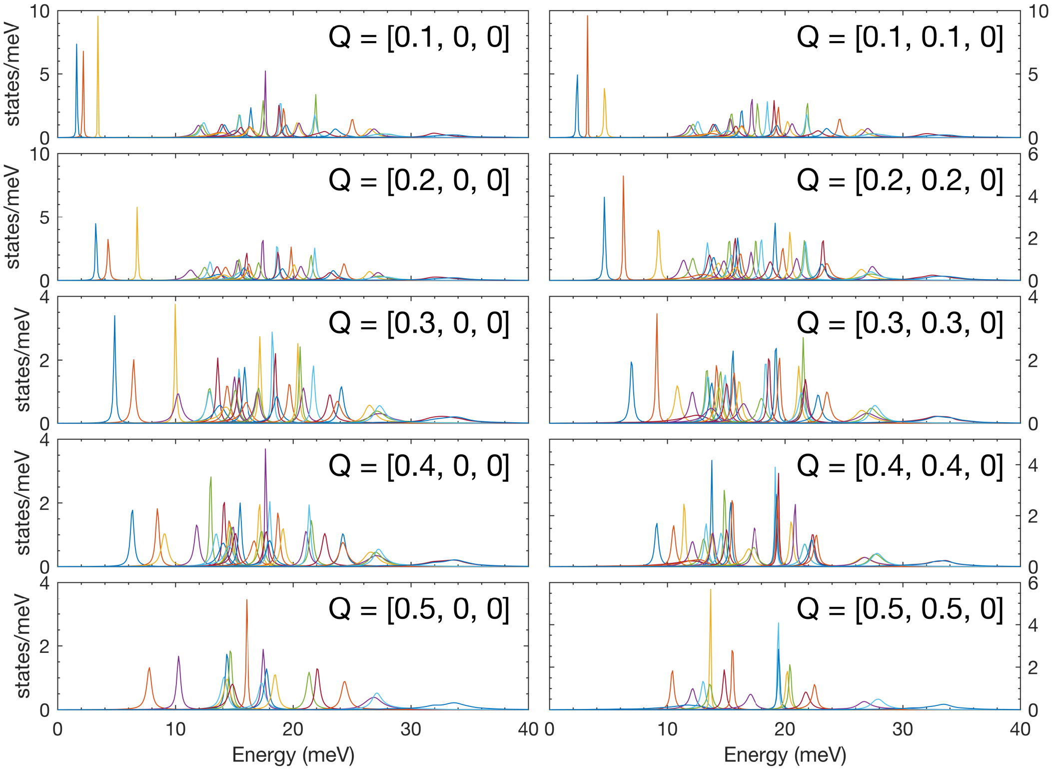

Figure 3.22: Calculated phonon spectrum function along [HH0] and [H00] directions in $FeGe_2$ at 635 K. The phonon spectra along the two symmetry lines at 635K were calculated by *ab initio* stochastically initialized temperature-dependent effective potential method (s-TDEP) method. Colors represent different phonon branches.

## *Chapter 4*

# THE ANHARMONIC ORIGIN OF THE GIANT THERMAL EXPANSION OF SODIUM BROMIDE

### 4.1 Main Text

Thermal expansion, a fundamental thermophysical property, originates primarily from a competition between the elastic energy of expansion and the phonon entropy, which usually increases beyond harmonic behavior as a solid expands. Thermal expansion can be calculated readily in the quasiharmonic approximation (QHA), which assumes that phonon frequencies depend only on volume [109–114]. The QHA theory of thermal expansion is textbook content and is logically self-consistent. It ignores explicit anharmonicity, where phonon frequencies also change with temperature at a fixed volume [115, 116]. Some calculations include anharmonicity as a small correction to the QHA, but the relative importance of anharmonicity is not yet settled [110, 117].

We recently found that the QHA gave the wrong sign for the temperature dependence of most phonons in silicon [106]. This shows that the QHA is physically incomplete, even though it did predict correctly the thermal expansion. Here we report a more compelling inelastic neutron scattering (INS) experiment to test predictions of phonons and thermal expansion in a different material, sodium bromide (NaBr). Like other alkali halides with the rocksalt structure [59, 118, 119], NaBr has received special attention owing to its cubic structure and highly ionic bonding.

The INS data from a single crystal of NaBr were acquired with the time-of-flight spectrometer, ARCS [43], at the Spallation Neutron Source at the Oak Ridge National Laboratory, using neutrons with an incident energy of 30 meV. Data were collected from 201 rotations of the crystal in increments of 0.5° about the vertical [001] axis. Data reduction gave the 4D scattering function $S(\mathbf{Q}, \varepsilon)$ [120, 121], where $\mathbf{Q}$ is the 3D wave-vector and $\varepsilon$ is the phonon energy (from the neutron energy loss). Nonlinearities of the ARCS instrument were corrected with a small linear rescaling of the $q$-grid, calibrated by the positions of 45 *in situ* Bragg diffractions. After subtracting the background from measurements on an empty can at the same temperature, and removing multiphonon scattering with the incoherent approximation, the higher Brillouin zones were folded back into an irreducible wedge in the first

Brillouin zone to obtain the spectral intensities shown in Fig. 4.1. The *S*upplemental Material describes the experiment and data analysis in more detail.

The QHA uses an explicit dependence of phonon frequencies on volume into the Helmholtz free energy

$$\begin{aligned} & F^{\mathrm{QHA}}(T,V) \\ = \; & U_0(V) + \sum_{\mathbf{q},j} \left[ \frac{\hbar\omega_{\mathbf{q},j}}{2} + k_{\mathrm{B}} T \ln\left(1 - e^{-\frac{\hbar\omega_{\mathbf{q},j}}{k_{\mathrm{B}}T}}\right)\right] , \end{aligned} \tag{4.1}$$

where $U_0(V)$ is the ground-state internal energy without any vibrational contribution and the term $k_{\mathrm{B}} \ln[...]$ includes the entropy that depends on volume through the individual phonon frequencies $\omega_{\mathbf{q},j} = \omega_{\mathbf{q},j}(V)$ (for the $j$-th phonon branch at wavevector $\mathbf{q}$). The finite-displacement method, as implemented in PHONOPY [103], was used to obtain phonon frequencies for different volumes by density functional theory (DFT) calculations with the VASP package [66–68, 122]. The equilibrium volume at a given temperature $T$ was obtained by minimizing $F^{\mathrm{QHA}}(T,V)$ with respect to volume $V$, keeping $T$ as a fixed parameter. Figure 4.2 shows how the QHA fails to predict both the magnitude and shape of the thermal expansion curve of NaBr, even at room temperature.

Anharmonic behavior was calculated by the stochastically-initialized temperature dependent effective potential method (sTDEP) [39–41, 123]. In sTDEP, the Born-Oppenheimer molecular dynamics potential energy surface of NaBr was evaluated by a Monte Carlo sampling of the phase space of atom positions. The forces on atoms were fitted to a model Hamiltonian

$$\begin{aligned} \hat{H} = \; & U_0 \; + \sum_i \frac{\mathbf{p}_i^2}{2m_i} + \frac{1}{2!} \sum_{ij} \sum_{\alpha\beta} \Phi_{ij}^{\alpha\beta} u_i^\alpha u_j^\beta \\ + \; & \frac{1}{3!} \sum_{ijk} \sum_{\alpha\beta\gamma} \Phi_{ijk}^{\alpha\beta\gamma} u_i^\alpha u_j^\beta u_k^\gamma , \end{aligned} \tag{4.2}$$

by DFT calculations on various configurations of displaced atoms by stochastic sampling of a canonical ensemble, with Cartesian displacements ($u_i^\alpha$) normally distributed around the mean thermal displacement. The $U_0$ is a fit parameter for the baseline of the potential energy surface. The quadratic constants $\Phi_{ij}$ capture not only harmonic properties, but their temperature dependence accounts for quartic and higher nonharmonic parts of the potential. These temperature-dependent $\{\Phi_{ij}\}$ were used to calculate phonon frequencies. The cubic force constants $\Phi_{ijk}$ capture the broadening and additional shifts of phonon modes, discussed below.

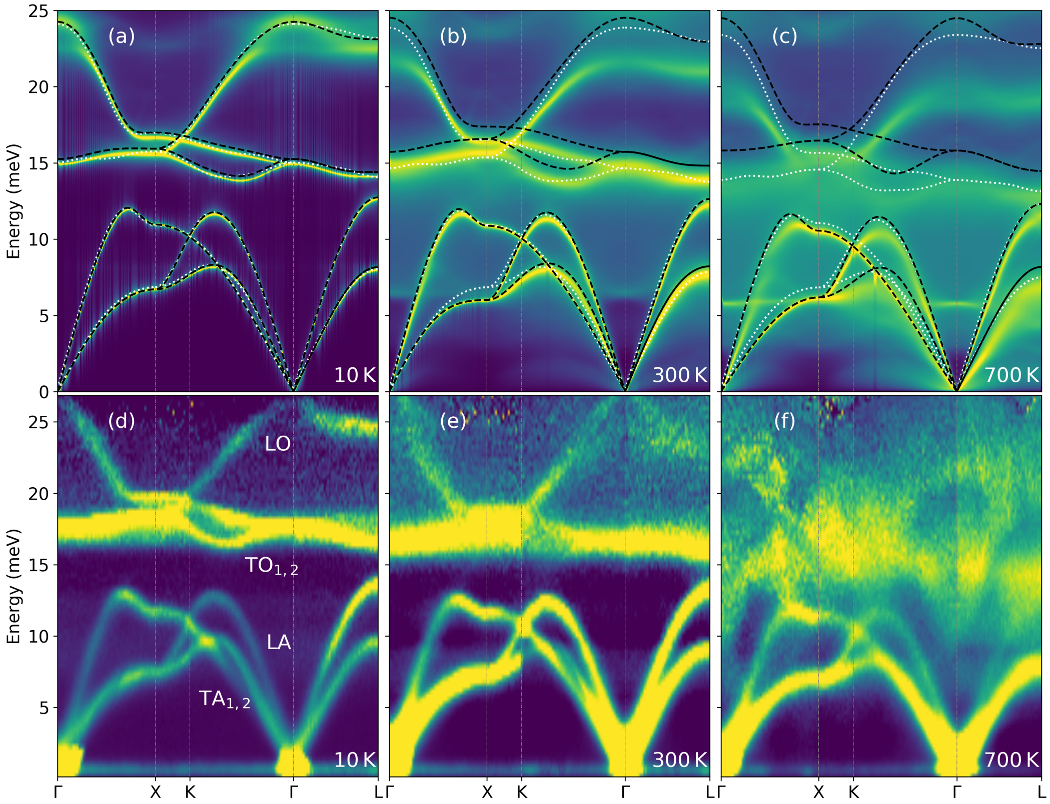

Figure 4.1: Comparison between computational (QHA and fully anharmonic) and experimental (INS) results on phonon dispersions of NaBr. (a-c) Phonons in NaBr calculated with the QHA (white dotted line), with only the second-order force constants from sTDEP (black dashed line), and from the full phonon spectral function (logarithmic intensity map) from sTDEP. Temperatures are labeled in the panels. (d-f) Corresponding 2D slices through the four-dimensional scattering function $S(\mathbf{Q}, \varepsilon)$, where $\varepsilon = \hbar\omega$, along high symmetry lines in the first Brillouin zone.

For a given temperature, the Helmholtz free energy $F(T, V)$ was calculated for different volumes $V$ as [124]

$$F(T, V) = U_0(T, V) + F_{\mathrm{vib}}(T, V) , \tag{4.3}$$

where $U_0(T, V)$ is the baseline from Eq. 4.2. The equilibrium volumes were obtained by minimization of the Helmholtz free energy at $T$, giving the results shown in Fig. 4.2. These equilibrium volumes are in good agreement with experimental measurements, although there are deviations at higher temperatures. Details of the calculations of equilibrium volumes and phonon dispersions are given in the *Supplemental Material*.

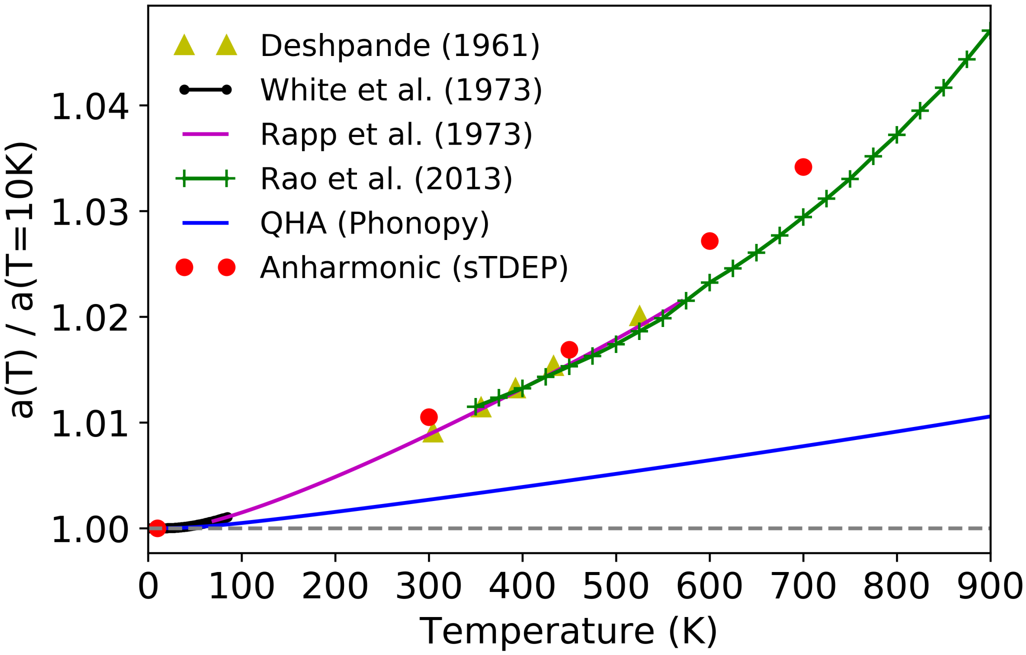

Figure 4.2: Thermal expansion of NaBr. The *ab initio* QHA (blue solid line) and anharmonic calculations (red solid circles) are compared with experimental results [14–17]. There is a large discrepancy between the measurements and the QHA predictions, while results from the sTDEP method are in close agreement with the experiments.

Some calculated phonon spectral weights are compared to experimental measurements in Fig. 4.1 along directions of high symmetry. At 10 K, all calculations agree with each other and with the experimental measurements. At higher temperatures, the acoustic dispersions below 14 meV show some softening, especially at 700 K, but are not broadened so much as the optical modes. The optical modes show large broadening at 300 K, and major changes in shape at 700 K. The temperature dependence of the optical dispersions is largely captured by the spectral weight calculated by sTDEP, but only a minor part of the softening is predicted by the QHA calculations (and none of the broadening owing to its assumption of non-interacting modes). The quadratic term from sTDEP (with $\Phi_{ij}^{\alpha\beta}$ in Eq. 4.2) was used to calculate the dispersions shown as black dashed lines in Fig. 4.1a-c. By itself, this term does not reproduce the thermal phonon softening. The largest contribution to the temperature shift of the spectral weight is from the real part of the cubic term, obtained as a Kramers–Kronig transformation of the imaginary part of the self-energy as explained in the *Supplemental Material* with Eq. 51. The imaginary part of the phonon self-energy from this cubic term is responsible for the surprisingly-large energy broadening of the longitudinal optical (LO) phonons at 300 K and especially at 700 K.

The experimental inelastic neutron scattering (INS) measurements (see Fig. 4.1) were fitted to give the energy shifts of LO phonons presented in Table I. The QHA accounts for only a small part of the experimental shifts, but the anharmonic calculations are much more successful. The spectral intensities at the $L$-point are shown in Fig. 4.3a. All phonons at the $L$-point soften and broaden significantly with temperature. Spectra from the longitudinal acoustic (LA) and transverse optic (TO) phonon modes merge into one broad peak at 700 K. The longitudinal optical (LO) peak broadens significantly, but its large thermal softening is still evident. Figure 4.3b shows that the real part of the self-energy of the LO phonon at the $L$-point is approximately –3.5 meV at 700 K, so phonon-phonon anharmonicity dominates the thermal shift of this mode (the LO mode has a phonon energy of 19 meV at the $L$-point from sTDEP). The *Supplemental Material* shows some of the spectral weights in more detail. There are differences between experiment and the sTDEP calculations at 700 K, especially halfway between $\Gamma$ and $L$ between 16 and 23 meV. Some anharmonic effects in NaBr are too large to be predicted accurately by the sTDEP method.

To understand the origin of the anharmonicity at 700 K, the cubic irreducible force constants (IFCs) for the three-body interactions within the first ten coordination shells were individually set to zero while recalculating phonon lineshapes at different **Q**. Figure 4.3c shows how two related IFCs dominate the lineshapes. They correspond to the nearest-neighbor cubic interactions of degenerate triplets (NaNaBr and/or NaBrBr) in the [100] direction (i.e. along the Na-Br bond direction). (By translational invariance, $\Phi^{\alpha\alpha\alpha}_{\text{NaNaBr}} = -\Phi^{\alpha\alpha\alpha}_{\text{NaBrBr}}$.) When these force constants are switched off, the phonon lineshapes revert to narrow Lorentzian functions typical of weakly anharmonic solids, and these Lorentzian peaks are at energies similar to those from the QHA calculations. The dominance of $\Phi^{\alpha\alpha\alpha}_{\text{NaNaBr}} = -\Phi^{\alpha\alpha\alpha}_{\text{NaBrBr}}$ on the phonon anharmonicity was found for phonons at all other points in reciprocal space, as shown in the *Supplemental Material*.

The physics of thermal expansion requires volume and temperature derivatives of $F(V,T)$, specifically $\partial^2 F/(\partial V\, \partial T) = -\beta\, B_T$. The *Supplemental Material* obtains an expression for the ratio between $\beta^{\text{QH}}$, the thermal expansion in the QHA, and the

Table 4.1: Phonon energy shifts of the LO mode with temperature.

| $T$ (K) | Energy shift: $(\varepsilon - \varepsilon_{10\,\mathrm{K}})/\varepsilon_{10\,\mathrm{K}}$ | | | | | | | | |
|---|---|---|---|---|---|---|---|---|---|
| | At $L$-point | | | Along $\Gamma$-$L$ | | | Along $\Gamma$-$X$ | | |
| | QH | Anh. | Exp. | QH | Anh. | Exp. | QH | Anh. | Exp. |
| 300 | -0.003 | -0.065 | -0.080 (0.020) | -0.037 | -0.087 | -0.062 (0.020) | -0.031 | -0.051 | -0.052 (0.020) |
| 700 | -0.025 | -0.164 | -0.174 (0.055) | -0.045 | -0.181 | -0.169 (0.055) | -0.034 | -0.144 | -0.132 (0.055) |

QH = quasiharmonic, Anh. = anharmonic, Exp. = experimental.

Errors are from the instrument energy resolution and/or the peak fitting process.

Average values were used for evaluation along the path.

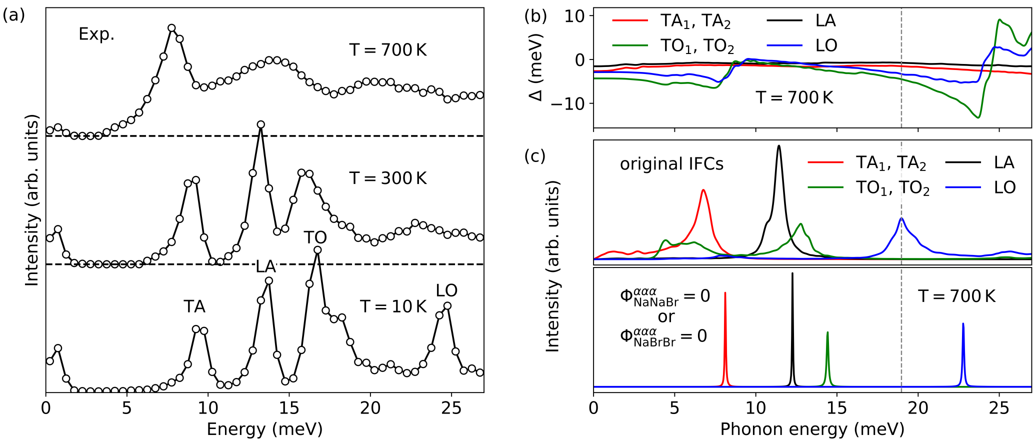

Figure 4.3: Measured and calculated phonon lineshapes at the $L$-point and the real part of the phonon self-energy. (a) The 1D cut of $S(\mathbf{Q}, \varepsilon)$ at a constant $\mathbf{Q}$ = $[0.5, 0.5, 0.5]$ r.l.u. (reciprocal lattice units), showing the temperature dependence of phonon lineshapes. (The small peak near zero is the residue from elastic scattering after correcting for the phonon creation thermal factor.) (b) Real component of the phonon self-energy $\Delta$ from the third-order force constants. (c) Phonon intensities after nulling the third-order force constants, $\Phi^{\alpha\alpha\alpha}_{\mathrm{NaNaBr}}$ or $\Phi^{\alpha\alpha\alpha}_{\mathrm{NaBrBr}}$, associated with the nearest-neighbor degenerate triplets, where $\alpha = (x, y, z)$ represents the direction along the Na-Br bond.

real $\beta$. For $\hbar\omega_{\max} < k_{\mathrm{B}}T$,

$$\beta^{\mathrm{QH}} \Big/ \beta = 1 - \frac{6k_{\mathrm{B}}}{\beta\, B_T\, v}\, \overline{\gamma}_{V,T} \ , \tag{4.4}$$

where $B_T$ is the isothermal bulk modulus, $v$ is the volume per atom, the mode anharmonicity parameter is

$$\gamma_{V,T} \triangleq -\frac{VT}{\omega} \left( \frac{\partial^2 \omega}{\partial T \partial V} \right) \ , \tag{4.5}$$

and $\overline{\gamma}_{V,T}$ is the average anharmonicity parameter. For NaBr, $\beta^{\mathrm{QH}} \simeq 0.28\beta$, which is consistent with Fig. 4.2 above.

By testing different first-principles calculations against phonons measured by inelastic neutron scattering at different temperatures, we demonstrated that the widely-accepted quasiharmonic method predicts only a small fraction of the thermal phonon shifts and the thermal expansion. Anharmonic effects drastically alter the phonon self energies, especially the LO phonons. The dominant anharmonicity is from cubic interactions associated with the nearest-neighbor degenerate triplets along the Na-Br boding direction. The volume dependence of the phonon anharmonicity dominates the thermal expansion of NaBr. Other alkali halides with the rocksalt structure, especially NaCl, NaI, and NaF, have similar thermal expansion as NaBr, and similar Grüneisen parameters of 3.3 when calculated as $\gamma = \beta B v / C_\mathrm{p}$. Similar anharmonic effects seem likely in these compounds.

## 4.2 Supplementary Material

### Comparing the thermal expansion in quasiharmonic and anharmonic theories

### Classical Thermodynamics

The (volumetric) thermal expansion coefficient, $\beta$, is defined as

$$\beta = \frac{1}{V}\frac{\mathrm{d}V}{\mathrm{d}T} \tag{4.6}$$

at $P = 0$, or at a constant pressure. This Section 4.2 obtains $\beta$ from the thermodynamic free energy $F(V,T)$, which includes the variables of Eq. 4.6. A good starting point is classical thermodynamics, which provides relationships involving partial derivatives of $F$ with respect to $V$ and $T$. Thermal expansion requires both types of partial derivatives to second order. Expansion is a change in volume, of course, but thermal expansion occurs with a change of temperature.

We start with a thermodynamic identity

$$\beta = -\frac{1}{B_T}\frac{\partial^2 F}{\partial T \partial V} \ , \tag{4.7}$$

where $B_T$ is the isothermal bulk modulus, defined as

$$B_T = -V\frac{\partial P}{\partial V} = V\frac{\partial^2 F}{\partial V^2} \ . \tag{4.8}$$

Thus, we have

$$\beta = -\frac{1}{V}\left(\frac{\partial^2 F}{\partial T \partial V}\right) \Big/ \left(\frac{\partial^2 F}{\partial V^2}\right) \ . \tag{4.9}$$

One strategy to calculate thermal expansion is to solve for $f(T,V) \triangleq \dfrac{\partial F}{\partial V} = 0$ for $V = V(T)$ in quasiharmonic or anharmonic models, and then obtain the thermal expansion coefficient from Eq. 4.6. This is done for the quasiharmonic approximation in Sect. 4.2 with Fig. 4.8. Here we employ an alternative strategy of calculating Eq. 4.9 directly. The two approaches are equivalent because

$$\frac{\mathrm{d}V}{\mathrm{d}T} = -\left(\frac{\partial f}{\partial T}\right) \Big/ \left(\frac{\partial f}{\partial V}\right) = -\left(\frac{\partial^2 F}{\partial T \partial V}\right) \Big/ \left(\frac{\partial^2 F}{\partial V^2}\right) \ . \tag{4.10}$$

**Phonon Statistical Mechanics**

We address the underlying physics by calculating the phonon free energy, ignoring possible contributions from electronic or magnetic excitations. The key quantities are the energies $\{\hbar\omega_i\}$, where $\omega_i$ is the frequency of a phonon added to the $i$th vibrational mode. In general, this frequency depends on $V$ and $T$, $\omega_i(V,T)$. In the "quasiharmonic approximation" (QHA), the $\omega_i$ and the phonon free energy depend only on $V$. In the QHA, the effects of temperature are only from the occupancies of phonon modes. The QHA is convenient for calculating thermal expansion, requiring only a set of mode Grüneisen parameters.

For $\omega(T,V)$, the Taylor expansion to second order gives

$$\begin{aligned}\Delta\omega &= \omega(T+\Delta T, V+\Delta V) - \omega(T,V)\,, && (4.11)\\ &\simeq \frac{\partial\omega}{\partial T}\Delta T + \frac{\partial\omega}{\partial V}\Delta V \\ &\quad + \frac{1}{2}\left(\frac{\partial^2\omega}{\partial T^2}(\Delta T)^2 + 2\frac{\partial^2\omega}{\partial T\partial V}(\Delta T\Delta V) + \frac{\partial^2\omega}{\partial V^2}(\Delta V)^2\right)\,. && (4.12)\end{aligned}$$

The first two terms in Eq. 4.12, with linear shifts of frequency with $\Delta T$ and $\Delta V$, give the shifts from anharmonicity and quasiharmonicity. The term in $(\Delta T)^2$ is beyond the anharmonicity from cubic and quartic perturbations, which give frequency shifts linear in $\Delta T$. We expect it to be smaller than the anharmonic effects in NaBr at constant volume. Likewise, the last term in $(\Delta V)^2$ is beyond the quasiharmonic theory, since it describes how Grüneisen parameters change with $\Delta V$.

The remaining term in Eq. 4.12 with $\Delta T\Delta V$ describes how a Grüneisen parameter changes with temperature, or how the anharmonicity changes with volume. If mode Grüneisen parameters change with temperature, the anharmonic 3- and 4-phonon processes will have a different dependence on volume at low and high temperatures, owing to changes in the kinematically-allowed processes that conserve energy and momentum. This is a change in anharmonicity with volume.

$$\Delta\omega \simeq \frac{\partial\omega}{\partial T}\Delta T + \frac{\partial\omega}{\partial V}\Delta V + \frac{\partial^2\omega}{\partial T\partial V}(\Delta T\Delta V)\,. \qquad (4.13)$$

The second term in Eq. 4.13, the quasiharmonic correction, is a first order term. It is expected to be larger than the third term. However, the temperature dependence is still needed for thermal expansion, so the third term proves important, and is dominant in NaBr.

It was recently proved that the QHA gives the leading term of the quantity $\partial F/\partial V$ [110], also [45]. This does not guarantee that the QHA gives the leading term of the thermal expansion coefficient, however, because a temperature derivative is still needed. (For example, consider the functional $y = y_0 + \Delta y$, where $y_0 = 100 + 0.001 \sin x$ and $\Delta y = \sin x$. Here the $x$-derivative is dominated by the small term $\Delta y$, rather than the leading term $y_0$.)

Less well known are anharmonic theories of thermal expansion developed with many-body theory [125, 126]. To our knowledge, there has been no direct comparison of thermal expansion from the QHA and anharmonic theory, so the goal of this section is an comparison of the relative importance of each.

Ignoring the entropy from free electrons or magnetic excitations, for a simple solid with $N$ atoms the Helmholtz free energy originates with the electronic energy, i.e., the internal energy of the lattice, $U_0$, plus the free energy from phonons

$$\begin{aligned} F &= U_0 + F_{\mathrm{ph}} \ , \\ F &= U_0 + \left\langle \sum_{\mathbf{k},j} \left[ \frac{1}{2}\hbar\omega_{\mathbf{k},j} + k_{\mathrm{B}}T \ln\left(1 - e^{-\frac{\hbar\omega_{\mathbf{k},j}}{k_{\mathrm{B}}T}}\right)\right]\right\rangle_{\mathrm{BZ}} \ . \end{aligned} \tag{4.14}$$

where $\hbar\omega_{\mathbf{k},j}$ is the phonon energy at the $\mathbf{k}$-point for the $j$th phonon branch. The sum is taken over all phonon branches and $\mathbf{k}$-points in reciprocal space, and $\langle ... \rangle_{\mathrm{BZ}}$ is the average over the first Brillouin zone. For clarity in what follows, the subscripts of $\omega$ are suppressed.

Because the free energy depends on $V$ and $T$, we expect $U_0 = U_0(V, T)$ and $\omega = \omega(V, T)$. Derivatives of these quantities are needed for Eq. 4.9. The volume derivative is essential for expansion

$$\begin{aligned} \frac{\partial F}{\partial V} &= \frac{\partial U_0}{\partial V} + \left\langle \sum \frac{\hbar}{2}\frac{\partial \omega}{\partial V} + \frac{k_{\mathrm{B}}T}{1 - e^{-\frac{\hbar\omega}{k_{\mathrm{B}}T}}} \left(-e^{-\frac{\hbar\omega}{k_{\mathrm{B}}T}}\right)\left(-\frac{\hbar}{k_{\mathrm{B}}T}\right)\frac{\partial \omega}{\partial V}\right\rangle_{\mathrm{BZ}} \\ &= \frac{\partial U_0}{\partial V} + \frac{\hbar}{2}\left\langle \sum \frac{\partial \omega}{\partial V} \coth\left(\frac{\hbar\omega}{2k_{\mathrm{B}}T}\right)\right\rangle_{\mathrm{BZ}} \ . \end{aligned} \tag{4.15}$$

From Eq. 4.15, we can calculate the additional derivatives needed in Eq. 4.9

$$\begin{aligned} \frac{\partial^2 F}{\partial T \partial V} =& \frac{\partial^2 U_0}{\partial T \partial V} + \frac{\hbar}{2}\Bigg\langle \sum \Bigg[ \frac{\partial^2 \omega}{\partial T \partial V} \coth\left(\frac{\hbar\omega}{2k_{\mathrm{B}}T}\right) \\ & - \frac{\partial \omega}{\partial V} \operatorname{csch}^2\left(\frac{\hbar\omega}{2k_{\mathrm{B}}T}\right)\left(\frac{\hbar}{2k_{\mathrm{B}}T}\frac{\partial \omega}{\partial T} - \frac{\hbar\omega}{2k_{\mathrm{B}}T^2}\right)\Bigg]\Bigg\rangle_{\mathrm{BZ}} \ , \end{aligned} \tag{4.16}$$

and

$$\frac{\partial^2 F}{\partial V^2} = \frac{\partial^2 U_0}{\partial V^2} + \frac{\hbar}{2}\left\langle \sum \left[ \frac{\partial^2 \omega}{\partial V^2} \coth\left(\frac{\hbar\omega}{2k_\mathrm{B}T}\right) - \frac{\partial \omega}{\partial V} \operatorname{csch}^2\left(\frac{\hbar\omega}{2k_\mathrm{B}T}\right)\left(\frac{\hbar}{2k_\mathrm{B}T}\frac{\partial\omega}{\partial V}\right)\right]\right\rangle_\mathrm{BZ} . \tag{4.17}$$

### Internal Energy

The first terms with $U_0$ in Eqs. 4.16 and 4.17 are familiar from the elastic energy of a solid. They are typically obtained from a Taylor expansion of the internal energy. For cubic crystals near the ground-state equilibrium volume $V_0$,

$$U_0(V,T) = U_0(V_0,T) + \frac{B_0(T)V_0}{2}\left(\frac{V-V_0}{V_0}\right)^2 + \ldots , \tag{4.18}$$

gives

$$\frac{\partial U_0}{\partial V} = B_0(T)\left(\frac{V-V_0}{V_0}\right) , \tag{4.19}$$

then

$$\frac{\partial^2 U_0}{\partial V^2} = \frac{B_0(T)}{V_0} , \tag{4.20}$$

and

$$\frac{\partial^2 U_0}{\partial T \partial V} = \frac{dB_0}{dT}\left(\frac{V-V_0}{V_0}\right) , \tag{4.21}$$

where $B_0 = -V(\partial P/\partial V)_{P=0}$ is the zeroth-order bulk modulus (i.e. $B_0 = B_T$).

### Phonon Contributions at Medium to High Temperatures

To simplify the second terms in Eqs. 4.16 and 4.17, notice that $\coth(x) = \frac{1}{x} + \frac{x}{3} - \frac{x^3}{45} + \ldots$ and $\operatorname{csch}(x) = \frac{1}{x} - \frac{x}{6} + \frac{7x^3}{360} + \ldots$, so for $\hbar\omega_\mathrm{max} < k_\mathrm{B}T$,

$$\coth\left(\frac{\hbar\omega}{2k_\mathrm{B}T}\right) \simeq \operatorname{csch}\left(\frac{\hbar\omega}{2k_\mathrm{B}T}\right) \simeq \frac{2k_\mathrm{B}T}{\hbar\omega} . \tag{4.22}$$

Using Eq. 4.22 greatly simplifies Eq. 4.16 and 4.17, with the restriction to higher temperatures where $\hbar\omega_\mathrm{max} < k_\mathrm{B}T$,

$$\frac{\partial^2 F}{\partial T \partial V} = \frac{dB_T}{dT}\left(\frac{V-V_0}{V_0}\right) + k_\mathrm{B}\left\langle \sum \left( \frac{T}{\omega}\frac{\partial^2\omega}{\partial T\partial V} - \frac{T}{\omega^2}\frac{\partial\omega}{\partial T}\frac{\partial\omega}{\partial V} + \frac{1}{\omega}\frac{\partial\omega}{\partial V}\right)\right\rangle_\mathrm{BZ} , \tag{4.23}$$

and

$$B_T = V\frac{\partial^2 F}{\partial V^2} \simeq V\left\{\frac{B_T}{V_0} + k_\mathrm{B}T\left\langle\sum\left[\frac{1}{\omega}\frac{\partial^2\omega}{\partial V^2} - \frac{1}{\omega^2}\left(\frac{\partial\omega}{\partial V}\right)^2\right]\right\rangle_\mathrm{BZ}\right\}$$

$$B_T = \frac{V}{V_0}B_T + k_\mathrm{B}TV\left\langle\sum\frac{\partial^2(\ln\omega)}{\partial V^2}\right\rangle_\mathrm{BZ} , \tag{4.24}$$

which indicates $\left|k_\mathrm{B}TV\left\langle\sum\frac{\partial^2(\ln\omega)}{\partial V^2}\right\rangle_\mathrm{BZ}\right| \ll B_T$, since $V/V_0 \simeq 1$.

### Quasiharmonic Approximation

In the quasiharmonic approximation, $U_0 = U_0(V, T = 0)$ and $\omega = \omega(V, T = 0)$, so

$$\left(\frac{\partial^2 U_0}{\partial V^2}\right)^\mathrm{QH} = \frac{B_T(T=0)}{V_0} , \quad \left(\frac{\partial^2 U_0}{\partial T\partial V}\right)^\mathrm{QH} = 0 , \quad \left(\frac{\partial\omega}{\partial T}\right)^\mathrm{QH} = 0 . \tag{4.25}$$

For $\hbar\omega_\mathrm{max} < k_\mathrm{B}T$, Eqs. 4.16 and 4.17 are simplified

$$\left(\frac{\partial^2 F}{\partial T\partial V}\right)^\mathrm{QH} = k_\mathrm{B}\left\langle\sum\frac{1}{\omega(V,T=0)}\frac{\partial\omega(V,T=0)}{\partial V}\right\rangle_\mathrm{BZ} , \tag{4.26}$$

and

$$B_T^\mathrm{QH} = V\left(\frac{\partial^2 F}{\partial V^2}\right)^\mathrm{QH} \simeq \frac{V}{V_0}B_T(T=0) + k_\mathrm{B}TV\left\langle\sum\frac{\partial^2\left[\ln\omega(V,T=0)\right]}{\partial V^2}\right\rangle_\mathrm{BZ}$$

$$\simeq B_T(T=0) \simeq B_T , \tag{4.27}$$

assuming $B_T$ is not strongly dependent on temperature, which is often true in practice.

### Comparison of Quasiharmonic and Anharmonic Results for Thermal Expansion

The results from Sections 4.2 and 4.2 allow a direct comparison of the difference in thermal expansion predicted by anharmonic and quasiharmonic theory. For moderate to high temperatures the difference between $\beta$ and $\beta^\mathrm{QH}$ is

$$\beta - \beta^\mathrm{QH} = \left(-\frac{1}{B_T}\frac{\partial^2 F}{\partial T\partial V}\right) - \left(-\frac{1}{B_T^\mathrm{QH}}\frac{\partial^2 F^\mathrm{QH}}{\partial T\partial V}\right) ,$$

$$\simeq -\frac{1}{B_T}\frac{\partial^2\left(F - F^\mathrm{QH}\right)}{\partial T\partial V} ,$$

assuming the bulk modulus does not vary strongly with temperature. Using the derivatives of $F$ from Sections 4.2 and 4.2

$$\begin{aligned}
\beta - \beta^{\mathrm{QH}} &= -\frac{1}{B_T}\frac{dB_T}{dT}\left(\frac{V-V_0}{V_0}\right) - \\
&\quad \frac{k_{\mathrm{B}}}{B_T}\left\langle \sum \left(\frac{T}{\omega}\frac{\partial^2\omega}{\partial T\partial V} - \frac{T}{\omega^2}\frac{\partial\omega}{\partial T}\frac{\partial\omega}{\partial V} \right.\right. \\
&\quad \left.\left. + \frac{1}{\omega(V,T)}\frac{\partial\omega(V,T)}{\partial V} - \frac{1}{\omega(V,T=0)}\frac{\partial\omega(V,T=0)}{\partial V}\right)\right\rangle_{\mathrm{BZ}} \\
&\simeq -\frac{1}{B_T}\frac{dB_T}{dT}\left(\frac{V-V_0}{V_0}\right) \\
&\quad - \frac{k_{\mathrm{B}}}{B_T}\left\langle \sum\left[\frac{T}{\omega}\frac{\partial^2\omega}{\partial T\partial V} - \frac{T}{\omega^2}\frac{\partial\omega}{\partial T}\frac{\partial\omega}{\partial V} + T\frac{\partial}{\partial T}\left(\frac{1}{\omega}\frac{\partial\omega}{\partial V}\right)\right]\right\rangle_{\mathrm{BZ}} \\
&= -\frac{1}{B_T}\frac{dB_T}{dT}\left(\frac{V-V_0}{V_0}\right) - \frac{2k_{\mathrm{B}}}{B_T}\left\langle\sum\left(\frac{T}{\omega}\frac{\partial^2\omega}{\partial T\partial V} - \frac{T}{\omega^2}\frac{\partial\omega}{\partial T}\frac{\partial\omega}{\partial V}\right)\right\rangle_{\mathrm{BZ}} \\
&= -\frac{1}{B_T}\frac{dB_T}{dT}\left(\frac{V-V_0}{V_0}\right) + \frac{2k_{\mathrm{B}}T}{B_T}\left\langle\sum\left(-\frac{1}{\omega}\frac{\partial^2\omega}{\partial T\partial V} + \frac{1}{\omega^2}\frac{\partial\omega}{\partial T}\frac{\partial\omega}{\partial V}\right)\right\rangle_{\mathrm{BZ}} ,
\end{aligned} \tag{4.28}$$

thus we have

$$\begin{aligned}
\beta^{\mathrm{QH}}\big/\beta &= 1 + \frac{1}{B_T\beta}\frac{dB_T}{dT}\left(\frac{V-V_0}{V_0}\right) - \frac{2k_{\mathrm{B}}T}{B_T\beta}\left\langle\sum\left(-\frac{1}{\omega}\frac{\partial^2\omega}{\partial T\partial V} + \frac{1}{\omega^2}\frac{\partial\omega}{\partial T}\frac{\partial\omega}{\partial V}\right)\right\rangle_{\mathrm{BZ}} \\
&\simeq 1 - \frac{2k_{\mathrm{B}}T}{B_T\beta}\left\langle\sum\left(-\frac{1}{\omega}\frac{\partial^2\omega}{\partial T\partial V} + \frac{1}{\omega^2}\frac{\partial\omega}{\partial T}\frac{\partial\omega}{\partial V}\right)\right\rangle_{\mathrm{BZ}} ,
\end{aligned} \tag{4.29}$$

since $\frac{1}{B_T\beta}\frac{dB_T}{dT}\left(\frac{V-V_0}{V_0}\right) < \frac{1}{B_T\beta}\frac{dB_T}{dT}\beta T = \left(\frac{dB_T}{dT}T\right)\big/B_T \sim 0.1 \ll 1$ (e.g. in MgO [127]).

### Simplifying Parameters

Introducing the mode Grüneisen parameter,

$$\gamma_V \triangleq -\frac{V}{\omega}\left(\frac{\partial\omega}{\partial V}\right)\bigg|_T , \tag{4.30}$$

the thermal Grüneisen parameter (unitless),

$$\gamma_T \triangleq -\frac{T}{\omega}\left(\frac{\partial\omega}{\partial T}\right)\bigg|_V , \tag{4.31}$$

and the anharmonicity parameter (unitless),

$$\gamma_{V,T} \triangleq -\frac{VT}{\omega}\left(\frac{\partial^2\omega}{\partial T\partial V}\right) , \tag{4.32}$$

Eq. 4.29 can be rewritten as

$$\beta^{\mathrm{QH}} \Big/ \beta = 1 - \frac{2k_{\mathrm{B}}}{B_T \beta V} \left\langle \sum \left( \gamma_{V,T} + \gamma_T \gamma_V \right) \right\rangle_{\mathrm{BZ}} . \tag{4.33}$$

To first order, the infinitesimal change of phonon energy can be divided into changes induced by temperature and volume

$$\Delta\omega \simeq \frac{\partial \omega}{\partial T} \Delta T + \frac{\partial \omega}{\partial V} \Delta V \triangleq \Delta\omega^{\mathrm{T}} + \Delta\omega^{\mathrm{V}} , \tag{4.34}$$

we find (for later use in Eq. 4.29)

$$\begin{aligned} -\frac{1}{\omega} \frac{\partial^2 \omega}{\partial T \partial V} + \frac{1}{\omega^2} \frac{\partial \omega}{\partial T} \frac{\partial \omega}{\partial V} &\simeq -\frac{1}{\omega} \frac{\Delta\omega^{\mathrm{T}} + \Delta\omega^{\mathrm{V}}}{\Delta T \Delta V} + \frac{1}{\omega^2} \frac{\Delta\omega^{\mathrm{T}}}{\Delta T} \frac{\Delta\omega^{\mathrm{V}}}{\Delta V} \\ &= \frac{1}{\Delta T \Delta V} \left[ \left( -\frac{\Delta\omega^{\mathrm{T}}}{\omega} \right) + \left( -\frac{\Delta\omega^{\mathrm{V}}}{\omega} \right) + \left( -\frac{\Delta\omega^{\mathrm{T}}}{\omega} \right) \left( -\frac{\Delta\omega^{\mathrm{V}}}{\omega} \right) \right] . \end{aligned} \tag{4.35}$$

For small positive values of $\left( -\frac{\Delta\omega^{\mathrm{T}}}{\omega} \right)$ and $\left( -\frac{\Delta\omega^{\mathrm{V}}}{\omega} \right)$,

$$\left( -\frac{\Delta\omega^{\mathrm{T}}}{\omega} \right) + \left( -\frac{\Delta\omega^{\mathrm{V}}}{\omega} \right) \gg \left( -\frac{\Delta\omega^{\mathrm{T}}}{\omega} \right) \left( -\frac{\Delta\omega^{\mathrm{V}}}{\omega} \right) , \tag{4.36}$$

which gives

$$\beta^{\mathrm{QH}} \Big/ \beta \simeq 1 - \frac{2k_{\mathrm{B}}}{B_T \beta V} \left\langle \sum \gamma_{V,T} \right\rangle_{\mathrm{BZ}} = 1 - \frac{2k_{\mathrm{B}}}{B_T \beta V} (3N) \overline{\gamma}_{V,T} = 1 - \frac{6k_{\mathrm{B}}}{B_T \beta v} \overline{\gamma}_{V,T} , \tag{4.37}$$

where $v = V/N$ is the volume per atom, and $\overline{\gamma}_{V,T} = \frac{1}{3N} \left\langle \sum_{\mathbf{k}} \sum_{j=1}^{3N} \gamma_{V,T}^{(j)} \right\rangle_{\mathrm{BZ}}$ is the average anharmonicity parameter.

An interesting and compact result from Eq. 4.37 is

$$\beta \simeq \beta^{\mathrm{QH}} + \frac{6k_{\mathrm{B}}}{B_T v} \overline{\gamma}_{V,T} . \tag{4.38}$$

This shows that the thermal expansion differs from that of the QHA owing to the mixed second derivative of the phonon energy of Eq. 4.32. In general, thermal expansion requires the consideration of both the volume and temperature dependence of the free energy.

### Why is the QHA Unreliable for Thermal Expansion?

Eq. 4.38 shows why the quasiharmonic model predicts a small thermal expansion coefficient when phonon frequencies have a temperature dependence that varies with volume. Only in the limit of no temperature dependence, which means $\overline{\gamma}_{V,T} = 0$, Eq. 4.38 reduces to $\beta^{\mathrm{QH}} = \beta$. Here we estimate some magnitudes of these effects.

The change of internal energy is estimated as

$$\Delta U_0 = \frac{1}{2} B_0 V_0 \left( \frac{\Delta V}{V_0} \right)^2 \simeq B_0 V \cdot (0.01)^2 \simeq 10^{0 \sim 1} \mathrm{meV} \; , \tag{4.39}$$

which gives

$$B_T V = B_0 V \simeq 10^{4 \sim 5}\, \mathrm{meV} = 10^{1 \sim 2}\, \mathrm{eV} \; . \tag{4.40}$$

Thus,

$$\frac{6 k_{\mathrm{B}}}{B_T \beta V} \simeq \frac{6 \times 8.617 \times 10^{-5}\, \mathrm{eV} \cdot \mathrm{K}^{-1}}{10^{-5 \sim -4}\, \mathrm{K}^{-1} \cdot 10^{1 \sim 2}\, \mathrm{eV}} \sim \mathcal{O}\left(10^{-2 \sim 0}\right) \; [\text{unitless}] \; , \tag{4.41}$$

and in some solids, some modes are possible with $0 < \overline{\gamma}_{V,T} \sim \mathcal{O}(1)$.

Finally, we have

$$\beta^{\mathrm{QH}} \Big/ \beta \sim 1 - \mathcal{O}\left(10^{-2 \sim 0}\right) \cdot \mathcal{O}(1) \; . \tag{4.42}$$

Under some circumstances, the thermal expansion coefficient can be several times larger than the quasiharmonic prediction, which means the QHA fails to get the first-order term for thermal expansion. If the QHA accounts for the leading term of thermal expansion, it is either because 1) the solid is not so anharmonic ($\overline{\gamma}_{V,T}$ is small), or 2) there is a cancellation of positive and negative $\overline{\gamma}_{V,T}$ for different phonon modes despite the anharmonicity.

### Estimate of Thermal Expansion of NaBr

We expect these $\gamma_{V,T}$ to differ for the different phonon modes, but usually all these parameters $\gamma_{V,T}$ are not available for all phonon modes. For NaBr, the energies of acoustic phonons have small changes with temperature compared to the energies of optical phonons. We therefore estimate how the thermal expansion of NaBr deviates from the prediction of the QHA by considering only the optical phonons.

At $T = 700\,\mathrm{K}$, the fractional energy shifts of the LO phonons are estimated by averaging the shifts along the $\Gamma$-$L$ and $\Gamma$-$X$ lines as listed in Table I in the manuscript

$$\left\langle - \frac{\Delta \omega^{(\mathrm{LO})}}{\omega} \right\rangle_{\mathrm{BZ}} \simeq -\frac{1}{2} [(-0.169) + (-0.132)] = 0.15 \; . \tag{4.43}$$

and the anharmonicity parameter by

$$\gamma_{V,T} = -\frac{VT}{\omega}\left(\frac{\partial^2\omega}{\partial T \partial V}\right) \simeq -\frac{VT}{\omega}\frac{\Delta\omega}{\Delta T \Delta V} = -\frac{\Delta\omega}{\omega}\frac{T}{\Delta T}\frac{V}{\Delta V} \simeq -\frac{\Delta\omega}{\omega}\frac{V}{\Delta V} \; . \tag{4.44}$$

With $\frac{a(T = 700\,\mathrm{K})}{a(T = 10\,\mathrm{K})} = 1.03$, we have $\frac{V}{\Delta V} = \frac{1.03^3}{1.03^3 - 1} \simeq 11.78$ and thus $\overline{\gamma}^{(\mathrm{LO})}_{V,T} = 1.767$. Similarly, we obtain $\left\langle -\frac{\Delta\omega^{(\mathrm{TO}_{1,2})}}{\omega} \right\rangle_{\mathrm{BZ}} \simeq 0.14$ and $\overline{\gamma}^{(\mathrm{TO}_{1,2})}_{V,T} = 1.649$ for the two TO modes. The average anharmonicity parameter of NaBr is approximately

$$\overline{\gamma}_{V,T} = \frac{1}{6}\sum_{i=1}^{6}\overline{\gamma}^{(i)}_{V,T} \simeq \frac{1}{6}\left(\overline{\gamma}^{(\mathrm{LO})}_{V,T} + 2\overline{\gamma}^{(\mathrm{TO})}_{V,T}\right) = 0.844 \; . \tag{4.45}$$

We take the value of $\beta = 3\alpha = 3 \times 60.63 \times 10^{-6}\,\mathrm{K}^{-1} = 182 \times 10^{-6}\,\mathrm{K}^{-1}$ [17], $B_T = 18.5\,\mathrm{GPa}$ [128] and $a = 6.1376\,\text{Å}$ (700 K) [17], which gives the volume per atom as $v = a^3/8 = 2.89 \times 10^{-29}\,\mathrm{m}^3$. So finally,

$$\beta^{\mathrm{QH}} \Big/ \beta = 1 - \frac{6k_{\mathrm{B}}}{B_T \beta v}\overline{\gamma}_{V,T} \simeq 0.28 \; , \tag{4.46}$$

which is rather good agreement with the deficiency of the QHA shown in Fig. 4.9.

### Inelastic neutron scattering experiments

### Details about the experiment

The INS measurements used a high-purity single crystal of NaBr. Crystal quality was checked by X-ray and neutron diffraction. The INS data were acquired with the time-of-flight Wide Angular-Range Chopper Spectrometer, ARCS, at the Spallation Neutron Source at the Oak Ridge National Laboratory. The neutrons had an incident energy of 30 meV. The single crystal of [001] orientation was suspended in an aluminum holder, which was mounted in a closed-cycle helium refrigerator for the 10 K measurement, and a low-background electrical resistance vacuum furnace for measurements at 300 and 700 K. For each measurement, time-of-flight neutron data was collected from 201 rotations of the crystal in increments of 0.5° about the vertical axis.

Data reduction gave the 4D scattering function $S(\mathbf{Q}, \varepsilon)$, where $\mathbf{Q}$ is the 3D wave-vector and $\varepsilon$ is the phonon energy (from the neutron energy loss). Measurements with an empty can were performed to evaluate the background. To correct for nonlinearities of the ARCS instrument, offsets of the $q$-grid were corrected to first order by fitting a set of 45 *in situ* Bragg diffractions, which were transformed to their theoretical positions in the reciprocal space of the NaBr structure. The linear transformation matrix had only a small deviation (less than 0.02) from the identity matrix, showing that the original data had good quality and the linear correction for $q$-offsets was adequate. After subtracting the empty-can background and removing multiphonon scattering calculated with the incoherent approximation (discussed below), the intensities from the higher Brillouin zones were folded back into an irreducible wedge in the first Brillouin zone to obtain the spectral intensities shown in Fig. 2 in the main text.

The multiphonon scattering in the incoherent approximation [129] is given by

$$S_{n>1}(\mathbf{Q},\varepsilon) = \sum_{n=2}^{\infty}\sum_{d} e^{-2W_d}\frac{(2W_d)^n}{n!}\frac{\sigma_{\text{total},d}}{M_d}A_{n,d}(\varepsilon)\ , \tag{4.47}$$

where $\mathbf{Q}$ is the reciprocal space vector, $\varepsilon$ is the phonon energy, and for atom $d \in (\text{Na}, \text{Br})$, $\sigma_{\text{total},d}$ is the total neutron scattering cross section, $M_d$ is atomic mass, and

$$2W_d = 2W_d(|\mathbf{Q}|) = \frac{\hbar^2|\mathbf{Q}|^2}{2M_d}\int_0^{\infty} d\varepsilon\ \frac{g_d(\varepsilon)}{\varepsilon}\coth\left(\frac{\varepsilon}{2k_BT}\right) \tag{4.48}$$

is the Debye-Waller factor. The $n^{\text{th}}$-order partial phonon spectra of atoms $d$ and $\bar{d}$, $A_{n,d}$ and $A_{n,\bar{d}}$, were calculated as

$$A_{1,d}(\varepsilon) = \frac{g_d(\varepsilon)}{\varepsilon}\frac{1}{e^{\varepsilon/k_BT}-1}\ , \tag{4.49}$$

$$A_{1,\bar{d}}(\varepsilon) = \frac{g_{\bar{d}}(\varepsilon)}{\varepsilon}\frac{1}{e^{\varepsilon/k_BT}-1}\ , \tag{4.50}$$

$$A_{n,d}(\varepsilon) = \frac{1}{2}\Big(A_{1,d}\circledast A_{n-1,d} + \frac{1}{n}A_{1,d}\circledast A_{n-1,\bar{d}} + \frac{n-1}{n}A_{1,\bar{d}}\circledast A_{n-1,d}\Big)\ , \tag{4.51}$$

$$A_{n,\bar{d}}(\varepsilon) = \frac{1}{2}\Big(A_{1,\bar{d}}\circledast A_{n-1,\bar{d}} + \frac{1}{n}A_{1,\bar{d}}\circledast A_{n-1,d} + \frac{n-1}{n}A_{1,d}\circledast A_{n-1,\bar{d}}\Big)\ . \tag{4.52}$$

Here, $\bar{d}$ refers to the other atom in the unit cell. The temperature-dependent partial phonon density of states (DOS), $g_d(\varepsilon)$, was obtained by our sTDEP method that used *ab initio* DFT calculations.

For NaBr, we truncated Eq. 4.47 at $n = 8$, and a global scaling factor was applied to the multiphonon scattering function for normalization. Finally, the folded-back data was corrected for the phonon creation thermal factor. This folding technique cancels out the polarization effects and improves the statistical quality by assessing phonon intensities over multiple Brillouin zones. Fig. 4.4 shows a set of enlarged, separated figures of the scattering data along the $\Gamma$-$X$ and $\Gamma$-$L$ directions.

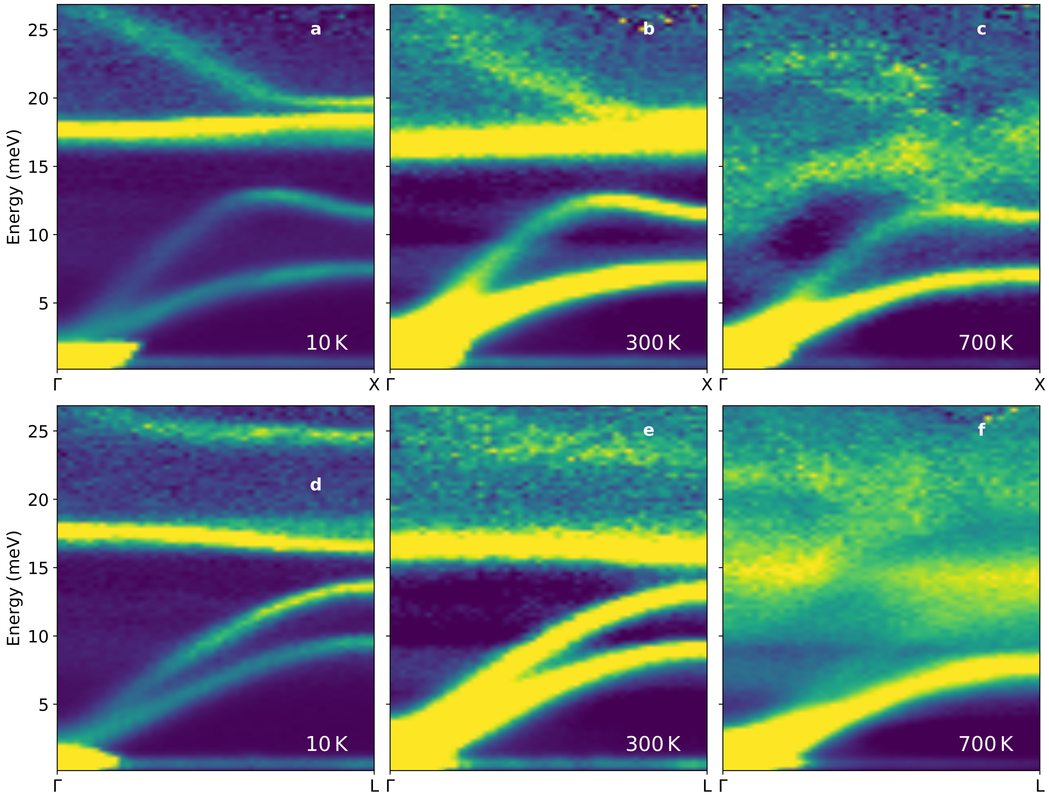

Figure 4.4: Experimental phonon dispersions of NaBr along Γ-$X$ and Γ-$L$. Phonon dispersions are shown by 2D slices of the $S(\mathbf{Q}, \varepsilon)$ data along the high symmetry lines of Γ-$X$ (a-c) and Γ-$L$ (d-f) at the temperature of 10 K (a, d), 300 K (b, e) and 700 K (c, f).

### Extracting the phonon DOS

Normally, the phonon DOS is measured by the INS experiments on the powder sample. However, with the folding-back technique and the multi-phonon scattering removal, we can also extract the phonon DOS from the INS experiment on the single crystal sample by doing an integration of the first Brillouin zone after folding back the inelastic neutron scattering data. The polarization effect was cancelled out as much as possible as more Brillouin zones were folded back. The discrepancy was introduced by the instrument resolution function and multi-scattering effects, but these results are good enough to show the reliability of the anharmonic phonon calculation.

The raw DOS data (e.g. at 700 K)is shown in Fig. 4.5. It was then cleaned by removing the elastic peak and corrected for the thermal effects before normalization. The final results are shown in Fig. 4.6 and 4.7 at elevated temperatures where the

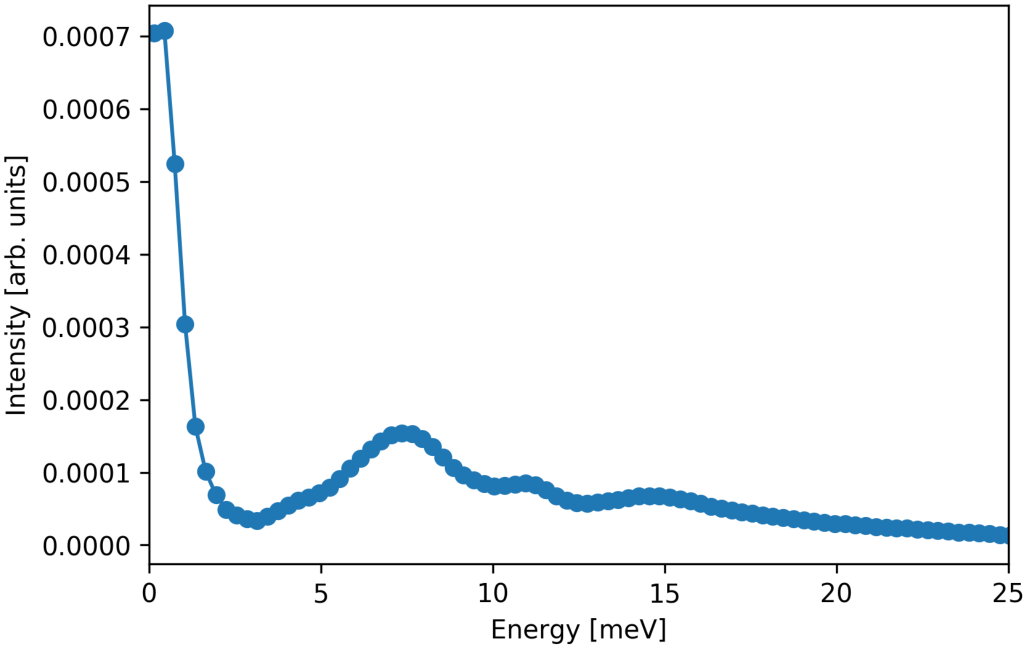

Figure 4.5: The raw dos from INS experiment on the single crystal.

anharmonicity matters.

### *ab initio* calculations

### General

All DFT calculations were performed with the VASP package using a plane-wave basis set [66–68, 122] with projector augmented wave (PAW) pseudopotentials [101] and the Perdew-Burke-Ernzerhof (PBE) exchange correlation functional [102]. All calculations used a kinetic-energy cutoff of 550 meV, a 5×5×5 supercell of 250 atoms, and a 3×3×3 $k$-point grid. Quasiharmonic calculations used PHONOPY [103]. The sTDEP [39–41] method was used to calculate anharmonic phonons at elevated temperatures. The Born effective charges and dielectric constants were obtained by DFT calculations in VASP [130]. The non-analytical term of the long-ranged electrostatics was corrected for both quasiharmonic and anharmonic calculations [131]. The phonon self-energy was calculated with a 35×35×35 $q$-grid.

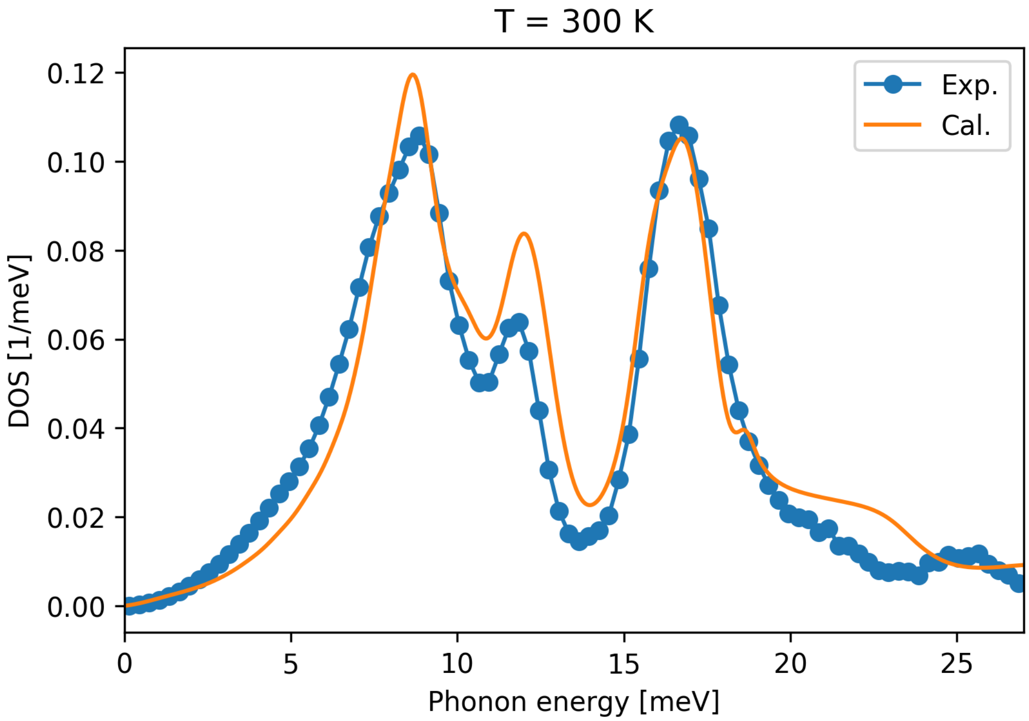

Figure 4.6: Comparison between the experimental phonon DOS extracted from the INS data and the calculated phonon DOS with anharmonicity at 300 K.

### Quasiharmonic calculations

The free energy and the equilibrium volumes calculated with the QHA are shown in Fig. 4.8. The linear thermal expansion coefficients from measurements and QHA calculations are compared in Fig. 4.9. We did not calculate detailed linear thermal expansion coefficients with the stochastically-initialized temperature dependent effective potential method (sTDEP) method, but we compared lattice constants at several temperatures to illustrate thermal expansion (see Fig. 1 in the main text).

### Anharmonic calculations: sTDEP method

We performed first-principles calculations on a temperature-volume grid covering five temperatures and five volumes. We chose the five temperatures as $T = \{10,\ 300,\ 450,\ 600,\ 700\}$ K and the five volumes linearly spaced within ±5% around the equilibrium volumes. We iterated for 3 to 5 times until the force constants were converged.

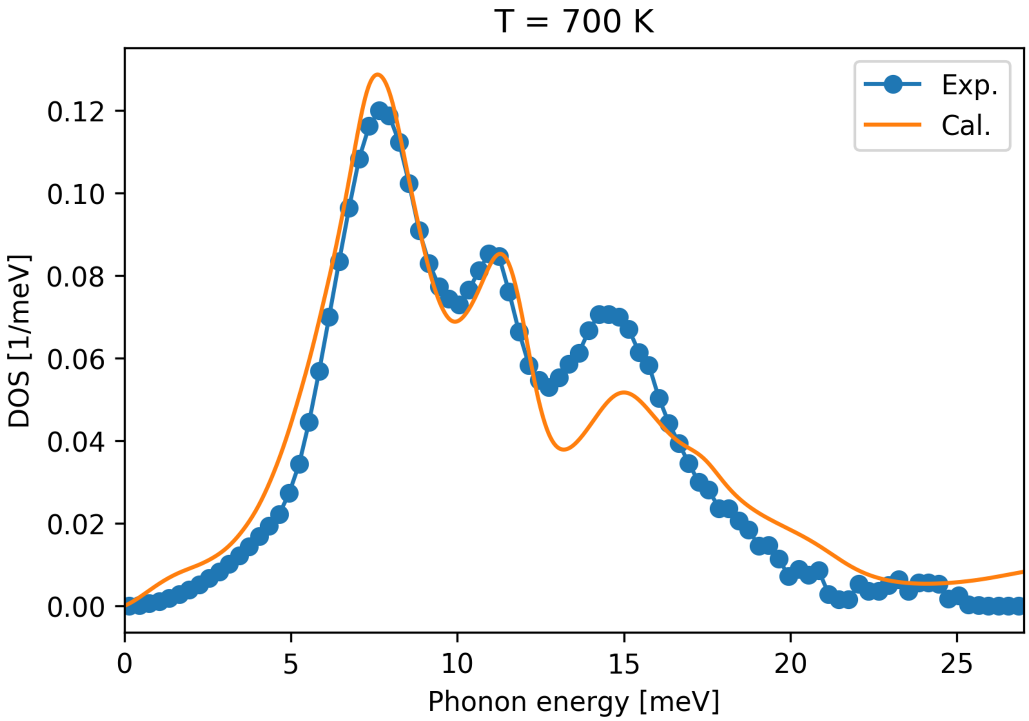

Figure 4.7: Comparison between the experimental phonon DOS extracted from the INS data and the calculated phonon DOS with anharmonicity at 700 K.

**Phonons away from high symmetry lines**

The anharmonicity and its origin with first-neighbor Na-Br bonds are not only true for phonons along the high-symmetry lines, but for the whole Brillouin zone. Figures 4.10 and 4.11 (similar to Fig. 3 in the manuscript) show lineshapes from experiment and computation at two arbitrary points in the Brillouin zone, along with the calculated real part of the phonon self-energy. The thermal softening of the LO phonon modes at 700 K is seen over the Brillouin zone. The real part of the phonon self-energy, arising from cubic anharmonicity to second order, is the main cause of these thermal shifts and broadenings.

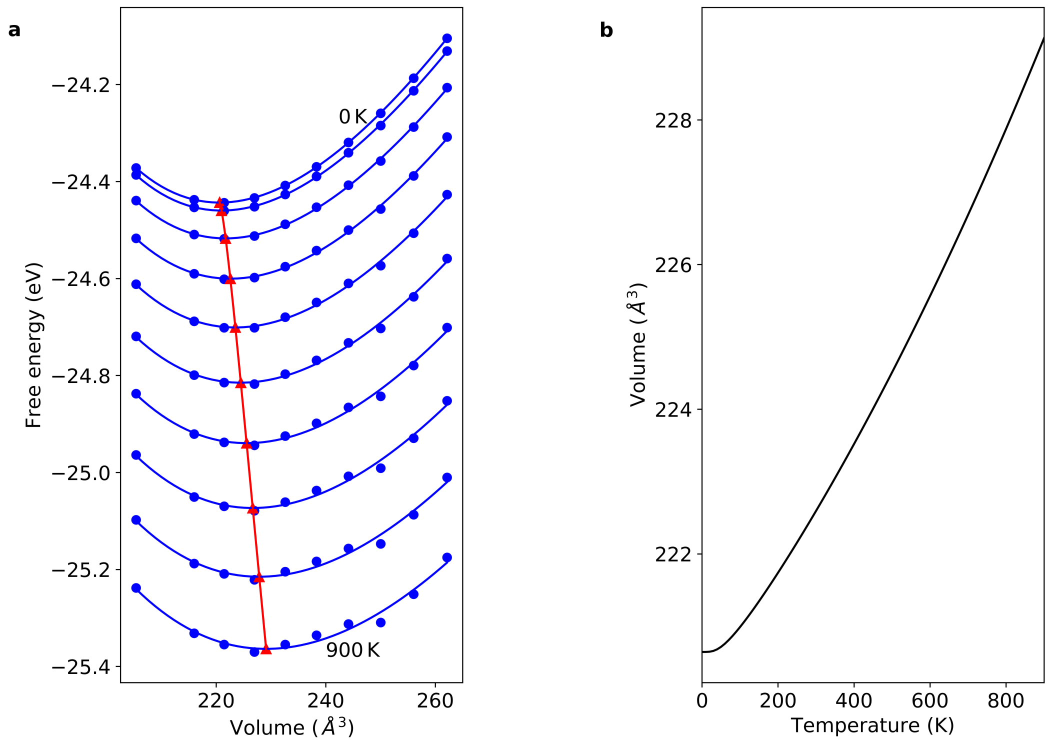

Figure 4.8: Intermediate results for expansion coefficients of NaBr calculated with the QHA. a, The Helmholtz free energy as a function of temperature and volume. The volume-energy data was fitted to a Birch-Murnaghan equation of state. b, The equilibrium volumes with temperature, obtained by minimizing the free energy at each temperature.

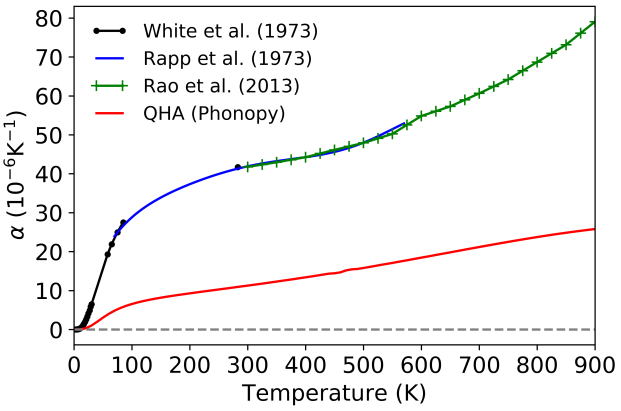

Figure 4.9: Thermal expansion coefficients of NaBr, measured and calculated by QHA. The *ab initio* quasiharmonic predictions (red solid line) are compared to the experimental results [15–17]. The linear thermal expansion coefficients, $\alpha$, are a factor of four lower than experimental results.

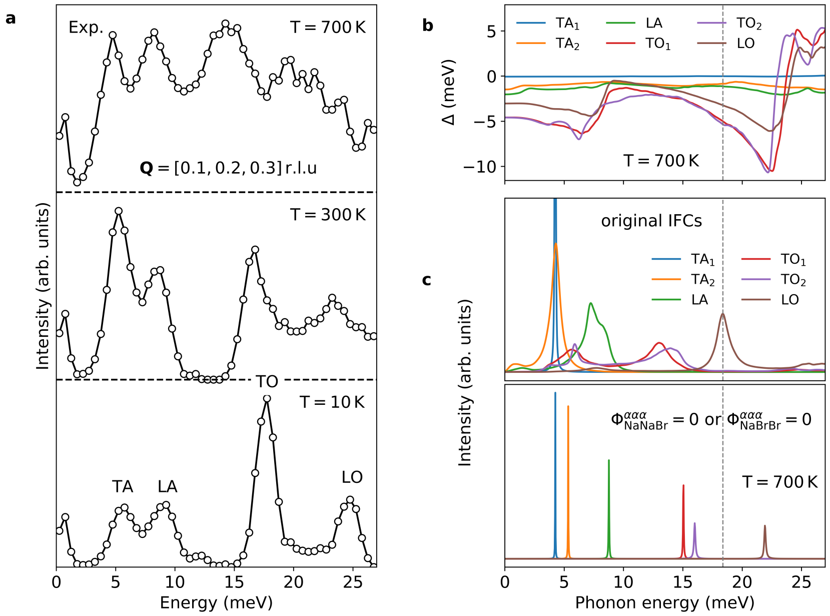

Figure 4.10: Measured and calculated phonon lineshapes at $\mathbf{Q} = [0.1, 0.2, 0.3]$ r.l.u. and the real part of the phonon self-energy. a, The 1D cut of $S(\mathbf{Q}, \varepsilon)$ at a constant $\mathbf{Q} = [0.1, 0.2, 0.3]$ r.l.u. (reciprocal lattice units), showing the temperature dependence of phonon lineshapes in NaBr. At this $Q$-point, the LO phonon peak has an energy decrease with temperature of $3 \sim 4$ meV. This can be attributed to the real component of the phonon self-energy as shown in (b). The intensity data were scaled and offset for clarity. c, By nulling the third-order force constants, $\Phi^{\alpha\alpha\alpha}_{\mathrm{NaNaBr}}$ or $\Phi^{\alpha\alpha\alpha}_{\mathrm{NaBrBr}}$, associated with the nearest-neighbor degenerate triplets, where $\alpha = (x, y, z)$ represents the direction along the Na-Br bond, the lineshapes at this $Q$-point become narrow Lorentzian peaks at 700 K and the energy decrease of the LO mode vanishes.

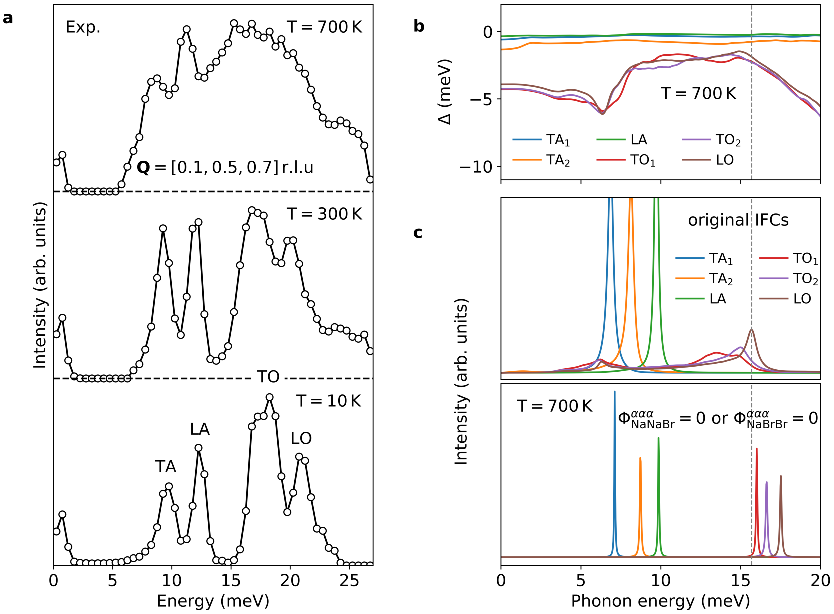

Figure 4.11: Measured and calculated phonon lineshapes at $\mathbf{Q} = [0.1, 0.5, 0.7]$ r.l.u. and the real part of the phonon self-energy. The panels are the same quantities in the previous figure, but for $\mathbf{Q} = [0.1, 0.5, 0.7]$ r.l.u. It is seen again that the LO phonon mode shifts to a lower energy at 700 K, mainly due to the cubic interactions.

## *Chapter 5*

# COHERENT SIDEBAND QUASIPARTICLES CREATED FROM ANHARMONIC PHONONS IN SODIUM BROMIDE

### 5.1 Main Text

Phonons, energy quanta in vibrational modes, are essential to condensed matter physics [132, 133]. Harmonic models give the essence of phonon dispersions of frequency versus wavevector, $\omega(\vec{k})$, and the harmonic equations of motion are formulated as eigenvalue problems. In three dimensions these give $3\mathcal{R}$ dispersions, where $\mathcal{R}$ is the number of atoms in the unit cell. The harmonic model is readily extended to a “quasiharmonic model” to account for how the dispersions shift with volume. Anharmonic models based on many-body perturbation theory [46, 58, 113] are needed to account for how the dispersions shift with temperature alone, and how finite phonon lifetimes originate with phonon-phonon interactions. Perturbation theory couples the phonon modes, but the $3\mathcal{R}$ dispersions are retained. To date these $3\mathcal{R}$ dispersions are consistent with experimental work, with an exception being the observation of intrinsic localized modes (ILM) [35, 36], but there are different views of their origin and significance [34, 134–138].

In the rapidly-advancing field of laser-cavity physics, a quantized mechanical motion is coupled to photons in a cavity. A tuned laser drives the eigenmodes, cooling or heating the mechanical motion [139–146]. Both photons and phonons are bosons, and photon-phonon coupling in laser-cavity research has similarities to anharmonic phonon-phonon coupling. Can laser-cavity phenomena, such as asymmetric sidebands, occur in the phonon spectra of anharmonic crystals? Here the advances in sensitivity of inelastic neutron scattering and single-crystal techniques with chopper spectrometers were used to find new spectral features in NaBr at moderate temperatures. We interpret both these new features and ILMs as intermodulation sidebands.

Phonons in NaBr were measured by inelastic neutron scattering (INS) experiments with the time-of-flight Wide Angular-Range Chopper Spectrometer, ARCS [43], at the Spallation Neutron Source at Oak Ridge National Laboratory. A new spectral feature appears at 300 K, labeled “G" in Fig. 5.1b. It is flat over the Brillouin zone with an energy of 25-26 meV. This new feature does not belong to any of

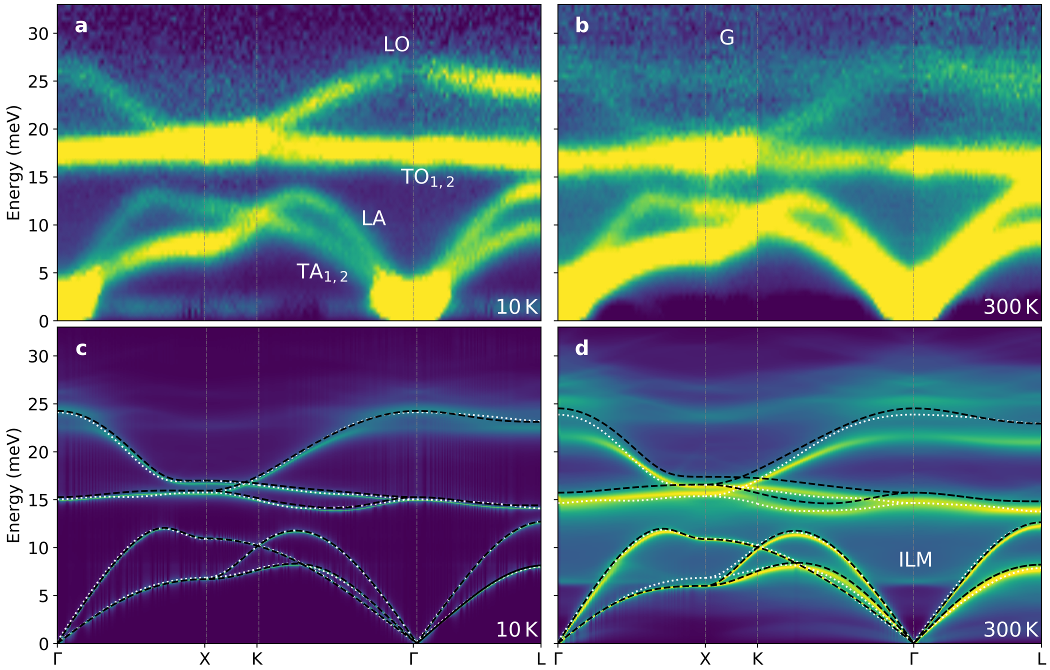

Figure 5.1: Comparison between experimental and computational phonon dispersions of NaBr. a-b, 2D slices through the four-dimensional scattering function $S(\mathbf{Q}, \varepsilon)$, where $\varepsilon = \hbar\omega$, along high symmetry lines in the first Brillouin zone. c-d, Phonons in NaBr calculated with the quasiharmonic approximation (white dotted line), with only the quadratic force constants s-TDEP (black dashed line), and the full phonon spectral function with phonon self-energy corrections. Temperatures are labeled. The IPS "G" is seen in the experimental and computational results around the X point at 300 K. The calculation also shows an ILM near the Γ-point at 300 K.

the six phonon branches predicted by a quasiharmonic model (see Methods and Supplemental).

*Ab inito* calculations accounted for the third-order anharmonic term, $\mathcal{H}_3$, of many-body theory [46, 113],

$$\mathcal{H}_3 = \frac{1}{3!} \sum_{\mathbf{q}\mathbf{q}'\mathbf{q}''} \sum_{jj'j''} \frac{(\hbar/2)^{\frac{3}{2}}}{N^{1/2}} \frac{\Phi(\mathbf{q}j, \mathbf{q}'j', \mathbf{q}''j'')}{\sqrt{\omega_{\mathbf{q}j}\omega_{\mathbf{q}'j'}\omega_{\mathbf{q}''j''}}} \delta_{\mathbf{q}+\mathbf{q}'+\mathbf{q}'',\mathbf{G}}$$
$$\times (\hat{a}^\dagger_{-\mathbf{q}j} + \hat{a}_{\mathbf{q}j})(\hat{a}^\dagger_{-\mathbf{q}'j'} + \hat{a}_{\mathbf{q}'j'})(\hat{a}^\dagger_{-\mathbf{q}''j''} + \hat{a}_{\mathbf{q}''j''}) \ , \quad (5.1)$$

where $\Phi(\mathbf{q}j, \mathbf{q}'j', \mathbf{q}''j'')$ is the three-phonon matrix element obtained from the cubic force constants by Fourier transformation, $\mathbf{q}$, $\mathbf{q}'$ and $\mathbf{q}''$ are the wave-vectors (with mode labels $j$, $j'$, $j''$) in the three-phonon processes, and the $\delta$-function guar-

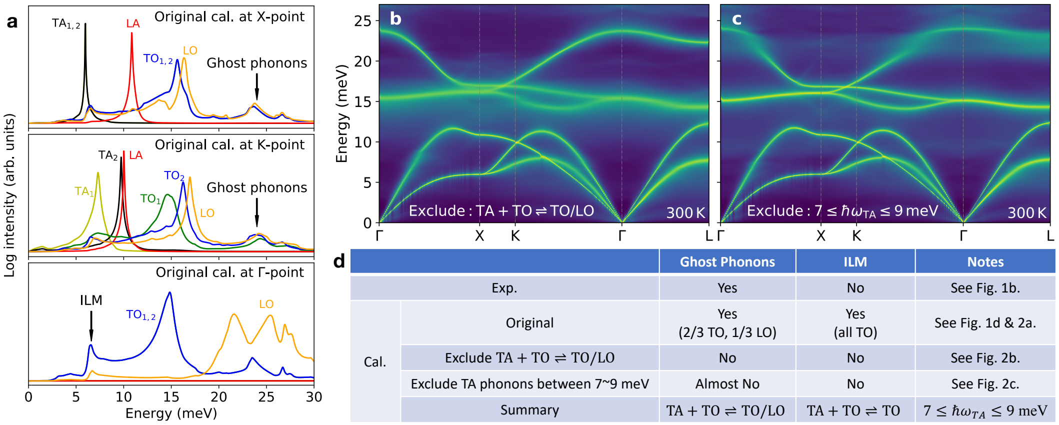

| | | Ghost Phonons | ILM | Notes |
|---|---|---|---|---|
| Exp. | | Yes | No | See Fig. 1b. |
| Cal. | Original | Yes<br>(2/3 TO, 1/3 LO) | Yes<br>(all TO) | See Fig. 1d & 2a. |
| | Exclude TA + TO ⇌ TO/LO | No | No | See Fig. 2b. |
| | Exclude TA phonons between 7~9 meV | Almost No | No | See Fig. 2c. |
| | Summary | TA + TO ⇌ TO/LO | TA + TO ⇌ TO | $7 \leq \hbar\omega_{TA} \leq 9$ meV |

Figure 5.2: Three-phonon processes associated with the IPS and ILM. a, Calculated phonon lineshapes at the high symmetry points of $X$, $K$ and Γ. The first two were used to identify the components of the IPS, and the calculated ILM is shown in the bottom panel. The phonon spectral function was recalculated b, without the three-phonon processes of TA + TO ⇌ TO/LO, and c, without TA phonons between 7-9 meV included in the three-phonon processes, compared with the original result in Fig. 5.1d. d, Table of phonon processes for IPS and the ILM.

antees momentum conservation. The temperature-dependent renormalized phonon frequencies were calculated from the dynamical matrix for the quadratic force constants, and then corrected by the real and imaginary part of the phonon self-energy from Eq. 5.1 (see Methods).

Figure 5.1a,c show that at 10 K, the harmonic, quasiharmonic, and anharmonic calculations agree well with each other, and with experimental phonon dispersions. At 300 K, the quasiharmonic model and the calculations without the phonon self-energy corrections from Eq. 5.1 predict neither the phonon broadening, nor most of the thermal energy shift. The anharmonic calculation, however, reproduces these features and further predicts a new and unexpected diffuse phonon feature around 25 meV, in good agreement with the experiments. Figure 5.2 shows that the diffuse features disappear when the calculation neglects the three phonon processes of TA + TO ⇌ TO/LO. Moreover, the participating TA phonons were shown to have energies between 7 and 9 meV. Similarly, the calculated ILM near the Γ-point (which is not definitive in Fig. 5.1b), is produced by TA + TO ⇌ TO in the calculation. The diffuse features nearly vanish at 10 K. (They should not vanish entirely, however, owing to effects of the zero-point occupancies of the TA and TO modes [106, 147].) Finally, the computations showed that the new features comprise optical modes, with polarizations distributed evenly over all transverse (two) and longitudinal (one) possibilities.

The three phonon modes for Eq. 5.1 are eigenstates of a dynamical matrix. Small anharmonic shifts and broadenings of these eigenstates do not produce new phonon branches or spectral features. Our anharmonic calculations obtained the diffuse features after applying a Kramers-Kronig transformation of Eq. 5.17 to the imaginary part of the phonon self energy of Eq. 5.16. The semiquantitative success is interesting, but these calculations of diffuse features do not elucidate the underlying physics. The calculations also predict a weak ILM [35, 148], which is more visible in the experimental data in the Supplemental.

In what follows we present an alternative physical explanation for the phonon dispersions of NaBr, inspired by interpretations of modern laser-cavity experiments [139–146]. Our model follows Eq. 5.1, with $j$, $j'$ and $j''$ designating the TA , TO and diffuse phonon features, respectively, but there is no implicit assumption that $\mathcal{H}_3$ is small. Phonons in solids are different from single mechanical oscillators because of the $\mathbf{q}$-dependence. The momentum conservation in Eq. 5.1 is usually an added complexity that is not needed for other coupled quantum systems [139–146]. Figure 5.1 shows that in NaBr, however, the TO phonon branch and the diffuse optical phonon branch are largely flat and dispersionless, as are most TA modes (the flat part of the TA dispersions occurs near Brillouin zone boundaries where there are many modes). The conservation of crystal momentum, $\mathbf{q} + \mathbf{q}' = \mathbf{q}'' + k\mathbf{G}$ ($k = 0, 1$) allows the $\mathbf{q}''$ of the diffuse modes to sweep over all the first Brillouin zone when $\mathbf{q}'$ (TO modes) covers the first Brillouin zone, even for a single value of $\mathbf{q}$. Finally, the anharmonicity is dominated by Na-Br first-neighbor interactions as shown recently [149]), and has no strong dependence on crystal orientation.

1.) Consider first the case where TA + TO $\rightleftharpoons$ G-LO and the interacting TA, TO, and LO diffuse phonon modes can be treated as individual quantum oscillators with a coupling coefficient $\eta$. The total Hamiltonian is much as expected from Eq. 5.1

$$\mathcal{H}_{\text{sys}} \simeq \mathcal{H}_0 + \hbar\eta \left(\hat{a}_j^\dagger + \hat{a}_j\right) \left(\hat{a}_{j'}^\dagger + \hat{a}_{j'}\right) \left(\hat{a}_{j''}^\dagger + \hat{a}_{j''}\right) \ , \tag{5.2}$$

where $\mathcal{H}_0 = \sum_{k=j,j',j''} \hbar\omega_k (\hat{a}_k^\dagger \hat{a}_k + \frac{1}{2})$ is the Hamiltonian for three uncoupled, independent oscillators. After dropping terms that do not conserve energy,

$$\mathcal{H}_{\text{sys}} = \mathcal{H}_0 + \hbar\eta \left(\hat{a}_j \hat{a}_{j'} \hat{a}_{j''}^\dagger + \hat{a}_j^\dagger \hat{a}_{j'}^\dagger \hat{a}_{j''}\right) \ , \tag{5.3}$$

which is the same form as for parametric down-conversion in nonlinear optics. The mode coupling is enhanced resonantly when $\omega_{j'} = \omega_{j''} - \omega_j$. Here $\eta$ is the parameter for coupling strength.

2.) The second case TA + TO $\rightleftharpoons$ G-TO has the same transverse polarization for two optical modes. Through the rest of the discussion (through Eq. 5.15), we model these two TO modes as a single oscillator. Its spectral weight is re-distributed in energy owing to strong coupling to the TA mode. (In formulating the equations of motion below, the spectral weight is also modified by the coupling to other phonons in a thermal bath.) Again starting from Eq. 5.1, the system Hamiltonian is

$$\mathcal{H}_{\text{sys}} = \mathcal{H}_0 + \hbar\frac{\eta}{2}\left(\hat{a}^\dagger + \hat{a}\right)^2\left(\hat{b}^\dagger + \hat{b}\right) , \tag{5.4}$$

where now $\hat{a}$ denotes the composite TO mode where $j' = j''$, and $\hat{b}$ denotes the TA mode, $j$, and the $1/2$ is added for later convenience. Here $\mathcal{H}_0 = \sum_{k=j,j'} \hbar\omega_k(\hat{a}_k^\dagger\hat{a}_k + \frac{1}{2})$ is the Hamiltonian for two uncoupled, independent oscillators. Confining our interest to the neutron energy loss side of the elastic line, equivalent to the rotating wave approximation (RWA) in quantum optics, we eliminate the terms $aab^\dagger$ and $a^\dagger a^\dagger b$ (and $aab$ and $a^\dagger a^\dagger b^\dagger$ that do not conserve energy)

$$\mathcal{H}_{\text{sys}} = \mathcal{H}_0 + \hbar\frac{\eta}{2}\left(\hat{a}^\dagger\hat{a} + \hat{a}\hat{a}^\dagger\right)\left(\hat{b}^\dagger + \hat{b}\right) , \tag{5.5}$$

In general we expect a term of the form $\hbar/\eta_2(a + a^\dagger)(b + b^\dagger)(b + b^\dagger)$, but we found that $\eta_2$ is small for NaBr because the number of these three-phonon processes is low. The fitting to the experimental data did not require this term.

Figure 5.3a identifies the relations between the TA and TO phonons and the thermal bath of other phonons. Using this picture, the general method of input-output theory [139, 150] gives the Heisenberg-Langevin equations of motion for the two modes,

$$\dot{\hat{a}} = -\mathrm{i}\omega_1\hat{a} - \mathrm{i}\eta\hat{a}\left(\hat{b}^\dagger + \hat{b}\right) - \frac{\gamma_1}{2}\hat{a} - \sqrt{\gamma_1}\hat{\xi}_1 , \tag{5.6}$$

$$\dot{\hat{b}} = -\mathrm{i}\omega_2\hat{b} - \mathrm{i}\frac{\eta}{2}\left(\hat{a}^\dagger\hat{a} + \hat{a}\hat{a}^\dagger\right) - \frac{\gamma_2}{2}\hat{b} - \sqrt{\gamma_2}\hat{\xi}_2 . \tag{5.7}$$

Here $\gamma_1$ and $\gamma_2$ are decay rates of the two modes, giving phonon linewidths. The other phonons are modeled as a thermal bath, described by stochastic operators $\xi_1(t)$ and $\xi_2(t)$. These satisfy the correlation conditions: $\langle\hat{\xi}_{1,2}^\dagger(t)\hat{\xi}_{1,2}(t')\rangle = n_{1,2}\delta(t - t')$ and $\langle\hat{\xi}_{1,2}(t)\hat{\xi}_{1,2}^\dagger(t')\rangle = (n_{1,2} + 1)\delta(t - t')$, where $n_{1,2}$ is the equilibrium Planck occupancy $n_{1,2} = [\exp(\hbar\omega_{1,2}/k_{\mathrm{B}}T) - 1]^{-1}$.

Using the concept of intermodulation, a classical analysis by representing the TO phonon amplitudes as Fourier decomposition of sidebands [142] shows that $\hat{a}$ comprises the frequency components $\omega_1$ (first-order), $\omega_1 \pm \omega_2$ (second-order distortion), $\omega_1 \pm 2\omega_2$ (third-order distortion), etc. Second-order effects are identified by transforming to a frame moving at the central frequency $\omega_1$ by replacing

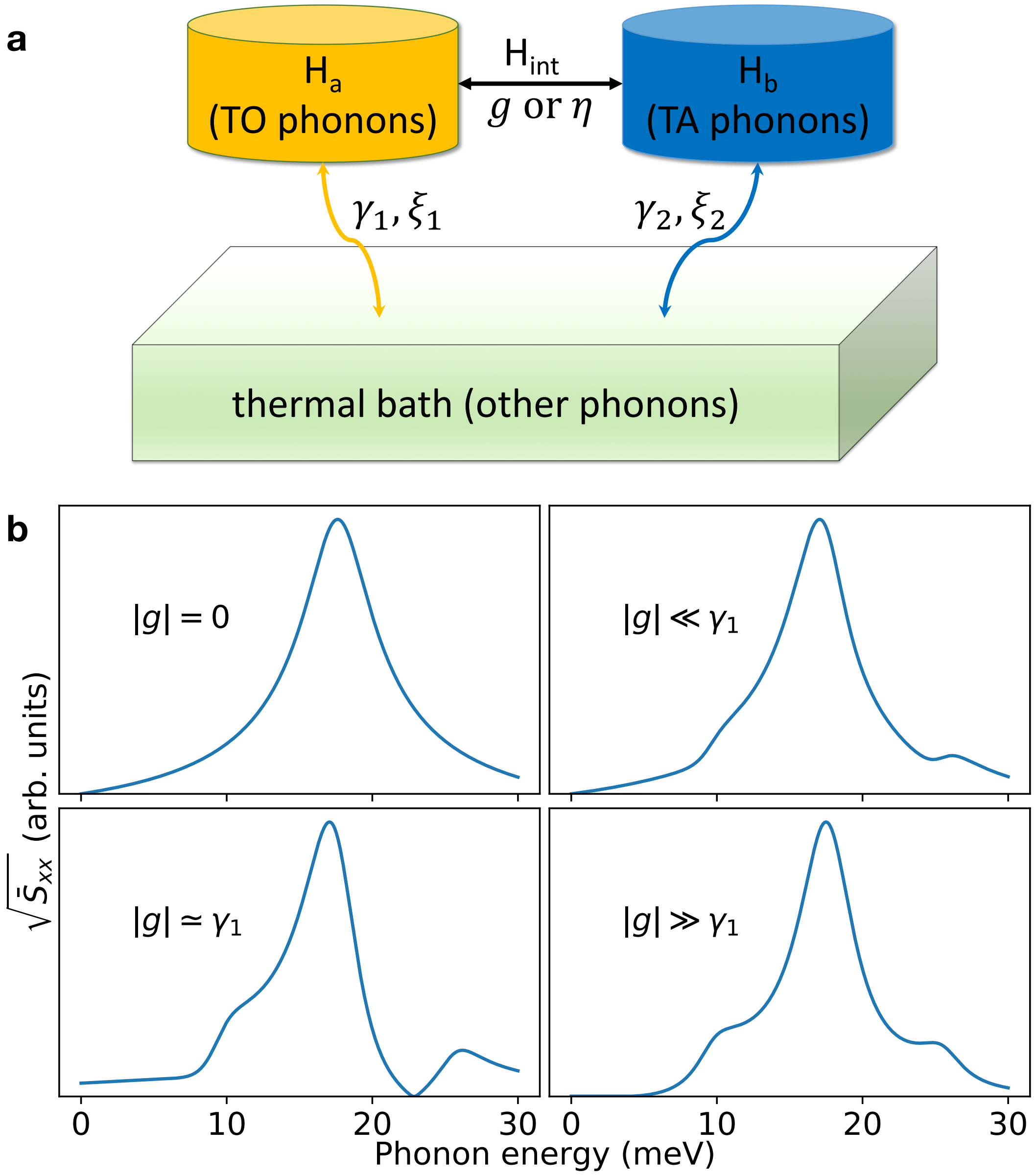

Figure 5.3: Phonon self-transduction block diagram and its features. a, The TO phonons and the TA phonons within 7-9 meV are coupled by phonon-phonon interactions. Meanwhile, they are in thermal equilibrium with the bath, which is an ensemble of other phonons. b, The power spectral density for coupling strengths in four coupling domains.

$\hat{a}(t) \longrightarrow [\alpha + \hat{c}(t)]e^{-\mathrm{i}\omega_1 t}$ and $\hat{\xi}_1(t) \longrightarrow [\xi_{\mathrm{in}} + \hat{\xi}_1(t)]e^{-\mathrm{i}\omega_1 t}$. This gives linearized equations of motion

$$\dot{\hat{c}} = -\mathrm{i}g\left(\hat{b}^\dagger + \hat{b}\right) - \frac{\gamma_1}{2}\hat{c} - \sqrt{\gamma_1}\hat{\xi}_1 \,, \tag{5.8}$$

$$\dot{\hat{b}} = -\mathrm{i}\omega_2\hat{b} - \mathrm{i}g\left(\hat{c}^\dagger + \hat{c}\right) - \frac{\gamma_2}{2}\hat{b} - \sqrt{\gamma_2}\hat{\xi}_2 \,, \tag{5.9}$$

where we take $\alpha$ to be real without loss of generality, and $g = \eta\alpha$ is the coupling strength. A straightforward calculation (see Supplemental) obtained the symmetrized power spectral density of displacement as

$$\begin{aligned}\bar{S}_{xx}[\omega] =& \frac{\hbar\gamma_1\left(n_1 + \frac{1}{2}\right)}{2m\omega_1}\left(\left|\chi_{a,-} + 2\mathrm{i}\omega_2 g^2\chi_{a,-}^2\chi_{b,-}\bar{\chi}_{b,-}\right|^2\right. \\ &\left. + \left|\chi_{a,+} - 2\mathrm{i}\omega_2 g^2\chi_{a,+}^2\chi_{b,+}\bar{\chi}_{b,+}\right|^2\right) \,,\end{aligned} \tag{5.10}$$

where the response functions are defined as

$$\chi_{a,\pm}^{-1} = -\mathrm{i}(\omega \pm \omega_1) + \frac{\gamma_1}{2} \,, \tag{5.11}$$

$$\chi_{b,\pm}^{-1} = -\mathrm{i}(\omega \pm \omega_1 - \omega_2) + \frac{\gamma_2}{2} \,, \tag{5.12}$$

$$\bar{\chi}_{b,\pm}^{-1} = -\mathrm{i}(\omega \pm \omega_1 + \omega_2) + \frac{\gamma_2}{2} \,. \tag{5.13}$$

The first term in parens in Eq. 5.10,

$$\bar{S}_{xx}^{(+)}[\omega] = \frac{\hbar\gamma_1\left(n_1 + \frac{1}{2}\right)}{2m\omega_1}\left|\chi_{a,-} + 2\mathrm{i}\omega_2 g^2\chi_{a,-}^2\chi_{b,-}\bar{\chi}_{b,-}\right|^2 \,, \tag{5.14}$$

contributes spectral weight primarily to the positive frequency region. The other term $\bar{S}_{xx}^{(-)}$ contributes to the negative.

In the absence of phonon coupling, i.e., $g = 0$, Eq. 5.14 reduces to the thermal noise spectrum of a damped harmonic oscillator

$$\bar{S}_{xx}^{(+),\mathrm{th}}[\omega] = \frac{\hbar\gamma_1\left(n_1 + \frac{1}{2}\right)}{2m\omega_1}\frac{1}{(\omega - \omega_1)^2 + (\gamma_1/2)^2} \,. \tag{5.15}$$

As shown in Fig. 5.3b, this is a Lorentzian function centered at $\omega_1$. Three other cases are shown: weak coupling ($|g| \ll \gamma_1$), medium coupling ($|g| \sim \gamma_1$), strong coupling ($|g| \gg \gamma_1$).

The Supplemental explains how experimentally measured parameters of $\omega_1 \simeq 16.97\,\mathrm{meV}$, $\omega_2 \simeq 8.2\,\mathrm{meV}$, $\gamma_1 \simeq 3.6\,\mathrm{meV}$ and $\gamma_2 \simeq 3.7\,\mathrm{meV}$ were used in a numerical analysis that generated the spectra of Fig. 5.3b. In the weak-coupling case, our measured INS spectra would probably show no features other than the main peak at $\omega = \omega_1$. In the medium-coupling case, the lower sideband Stokes peak at $\omega_1 - \omega_2$ is only a shoulder on the main peak, but the upper sideband anti-Stokes $\omega_1 + \omega_2$ should be distinguishable. The strong-coupling case shows two symmetric sidebands as shoulders on the main peak. The clear, isolated diffuse intensity in Fig. 5.1b indicates that the TA and TO modes are in the medium-coupling case. To verify this, we numerically solved (see Supplemental) the equation of the ratio between the heights of the two resonant peaks at $\omega = \omega_1$ and $\omega = \omega_1 + \omega_2$ (which avoids scaling factors), to obtain the coupling strength parameter $|g| \simeq 3.7\,\mathrm{meV}$, showing that the system is indeed in the medium-coupling domain. Unlike a classical intermodulation, phonon intermodulation can have an asymmetric quantum effect of enhancing one sideband at the expense of the other. Excitations in the ILMs and IPSs are entangled in the EPR sense. The coherency of these entangled states is not high, however, so their value for information transmission may prove less important than their role in the temperature-control of light-matter interactions.

In conclusion, we found a new diffuse phonon intensity of mixed polarization in NaBr at 300 K. The TO part of this feature is consistent with an intermodulation phonon sideband (IPS) from the anharmonic coupling of TO modes and TA modes. The LO part is consistent with strong three-phonon process, again with anharmonic coupling to the TA modes. There are similarities to the formation of sidebands in laser-cavity experiments, which also depend on anharmonicity and quantum force fluctuations from the thermal bath. Compared to laser-cavity experiments, the anharmonic processes in these neutron scattering measurements on NaBr are stronger, and are driven by relatively few thermal TA phonons. Another significant difference is that the neutron is a gentle probe of the phonon dynamics that is driven by temperature, and not by a high-power laser.

The transfer of spectral weight to upper and lower intermodulation phonon sidebands likely occurs in other anharmonic materials, but NaBr has flat phonon dispersions that make the IPS more distinct. The IPS are available for thermal control of light-matter interactions. Even without proof of principle for applications, however, it is remarkable that anharmonic phonon scattering processes, central to thermal conductivity for example, involve phonon states that are briefly entangled.

## 5.2 Methods

### INS experiments

The INS measurements used a high-purity single crystal of NaBr. Crystal quality was checked by X-ray and neutron diffraction. The INS data were acquired with the time-of-flight Wide Angular-Range Chopper Spectrometer, ARCS, at the Spallation Neutron Source at Oak Ridge National Laboratory, using neutrons with an incident energy of 50 meV. The single crystal of [001] orientation was suspended in an aluminum holder, which was mounted in a closed-cycle helium refrigerator for the 10 K measurement, and a low-background electrical resistance vacuum furnace for measurements at 300 K. For each measurement, time-of-flight neutron data were collected from 201 rotations of the crystal in increments of 0.5° about the vertical axis. Data reduction gave the 4D scattering function $S(\mathbf{Q}, \varepsilon)$, where $\mathbf{Q}$ is the 3D wave-vector and $\varepsilon$ is the phonon energy (from the neutron energy loss). Measurements with an empty can were performed to evaluate the background. To correct for nonlinearities of the ARCS instrument, offsets of the $q$-grid were corrected to first order by fitting a set of 76 *in situ* Bragg diffractions, which were transformed to their theoretical positions in the reciprocal space of the NaBr structure. The linear transformation matrix had only a small deviation (less than 0.02) from the identity matrix, showing that the original data had good quality and the linear correction for $q$-offsets was adequate. After subtracting the empty-can background and removing multiphonon scattering with the incoherent approximation, the higher Brillouin zones were folded back [106, 149] into an irreducible wedge in the first Brillouin zone to obtain the spectral intensities shown in Fig. 5.1a-b. More details are in the Supplemental.

### *Ab initio* calculations

All DFT calculations were performed with the VASP package using a plane-wave basis set [66–68, 122] with projector augmented wave (PAW) pseudopotentials [101] and the Perdew-Burke-Ernzerhof (PBE) exchange correlation functional [102]. All calculations used a kinetic-energy cutoff of 550 meV, a 5×5×5 supercell of 250 atoms, and a 3×3×3 $k$-point grid.

Quasiharmonic calculations used PHONOPY [103]. The stochastically-initialized temperature dependent effective potential method (sTDEP) [39–41] method was used to accelerate the traditional *ab initio* molecular dynamics (AIMD) and calculate anharmonic phonons at finite temperatures. Using results from many-body theory, the phonon frequencies were obtained from the dynamical matrix for the quadratic force constants, and then corrected by the real ($\Delta$) and imaginary ($i\Gamma$) parts of the phonon self-energy. The imaginary part was calculated with the third-order force constants,

$$\Gamma_\lambda(\Omega) = \frac{\hbar\pi}{16}\sum_{\lambda'\lambda''}|\Phi_{\lambda\lambda'\lambda''}|^2 \left\{(n_{\lambda'} + n_{\lambda''} + 1)\times\delta(\Omega - \omega_{\lambda'} - \omega_{\lambda''}) \right.$$
$$\left. +(n_{\lambda'} - n_{\lambda''})\times[\delta(\Omega - \omega_{\lambda'} + \omega_{\lambda''}) - \delta(\Omega + \omega_{\lambda'} - \omega_{\lambda''})]\right\}, \quad (5.16)$$

where $\Omega = E/\hbar$) is the probing energy. The real part was obtained by a Kramers-Kronig transformation

$$\Delta(\Omega) = \mathcal{P}\int \frac{1}{\pi}\frac{\Gamma(\omega)}{\omega - \Omega}\mathrm{d}\omega\ . \quad (5.17)$$

Equation 5.16 is a sum over all possible three-phonon interactions, where $\Phi_{\lambda\lambda'\lambda''}$ is the three-phonon matrix element obtained from the cubic force constants by Fourier transformation, $n$ is the Bose-Einstein thermal occupation factor giving the number of phonons in each mode, and the delta functions conserve energy and momentum. Details were given in the supplemental to our previous work [149].

The Born effective charges and dielectric constants were obtained by DFT calculations in VASP [130]. The non-analytical term of the long-ranged electrostatics was corrected for, both in quasiharmonic and anharmonic calculations [131]. The phonon self-energy was calculated with a 35×35×35 $q$-grid.

## 5.3 Supplementary Material

### Instrument Background

When measuring diffuse features in inelastic neutron scattering, properly understanding and correcting the background from the instrument and the environment around the sample is paramount. Part of the data correction requires measurements of the empty sample container under identical conditions. The empty can background, folded into the first Brillouin zone, is shown in Fig. 5.4c,d, and is compared with Fig. 1 in the manuscript. The background has two peaks centered at 20 and 35 meV, consistent with inelastic neutron scattering (INS) measurements of the phonon density of state (DOS) from polycrystalline aluminum at 300 K [18]. The new diffuse feature gives a peak at 25 meV, thus it cannot be the residue of the aluminum empty can. We also confirmed that the diffuse feature cannot be formed by the excessive subtraction of the background – this gives a much wider peak spanning the energy range between 20-35 meV. Furthermore, the temperature dependence of the background follows that of the main dispersions in NaBr, but the diffuse features are far weaker than the main dispersions at 10 K, but modestly weaker at 300 K.

### Temperature Dependence of Intermodulation Phonon Sidebands

The IPS spectra are much weaker at 10 K than at 300 K, owing to the temperature dependence of the Planck factors for phonon populations. Figure 5.5 shows how few one-phonon spectra (before renormalization) are excited at low temperature. This limits the number of the TA phonons within 7-9 meV that are available to participate the three-phonon processes to generate the intermodulation sidebands.

### Classical Analysis

Consider the original Heisenberg-Langevin equations (Eq. 6-7 in the main text):

$$\dot{\hat{a}} = -\mathrm{i}\omega_1\hat{a} - \mathrm{i}\eta\hat{a}\left(\hat{b}^\dagger + \hat{b}\right) - \frac{\gamma_1}{2}\hat{a} - \sqrt{\gamma_1}\hat{\xi}_1\ , \tag{5.18}$$

$$\dot{\hat{b}} = -\mathrm{i}\omega_2\hat{b} - \mathrm{i}\frac{\eta}{2}\left(\hat{a}^\dagger\hat{a} + \hat{a}\hat{a}^\dagger\right) - \frac{\gamma_2}{2}\hat{b} - \sqrt{\gamma_2}\hat{\xi}_2\ . \tag{5.19}$$

Following the method in Ref. [142], we can replace the phonon amplitudes with a Fourier decomposition of sidebands as

$$\hat{a} \longrightarrow \alpha = \sum_j A_j e^{-\mathrm{i}\omega_{a,j}t}, \qquad b \longrightarrow B_0 e^{-\mathrm{i}\omega_2 t}\ , \tag{5.20}$$

where $j$ is the sideband order. Substituting these into Eq. 5.18

$$\begin{aligned}\sum_j -\mathrm{i}\omega_{a,j}A_j e^{-\mathrm{i}\omega_{a,j}t} &= -\left(\mathrm{i}\omega_1 + \frac{\gamma_1}{2}\right)\sum_j A_j e^{-\mathrm{i}\omega_{a,j}t} \\ &\quad - \mathrm{i}\eta B_0 \sum_j A_j\left(e^{-\mathrm{i}(\omega_{a,j}+\omega_2)t} + e^{-\mathrm{i}(\omega_{a,j}-\omega_2)t}\right)\ .\end{aligned} \tag{5.21}$$

Comparing the two sides of Eq. 5.21, we find the intermodulation frequencies

$$\begin{aligned}\text{First order}: j &= 1,\ \omega_{a,1} = \omega_1; \\ \text{Second order}: j &= 2,\ \omega_{a,2} = \omega_1 \pm \omega_2; \\ \text{Third order}: j &= 3,\ \omega_{a,3} = \omega_{a,2} \pm \omega_2 = \omega_1 \pm 2\omega_2; \\ &\ldots\end{aligned} \tag{5.22}$$

### Solving the quantum Langevin equations

The Heisenberg-Langevin equations in the main text (Eq. 7) can be solved by Fourier transformation.For an operator in the time domain $\hat{O}(t)$, we use an operator in the frequency domain, $\hat{O}[\omega]$

$$\hat{O}[\omega] = \frac{1}{\sqrt{2\pi}} \int_{-\infty}^{+\infty} \mathrm{d}t e^{\mathrm{i}\omega t} \hat{O}(t) \ , \tag{5.23}$$

$$\hat{O}^{\dagger}[\omega] = \frac{1}{\sqrt{2\pi}} \int_{-\infty}^{+\infty} \mathrm{d}t e^{\mathrm{i}\omega t} \hat{O}^{\dagger}(t) \ . \tag{5.24}$$

This procedure gives the following Fourier transformed equations

$$(-\mathrm{i}\omega + \frac{\gamma_1}{2})\hat{c}[\omega] = -\mathrm{i}g\left(\hat{b}^{\dagger}[\omega] + \hat{b}[\omega]\right) - \sqrt{\gamma_1}\hat{\xi}_1[\omega] \ , \tag{5.25}$$

$$(-\mathrm{i}\omega + \frac{\gamma_1}{2})\hat{c}^{\dagger}[\omega] = \mathrm{i}g\left(\hat{b}^{\dagger}[\omega] + \hat{b}[\omega]\right) - \sqrt{\gamma_1}\hat{\xi}_1{}^{\dagger}[\omega] \ , \tag{5.26}$$

$$\left[-\mathrm{i}(\omega - \omega_2) + \frac{\gamma_2}{2}\right]\hat{b}[\omega] = -\mathrm{i}g\left(\hat{c}^{\dagger}[\omega] + \hat{c}[\omega]\right) - \sqrt{\gamma_2}\hat{\xi}_2[\omega] \ , \tag{5.27}$$

$$\left[-\mathrm{i}(\omega + \omega_2) + \frac{\gamma_2}{2}\right]\hat{b}^{\dagger}[\omega] = \mathrm{i}g\left(\hat{c}^{\dagger}[\omega] + \hat{c}[\omega]\right) - \sqrt{\gamma_2}\hat{\xi}_2^{\dagger}[\omega] \ . \tag{5.28}$$

Solutions for $\hat{c}$ and $\hat{c}^{\dagger}$ are

$$\begin{aligned}\hat{c}[\omega] = \chi_c^2\chi_b\bar{\chi}_b\Big\{ &- \sqrt{\gamma_1}\left[\left(\chi_c^{-1}\chi_b^{-1}\bar{\chi}_b^{-1} + 2\mathrm{i}\omega_2 g^2\right)\hat{\xi}_1 + 2\mathrm{i}\omega_2 g^2\hat{\xi}_1^{\dagger}\right] \\ &+ \mathrm{i}g\sqrt{\gamma_2}\chi_c^{-1}\left(\bar{\chi}_b^{-1}\hat{\xi}_2 + \chi_b^{-1}\hat{\xi}_2^{\dagger}\right)\Big\} \ ,\end{aligned} \tag{5.29}$$

$$\begin{aligned}\hat{c}^{\dagger}[\omega] = \chi_c^2\chi_b\bar{\chi}_b\Big\{ &- \sqrt{\gamma_1}\left[-2\mathrm{i}\omega_2 g^2\hat{\xi}_1 + \left(\chi_c^{-1}\chi_b^{-1}\bar{\chi}_b^{-1} - 2\mathrm{i}\omega_2 g^2\right)\hat{\xi}_1^{\dagger}\right] \\ &- \mathrm{i}g\sqrt{\gamma_2}\chi_c^{-1}\left(\bar{\chi}_b^{-1}\hat{\xi}_2 + \chi_b^{-1}\hat{\xi}_2^{\dagger}\right)\Big\} \ ,\end{aligned} \tag{5.30}$$

where the bare response functions are

$$\chi_c^{-1} = -\mathrm{i}\omega + \frac{\gamma_1}{2} \ , \tag{5.31}$$

$$\chi_b^{-1} = -\mathrm{i}(\omega - \omega_2) + \frac{\gamma_2}{2} \ , \tag{5.32}$$

$$\bar{\chi}_b^{-1} = -\mathrm{i}(\omega + \omega_2) + \frac{\gamma_2}{2} \ . \tag{5.33}$$

Transforming back to the original operators $\hat{a}$ ($\hat{a}^{\dagger}$), the position operator is obtained

$$\hat{x} = x_{\mathrm{zpf}}\left(\hat{a} + \hat{a}^{\dagger}\right) = x_{\mathrm{zpf}}\left[(\alpha + \hat{c})\, e^{-\mathrm{i}\omega_1 t} + \left(\alpha + \hat{c}^{\dagger}\right) e^{\mathrm{i}\omega_1 t}\right] \ , \tag{5.34}$$

with $x_{\mathrm{zpf}} = \sqrt{\frac{\hbar}{2m\omega_1}}$ as the amplitude of zero point fluctuations. Correspondingly

$$x[\omega] = x_{\mathrm{zpf}}\left(c[\omega - \omega_1] + c^{\dagger}[\omega + \omega_1] + \alpha\delta[\omega - \omega_1] + \alpha\delta[\omega + \omega_1]\right) \ . \tag{5.35}$$

Neglecting the unimportant terms of single $\delta$-functions, the displacement power spectral density, $S_{xx}[\omega]$, can be obtained by

$$\begin{aligned}
S_{xx}[\omega] &= \int_{-\infty}^{+\infty} \langle \hat{x}[\omega]\hat{x}[\omega'] \rangle \, \mathrm{d}\omega' \\
&= \frac{\hbar}{2m\omega_1} \int_{-\infty}^{+\infty} \Big\langle \Big( c[\omega-\omega_1] + c^\dagger[\omega+\omega_1] \Big) \\
&\qquad\qquad \Big( c[\omega'-\omega_1] + c^\dagger[\omega'+\omega_1] \Big) \Big\rangle \, \mathrm{d}\omega' \\
&= \frac{\hbar}{2m\omega_1} \Bigg( \int_{-\infty}^{+\infty} \langle c[\omega-\omega_1] c[\omega'-\omega_1] \rangle \, \mathrm{d}\omega' \\
&\qquad + \int_{-\infty}^{+\infty} \Big\langle c[\omega-\omega_1] c^\dagger[\omega'+\omega_1] \Big\rangle \, \mathrm{d}\omega' \\
&\qquad + \int_{-\infty}^{+\infty} \Big\langle c^\dagger[\omega+\omega_1] c[\omega'-\omega_1] \Big\rangle \, \mathrm{d}\omega' \\
&\qquad + \int_{-\infty}^{+\infty} \Big\langle c^\dagger[\omega+\omega_1] c^\dagger[\omega'+\omega_1] \Big\rangle \, \mathrm{d}\omega' \Bigg)
\end{aligned} \tag{5.36}$$

In the frequency domain, the input noise operators satisfy the relations of

$$\Big\langle \hat{\xi}_{1,2}[\omega_1] \hat{\xi}^\dagger_{1,2}[\omega_2] \Big\rangle = (n_{1,2}+1)\delta[\omega_1+\omega_2] \ , \tag{5.37}$$

$$\Big\langle \hat{\xi}^\dagger_{1,2}[\omega_1] \hat{\xi}_{1,2}[\omega_2] \Big\rangle = n_{1,2}\delta[\omega_1+\omega_2] \ . \tag{5.38}$$

Employing these relations, every term in Eq. 5.36 can be calculated

$$\begin{aligned}&\int_{-\infty}^{+\infty} \langle c[\omega-\omega_1]c[\omega'-\omega_1]\rangle \,\mathrm{d}\omega' \\ =&\,\gamma_1 \left|\chi_{a,-}^2\chi_{b,-}\bar{\chi}_{b,-}\right|^2 \left(2\mathrm{i}\omega_2 g^2\right)\times \\ &\left[\left(\chi_{a,-}^{-1}\chi_{b,-}^{-1}\bar{\chi}_{b,-}^{-1}+2\mathrm{i}\omega_2 g^2\right)(n_1+1)+\left(\chi_{a,-}^{*-1}\chi_{b,-}^{*-1}\bar{\chi}_{b,-}^{*-1}+2\mathrm{i}\omega_2 g^2\right)n_1\right] \\ &-g^2\gamma_2\left|\chi_{a,-}\chi_{b,-}\bar{\chi}_{b,-}\right|^2\left(\left|\bar{\chi}_{b,-}^{-1}\right|^2(n_2+1)+\left|\chi_{b,-}^{-1}\right|^2 n_2\right)\ ,\end{aligned}\tag{5.39}$$

$$\begin{aligned}&\int_{-\infty}^{+\infty} \left\langle c[\omega-\omega_1]c^\dagger[\omega'+\omega_1]\right\rangle \mathrm{d}\omega' \\ =&\,\gamma_1 \left|\chi_{a,-}^2\chi_{b,-}\bar{\chi}_{b,-}\right|^2 \left[\left|\chi_{a,-}^{-1}\chi_{b,-}^{-1}\bar{\chi}_{b,-}^{-1}+2\mathrm{i}\omega_2 g^2\right|^2(n_1+1)+4\omega_2^2 g^4 n_1\right] \\ &+g^2\gamma_2\left|\chi_{a,-}\chi_{b,-}\bar{\chi}_{b,-}\right|^2\left(\left|\bar{\chi}_{b,-}^{-1}\right|^2(n_2+1)+\left|\chi_{b,-}^{-1}\right|^2 n_2\right)\ ,\end{aligned}\tag{5.40}$$

$$\begin{aligned}&\int_{-\infty}^{+\infty} \left\langle c^\dagger[\omega+\omega_1]c[\omega'-\omega_1]\right\rangle \mathrm{d}\omega' \\ =&\,\gamma_1 \left|\chi_{a,+}^2\chi_{b,+}\bar{\chi}_{b,+}\right|^2 \left[4\omega_2^2 g^4(n_1+1)+\left|\chi_{a,+}^{-1}\chi_{b,+}^{-1}\bar{\chi}_{b,+}^{-1}-2\mathrm{i}\omega_2 g^2\right|^2 n_1\right] \\ &+g^2\gamma_2\left|\chi_{a,+}\chi_{b,+}\bar{\chi}_{b,+}\right|^2\left(\left|\bar{\chi}_{b,+}^{-1}\right|^2(n_2+1)+\left|\chi_{b,+}^{-1}\right|^2 n_2\right)\ ,\end{aligned}\tag{5.41}$$

$$\begin{aligned}&\int_{-\infty}^{+\infty} \left\langle c^\dagger[\omega+\omega_1]c^\dagger[\omega'+\omega_1]\right\rangle \mathrm{d}\omega' \\ =&\,\gamma_1 \left|\chi_{a,+}^2\chi_{b,+}\bar{\chi}_{b,+}\right|^2 \left(-2\mathrm{i}\omega_2 g^2\right)\times \\ &\left[\left(\chi_{a,+}^{*-1}\chi_{b,+}^{*-1}\bar{\chi}_{b,+}^{*-1}-2\mathrm{i}\omega_2 g^2\right)(n_1+1)+\left(\chi_{a,+}^{-1}\chi_{b,+}^{-1}\bar{\chi}_{b,+}^{-1}-2\mathrm{i}\omega_2 g^2\right)n_1\right] \\ &-g^2\gamma_2\left|\chi_{a,+}\chi_{b,+}\bar{\chi}_{b,+}\right|^2\left(\left|\bar{\chi}_{b,+}^{-1}\right|^2(n_2+1)+\left|\chi_{b,+}^{-1}\right|^2 n_2\right)\ ,\end{aligned}\tag{5.42}$$

where the response functions are

$$\chi_{a,\pm}^{-1} = -\mathrm{i}(\omega \pm \omega_1)+\frac{\gamma_1}{2}\ ,\tag{5.43}$$

$$\chi_{b,\pm}^{-1} = -\mathrm{i}(\omega \pm \omega_1-\omega_2)+\frac{\gamma_2}{2}\ ,\tag{5.44}$$

$$\bar{\chi}_{b,\pm}^{-1} = -\mathrm{i}(\omega \pm \omega_1+\omega_2)+\frac{\gamma_2}{2}\ .\tag{5.45}$$

Finally, the displacement power spectral density is

$$\begin{aligned}
&S_{xx}[\omega] \\
&= \frac{\hbar\gamma_1}{2m\omega_1}\left|\chi_{a,-}^2\chi_{b,-}\bar{\chi}_{b,-}\right|^2 \Bigg\{\left|\chi_{a,-}^{-2}\chi_{b,-}^{-1}\bar{\chi}_{b,-}^{-1} + 2\mathrm{i}\omega_2 g^2\right|^2 (n_1+1) + 4\omega_2^2 g^4 n_1 \\
&+2\mathrm{i}\omega_2 g^2 \left[\left(\chi_{a,-}^{-1}\chi_{b,-}^{-1}\bar{\chi}_{b,-}^{-1} + 2\mathrm{i}\omega_2 g^2\right)(n_1+1) + \left(\chi_{a,-}^{*-1}\chi_{b,-}^{*-1}\bar{\chi}_{b,-}^{*-1} + 2\mathrm{i}\omega_2 g^2\right) n_1\right]\Bigg\} \\
&+ \frac{\hbar\gamma_1}{2m\omega_1}\left|\chi_{a,+}^2\chi_{b,+}\bar{\chi}_{b,+}\right|^2 \Bigg\{\left|\chi_{a,+}^{-2}\chi_{b,+}^{-1}\bar{\chi}_{b,+}^{-1} - 2\mathrm{i}\omega_2 g^2\right|^2 n_1 + 4\omega_2^2 g^4 (n_1+1) \\
&-2\mathrm{i}\omega_2 g^2 \left[\left(\chi_{a,+}^{*-1}\chi_{b,+}^{*-1}\bar{\chi}_{b,+}^{*-1} - 2\mathrm{i}\omega_2 g^2\right)(n_1+1) + \left(\chi_{a,+}^{-1}\chi_{b,+}^{-1}\bar{\chi}_{b,+}^{-1} - 2\mathrm{i}\omega_2 g^2\right) n_1\right]\Bigg\} \ .
\end{aligned} \tag{5.46}$$

For simplicity, we calculate the symmetrized power spectral density

$$\begin{aligned}
\bar{S}_{xx}[\omega] &= \frac{1}{2}\left(S_{xx}[\omega] + S_{xx}[-\omega]\right) \\
&= \frac{\hbar\gamma_1\left(n_1+\frac{1}{2}\right)}{2m\omega_1}\times \\
&\left(\left|\chi_{a,-} + 2\mathrm{i}\omega_2 g^2\chi_{a,-}^2\chi_{b,-}\bar{\chi}_{b,-}\right|^2 + \left|\chi_{a,+} - 2\mathrm{i}\omega_2 g^2\chi_{a,+}^2\chi_{b,+}\bar{\chi}_{b,+}\right|^2\right) \ .
\end{aligned} \tag{5.47}$$

This $\bar{S}_{xx}[\omega]$ can be separated into two parts $\bar{S}_{xx}[\omega] \triangleq \bar{S}_{xx}^{(+)}[\omega] + \bar{S}_{xx}^{(-)}[\omega]$, where

$$\bar{S}_{xx}^{(+)}[\omega] = \frac{\hbar\gamma_1\left(n_1+\frac{1}{2}\right)}{2m\omega_1}\left|\chi_{a,-} + 2\mathrm{i}\omega_2 g^2\chi_{a,-}^2\chi_{b,-}\bar{\chi}_{b,-}\right|^2 \tag{5.48}$$

contains intensity mainly in the positive frequency bands, and

$$\bar{S}_{xx}^{(-)}[\omega] = \frac{\hbar\gamma_1\left(n_1+\frac{1}{2}\right)}{2m\omega_1}\left|\chi_{a,+} - 2\mathrm{i}\omega_2 g^2\chi_{a,+}^2\chi_{b,+}\bar{\chi}_{b,+}\right|^2 \tag{5.49}$$

in the negative bands.

### Peak fitting

Ten points along high-symmetry directions were selected, and their scattering intensity and fitted spectrum at 300 K are shown in Fig. 5.6. Phonon centroids were fitted using the Levenberg–Marquardt nonlinear least square method for multiple Lorentzian functions, giving the fitting parameters listed in Table 5.1. The points near *X* or *K* (see Fig. 5.6c-g), show an extra peak above 20 meV, which is obviously not the highest normal LO phonon branch.

The fitting results were used to estimate the phonon energies and linewidths of the TA (within 7-9 meV) and TO phonons to generate IPS reported in the main manuscript (i.e. $\omega_1$, $\omega_2$, $\gamma_1$, $\gamma_2$) as follows

$$\omega_1 = \left\langle x_{c,1}^{(a)}, x_{c,2}^{(b)}, x_{c,3}^{(c)}, x_{c,3}^{(d)}, x_{c,3}^{(e)}, x_{c,2}^{(f)}, x_{c,3}^{(g)}, x_{c,3}^{(h)}, x_{c,3}^{(i)}, x_{c,3}^{(j)} \right\rangle = 16.97(10)\ \text{meV}\ , \tag{5.50}$$

$$\omega_2 = \left\langle x_{c,1}^{(d)}, x_{c,1}^{(e)}, x_{c,1}^{(g)}, x_{c,2}^{(i)} \right\rangle = 8.2(2)\ \text{meV}\ , \tag{5.51}$$

$$\gamma_1 = \left\langle w_1^{(a)}, w_2^{(b)}, w_3^{(g)}, w_3^{(h)}, w_3^{(i)}, w_3^{(j)} \right\rangle = 3.6(10)\ \text{meV}\ , \tag{5.52}$$

$$\gamma_2 = \left\langle w_1^{(d)}, w_1^{(e)}, w_1^{(g)}, w_2^{(i)} \right\rangle = 3.7(7)\ \text{meV}\ , \tag{5.53}$$

where the notations are consistent with those in Table 5.1. For example, $x_{c,2}^{(i)}$ refers to the frequency center of the second peak in Fig. 5.6i.

Finally, the frequency of the upper IPS ($\omega_\mathrm{G}$) was also calculated

$$\omega_\mathrm{G} = \left\langle x_{c,4}^{(c)}, x_{c,4}^{(d)}, x_{c,4}^{(e)}, x_{c,3}^{(f)}, x_{c,5}^{(g)} \right\rangle = 25.9(5)\ \text{meV}\ , \tag{5.54}$$

satisfying $\omega_1 + \omega_2 \simeq \omega_\mathrm{G}$.

### Coupling Strength Estimation

The coupling strength was calculated by comparing the power intensity between the model derivation and the measurement at 300 K. The ratio can avoid any possible scaling factors. The following ratio was calculated numerically

$$\begin{aligned} &\frac{\bar{S}_{xx}^{(+)}[\omega_1]}{\bar{S}_{xx}^{(+)}[\omega_1+\omega_2]} \\ &= \frac{(\text{Measured Phonon Intensity Peak at } \omega = \omega_1) * n(\omega_1)}{(\text{Measured Phonon Intensity Peak at } \omega = \omega_1+\omega_2) * n(\omega_1+\omega_2) * 2/3}\ . \end{aligned} \tag{5.55}$$

The notations are the same as in the main manuscript, a $2/3$ factor is added because two-thirds of the IPS feature are G-TO phonons, and $n(\omega) = [\exp(\hbar\omega/k_\mathrm{B}T) - 1]^{-1}$ is the Planck distribution function (the thermal weight was corrected when plotting the phonon intensity map). The physics solution corresponds to the one with an observable upper-shifted sideband (AS peak).

Table 5.1: Fitting parameters.

| Peak fitting function: $y = y_0 + \frac{2A}{\pi}\frac{w}{4(x-x_c)^2+w^2}$ | | | | | | | | | | | |
|---|---|---|---|---|---|---|---|---|---|---|---|
| Sub-figure No. in Fig. 5.6 | | a | b | c | d | e | f | g | h | i | j |
| q-point | | [0, 0, 0] | [0, 0, 0.25] | [0, 0, 0.5] | [0, 0, 0.75] | [0, 0, 1] | [0, 0.75, 0.75] | [0, 0.5, 0.5] | [0, 0.25, 0.25] | [0.25, 0.25, 0.25] | [0.5, 0.5, 0.5] |
| Offset, $y_0$ | | 0.0013(3) | -0.00001(6) | -0.0024(2) | -0.0015(2) | -0.0019(2) | -0.0008(2) | -0.0007(3) | -0.0037(5) | -0.0005(3) | -0.0008(3) |
| 1st. peak | Center, $x_{c,1}$ | 16.58(7) | 3.86(4) | 6.05(2) | 7.36(2) | 7.73(3) | 10.33(7) | 8.48(7) | 4.48(7) | 6.09(12) | 9.01(11) |
| | Width, $w_1$ | 2.8(3) | 3.6(2) | 3.57(11) | 3.25(11) | 3.35(11) | 4.7(3) | 3.9(3) | 3.3(3) | 2.5(4) | 3.1(4) |
| | Area, $A_1$ | 0,.038(4) | 0.142(9) | 0.086(3) | 0.077(3) | 0.088(3) | 0.078(5) | 0.045(5) | 0.051(10) | 0.040(9) | 0.045(6) |
| | Height, $H_1$ | 0.010 | 0.025 | 0.013 | 0.014 | 0.015 | 0.010 | 0.007 | 0.006 | 0.010 | 0.009 |
| 2nd. peak | Center, $x_{c,2}$ | 26.3(3) | 16.74(15) | 11.45(10) | 12.37(7) | 11.92(7) | 17.90(9) | 12.18(8) | 7.4(3) | 9.1(2) | 13.52(16) |
| | Width, $w_2$ | 3.8(15) | 3.7(6) | 4.6(4) | 2.5(3) | 2.3(3) | 4.3(3) | 2.8(3) | 6.8(7) | 4.2(7) | 2.6(6) |
| | Area, $A_2$ | 0.012(5) | 0.043(8) | 0.033(3) | 0.018(2) | 0.019(2) | 0.056(4) | 0.022(3) | 0.11(2) | 0.060(12) | 0.034(10) |
| | Height, $H_2$ | 0.002 | 0.007 | 0.005 | 0.005 | 0.005 | 0.008 | 0.005 | 0.010 | 0.009 | 0.008 |
| 3rd. peak | Center, $x_{c,3}$ | - | 25.9(6) | 17.07(5) | 17.40(5) | 17.27(5) | 26.3(3) | 16.90(7) | 16.74(6) | 16.68(12) | 16.40(19) |
| | Width, $w_3$ | - | 7(2) | 3.6(2) | 4.0(2) | 4.8(2) | 6.6(14) | 4.2(3) | 4.4(3) | 3.2(4) | 3.0(6) |
| | Area, $A_3$ | - | 0.030(14) | 0.046(3) | 0.063(3) | 0.088(4) | 0.033(7) | 0.044(4) | 0.049(4) | 0.042(5) | 0.040(10) |
| | Height, $H_3$ | - | 0.003 | 0.008 | 0.010 | 0.012 | 0.003 | 0.007 | 0.007 | 0.008 | 0.008 |
| 4th. peak | Center, $x_{c,4}$ | - | - | 24.8(2) | 26.3(2) | 26.4(2) | - | 21.49(11) | 25.72(14) | 25.6(4) | 25.8(5) |
| | Width, $w_4$ | - | - | 13.6(16) | 9.1(11) | 8.5(12) | - | 2.0(5) | 11.7(10) | 9.5(19) | 12(2) |
| | Area, $A_4$ | - | - | 0.102(14) | 0.058(7) | 0.052(7) | - | 0.008(2) | 0.12(2) | 0.063(13) | 0.096(19) |
| | Height, $H_4$ | - | - | 0.005 | 0.004 | 0.004 | - | 0.003 | 0.007 | 0.004 | 0.005 |
| 5th. peak | Center, $x_{c,5}$ | - | - | - | - | - | - | 25.7(3) | - | - | - |
| | Width, $w_5$ | - | - | - | - | - | - | 7.2(12) | - | - | - |
| | Area, $A_5$ | - | - | - | - | - | - | 0.038(8) | - | - | - |
| | Height, $H_5$ | - | - | - | - | - | - | 0.003 | - | - | - |

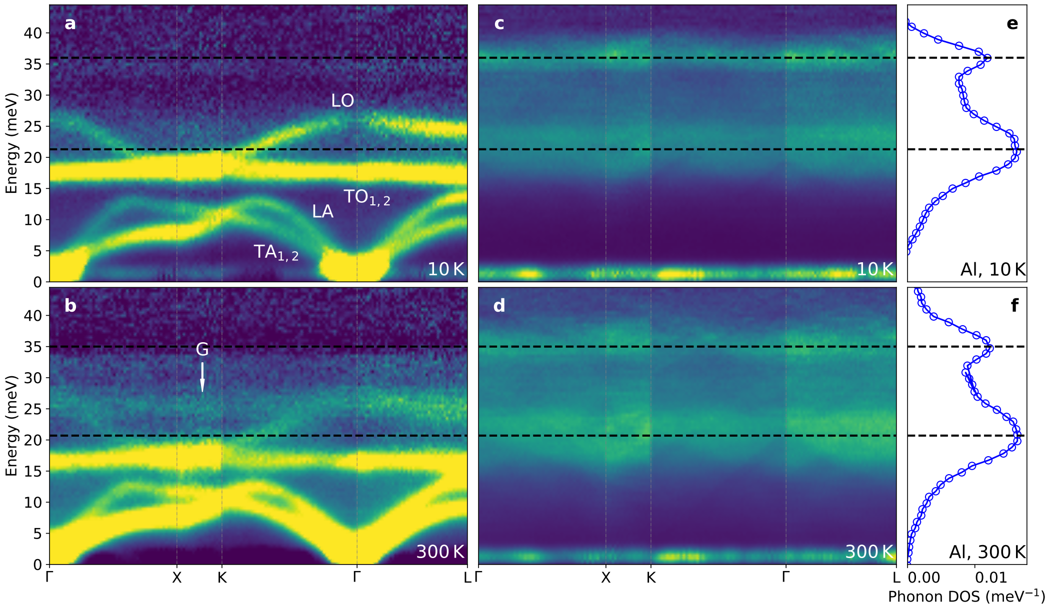

Figure 5.4: Information on background analysis. a-d, 2D slices through the four-dimensional scattering function $S(\mathbf{Q}, \varepsilon)$, where $\varepsilon = \hbar\omega$, along high symmetry lines in the first Brillouin zone, measured at 10 K (a, c) and 300 K (b, d) respectively. a-b are the final results of single crystal NaBr and c-d are the background measurements of the empty aluminum can. Corresponding aluminum phonon DOS from previous measurements [18] are shown in e (10 K) and f (300 K). 'G' refers to the intermodulation phonon sideband.

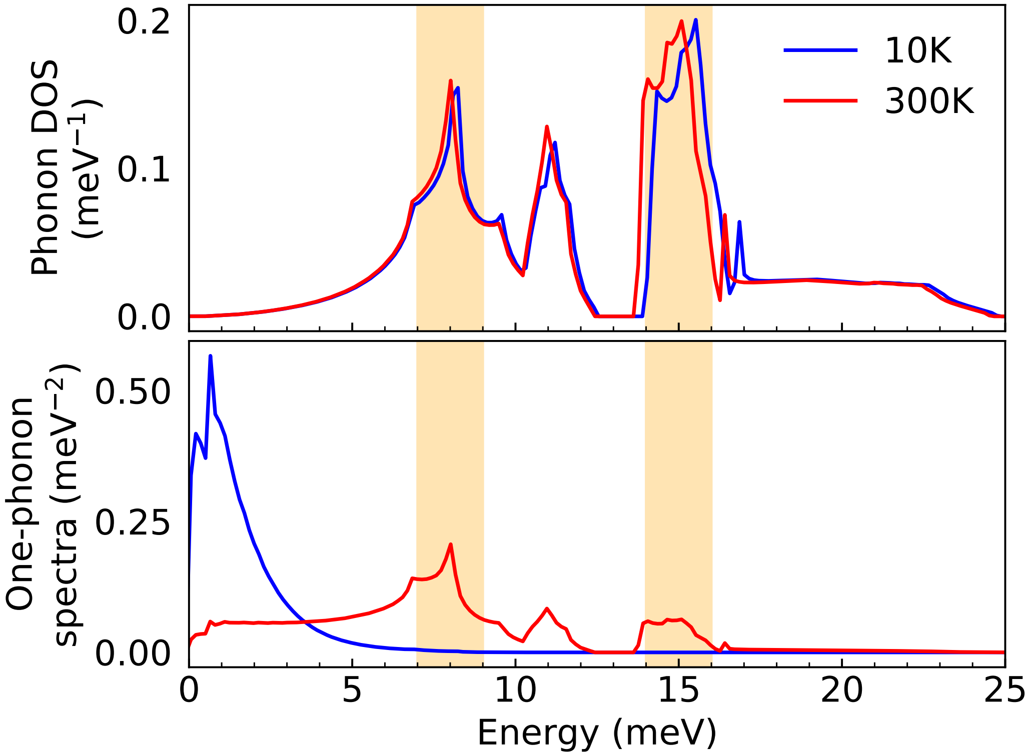

Figure 5.5: Calculated phonon DOS and one-phonon spectra before phonon self-energy corrections. Phonons involved in the three-phonon processes for IPS feature are indicated by the shaded regions. The one-phonon spectra are given by $A_1(\epsilon) = \frac{g(\varepsilon)}{\varepsilon}\frac{1}{e^{\varepsilon/k_\mathrm{B}T}-1}$, where $g(\epsilon)$ is the phonon DOS.

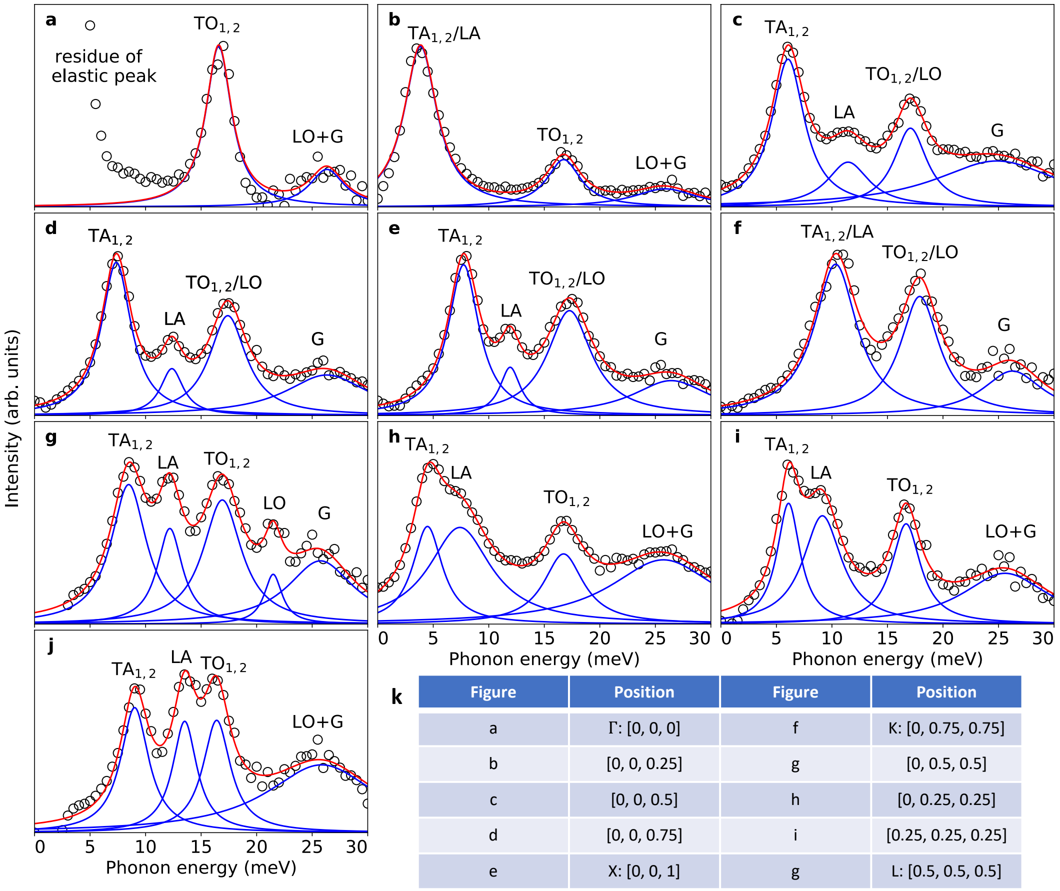

| Figure | Position | Figure | Position |
|---|---|---|---|
| a | Γ: [0, 0, 0] | f | K: [0, 0.75, 0.75] |
| b | [0, 0, 0.25] | g | [0, 0.5, 0.5] |
| c | [0, 0, 0.5] | h | [0, 0.25, 0.25] |
| d | [0, 0, 0.75] | i | [0.25, 0.25, 0.25] |
| e | X: [0, 0, 1] | g | L: [0.5, 0.5, 0.5] |

Figure 5.6: Measured constant $\mathbf{q}$-$S(\mathbf{q}, \epsilon)$ data at ten different points at 300 K. a-j, Measured intensity data are black empty circles. Fitted peaks are in blue, and the cumulative fitting results are in red. k, Table of the $\mathbf{q}$-points corresponding to each sub-figure.

## *Chapter 6*

# FUTURE WORK

### 6.1 Effects of Phonon Anharmonicity on Dielectric Properties

In polar materials, the phonon anharmonicity will certainly affect the dielectric properties of materials, such as the Born effective charges and the dielectric constants, as the long-ranged electrostatics are induced by dipole-dipole interactions. Conventional practice today is to just assume that these values do not change with temperature, calculated with different volumes at 0 K.

Discrepancies, however, can be obvious. As we can see from Fig. 6.1, there is a significant difference between the measured phonons and the computational results at 700 K in NaBr. Could this abnormal phonon behaviors arise from the change in the polar properties of a highly anharmonic phonon system with increasing temperature?

Our initial guess would be that due to the large vibrational amplitude of atomic motions, the dipole-dipole interactions will be weaker and the long-ranged electrostatic

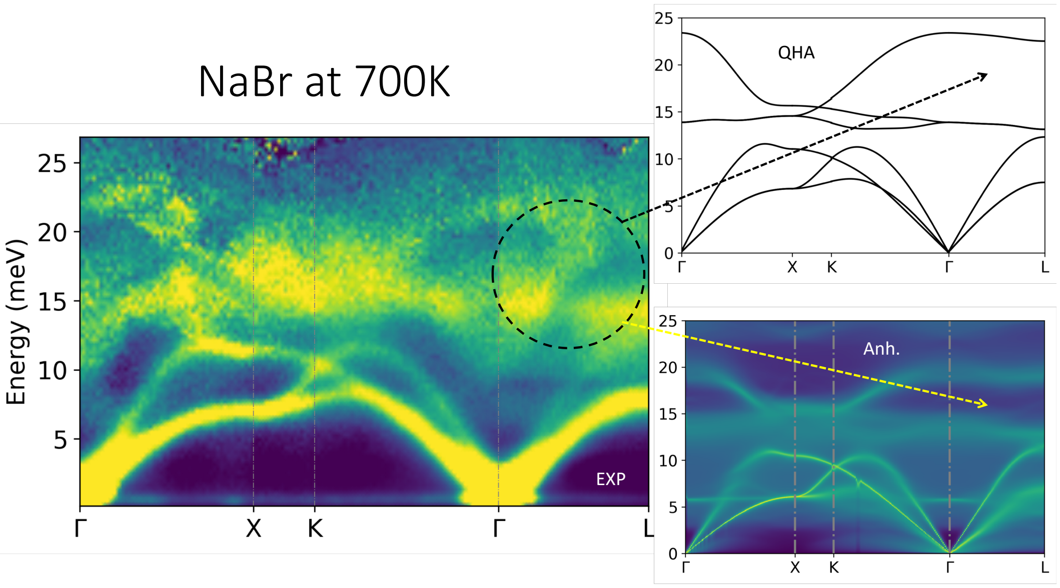

Figure 6.1: Phonons in NaBr at 700 K. The one on the left panel is the experimental result. The one on the upper right panel is the result with QHA, and the one on the lower right panel is the calculated anharmonic phonon lineshape. It is shown that the abnormal feature is not reproduced by either of the computational methods.

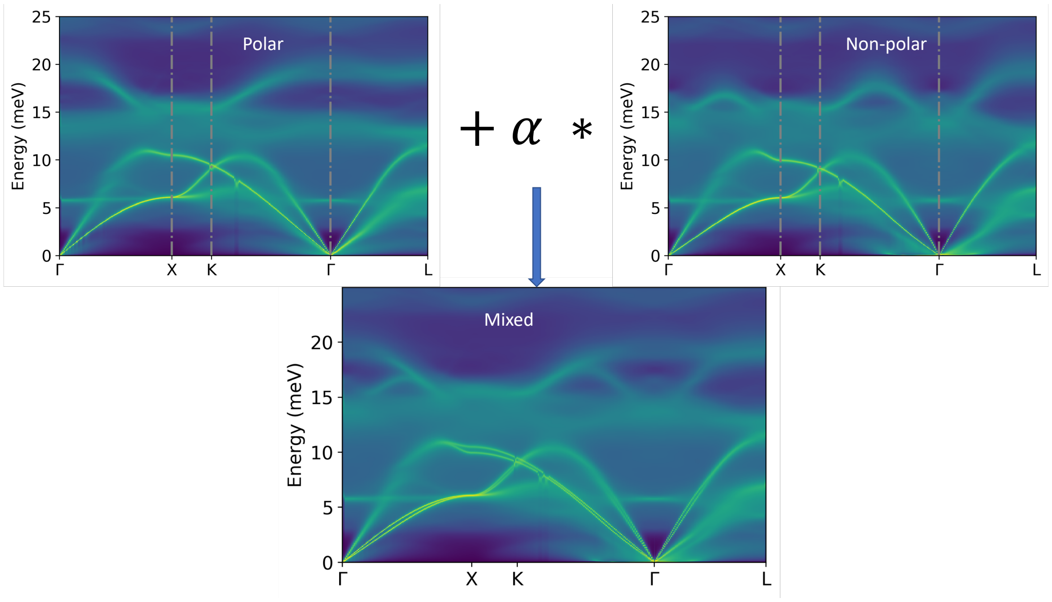

Figure 6.2: Mixed phonon spectral function of NaBr at 700 K when $\alpha = 1$.

interactions will be partially suppressed. As a result, part of atom motions might 'feel' like the non-polar material. The simplest but still informative model would be the linear combination of simulated results of the polar and non-polar (i.e. ignore the long-ranged interactions) material. If we denote the phonon spectral function as $\mathcal{S}$, then the prediction can be written as

$$\mathcal{S}^{\text{high } T} = \frac{\mathcal{S}^{\text{polar}} + \alpha * \mathcal{S}^{\text{non-polar}}}{1+\alpha} , \tag{6.1}$$

where $\alpha$ is the weighting factor in the linear combination process.

Figure 6.2 shows the case when $\alpha = 1$. For this test case, the position of the intersection point between LO-branch-1 (the normal one) and LO-branch-2 (the one goes up along $\Gamma - L$) agrees well. It also captures the main feature along $\Gamma - L$ direction, and might also explain the large broadening between $X - K$. There is some disagreement for the phonon behaviors near the $\Gamma$ point, however. Perhaps the cause is that the non-polar parts are experiencing different basic inter-atomic force constants from the polar ones, as for this simple model the same set of inter-atomic force constants were used, and the only difference was the presence or absence of the correction for the long-range electrostatic interaction. Nevertheless, this model may point the direction towards a more quantitative understanding of polar materials at high temperatures. More physics details still need careful analysis, and this could be an effort in the near future.

## 6.2 Experimental Detection of Localized Phonon Behaviors

Techniques for folding higher Brillouin zones back to the first work well for extracting regular phonon dispersions. If we are interested in phonon behaviors that are seen in specific zones, however, such features will be 'buried' after folding back multiple Brillouin zones. It is also a concern when we aim to study the polarization effects.

In this thesis, any possible localized information has not been fully examined. There could be some interesting features lying in certain Brillouin zones. More work is needed to look into each individually Brillouin zone to see if there is any localized phonon behaviors.

# BIBLIOGRAPHY

[1] A. P. Miiller and B. N. Brockhouse, Phys. Rev. Lett. **20**, 798 (1968).

[2] D. H. Dutton, B. N. Brockhouse, and A. P. Miiller, Canadian Journal of Physics **50**, 2915 (1972).

[3] J. Arblaster, Calphad **19**, 327 (1995).

[4] J. Arblaster, Platinum Metals Review(UK) **40**, 62 (1996).

[5] N. S. Murthy, R. Begum, C. Somanathan, and M. Murthy, Solid State Communications **3**, 113 (1965).

[6] E. Kren and P. Szabo, Physics Letters **11**, 215 (1964).

[7] E. Franus-Muir, E. Fawcett, and V. Pluzhnikov, Solid State Communications **52**, 615 (1984).

[8] A. Menshikov, Y. Dorofeev, G. Budrina, and V. Syromyatnikov, Journal of Magnetism and Magnetic Materials **73**, 211 (1988).

[9] L. M. Corliss, J. M. Hastings, W. Kunnmann, R. Thomas, J. Zhuang, R. Butera, and D. Mukamel, Phys. Rev. B **31**, 4337 (1985).

[10] V. V. Tarasenko, V. Pluzhnikov, and E. Fawcett, Phys. Rev. B **40**, 471 (1989).

[11] C. P. Adams, T. E. Mason, E. Fawcett, A. Z. Menshikov, C. D. Frost, J. B. Forsyth, T. G. Perring, and T. M. Holden, Journal of Physics: Condensed Matter **12**, 8487 (2000).

[12] Y. Shen, C. W. Li, X. Tang, H. L. Smith, and B. Fultz, Phys. Rev. B **93**, 214303 (2016).

[13] E. Havinga, H. Damsma, and P. Hokkeling, Journal of the Less Common Metals **27**, 169 (1972).

[14] V. Deshpande, Acta Cryst. **14**, 794 (1961).

[15] G. K. White, J. G. Collins, and K. A. G. Mendelssohn, Proc. R. Soc. Lond. A **333**, 237 (1973).

[16] J. E. Rapp and H. D. Merchant, J. Appl. Phys. **44**, 3919 (1973).

[17] A. S. M. Rao, K. Narender, K. G. K. Rao, and N. G. Krishna, J. Mod. Phys. **4**, 208 (2013).

[18] X. Tang, C. W. Li, and B. Fultz, Phys. Rev. B **82**, 184301 (2010).

[19] N. Ashcroft and N. Mermin, *Solid State Physics* (Saunders College, Philadelphia, 1976).

[20] C. Kittel, P. McEuen, and P. McEuen, *Introduction to solid state physics* (Wiley New York, 1996).

[21] O. Madelung, *Introduction to solid-state theory* (Springer Science & Business Media, 2012).

[22] B. Fultz, *Phase transitions in materials* (Cambridge University Press, 2020).

[23] O. Hellman, `http://ollehellman.github.io/program/phonon_dispersion_relations.html` (2011), accessed: 2020-05-01.

[24] P. Aynajian, *Electron-phonon interaction in conventional and unconventional superconductors* (Springer Science & Business Media, 2011).

[25] J. Page, Physical Review B **41**, 7835 (1990).

[26] A. Sievers and S. Takeno, Phys. Rev. Lett. **61**, 970 (1988).

[27] A. Dolgov, Fizika Tverdogo Tela **28**, 1641 (1986).

[28] S. A. Teukolsky, B. P. Flannery, W. Press, and W. Vetterling, SMR **693**, 59 (1992).

[29] M. E. Manley, J. W. Lynn, Y. Chen, and G. H. Lander, Phys. Rev. B **77**, 052301 (2008).

[30] K. Sandusky, J. Page, and K. Schmidt, Physical Review B **46**, 6161 (1992).

[31] V. Hizhnyakov, A. Shelkan, M. Klopov, S. Kiselev, and A. Sievers, Physical Review B **73**, 224302 (2006).

[32] E. Kenig, B. A. Malomed, M. C. Cross, and R. Lifshitz, Phys. Rev. E **80**, 046202 (2009).

[33] V. Hizhnyakov, M. Haas, A. Shelkan, and M. Klopov, Physica Scripta **89**, 044003 (2014).

[34] M. E. Manley, A. J. Sievers, J. W. Lynn, S. A. Kiselev, N. I. Agladze, Y. Chen, A. Llobet, and A. Alatas, Phys. Rev. B **79**, 134304 (2009).

[35] M. E. Manley, O. Hellman, N. Shulumba, A. F. May, P. J. Stonaha, J. Lynn, V. O. Garlea, A. Alatas, R. P. Hermann, J. D. Budai, H. Wang, S. B. C, and A. J. Minnich, Nature communications **10**, 1928 (2019).

[36] M. Sato and A. Sievers, Nature **432**, 486 (2004).

[37] A. Nicolaï, P. Delarue, and P. Senet, Scientific reports **5**, 1 (2015).

[38] E. Trias, J. Mazo, and T. Orlando, Physical review letters **84**, 741 (2000).

[39] O. Hellman, I. A. Abrikosov, and S. I. Simak, Phys. Rev. B **84**, 180301 (2011).

[40] O. Hellman, P. Steneteg, I. A. Abrikosov, and S. I. Simak, Phys. Rev. B **87**, 104111 (2013).

[41] O. Hellman and I. A. Abrikosov, Phys. Rev. B **88**, 144301 (2013).

[42] B. Fultz and J. M. Howe, *Transmission electron microscopy and diffractometry of materials* (Springer Science & Business Media, 2013).

[43] D. L. Abernathy, M. B. Stone, M. Loguillo, M. Lucas, O. Delaire, X. Tang, J. Lin, and B. Fultz, Rev. Sci. Instrum. **83**, 015114 (2012).

[44] G. G., *The Electron-Phonon interaction in metals* (North-Holland, Amsterdam, 1981).

[45] D. C. Wallace, *Statistical Physics of Crystals and Liquids* (World Scientific, Singapore, 2003).

[46] D. C. Wallace, *Thermodynamics of crystals* (Wiley, New York, USA, 1998).

[47] N. Bock, D. Coffey, and D. C. Wallace, Phys. Rev. B **72**, 155120 (2005).

[48] X. Tang and B. Fultz, Phys. Rev. B **84**, 054303 (2011).

[49] K. M. Ho, M. L. Cohen, and W. E. Pickett, Phys. Rev. Lett. **41**, 815 (1978).

[50] B. N. Harmon and S. K. Sinha, Phys. Rev. B **16**, 3919 (1977).

[51] P. Allen and J. Hui, Zeitschrift für Physik B Condensed Matter **37**, 33 (1980).

[52] S. M. Shapiro, G. Shirane, and J. D. Axe, Phys. Rev. B **12**, 4899 (1975).

[53] N. Suzuki and M. Otani, Journal of Physics: Condensed Matter **14**, 10869 (2002).

[54] O. Delaire, M. S. Lucas, J. A. Muñoz, M. Kresch, and B. Fultz, Phys. Rev. Lett. **101**, 105504 (2008).

[55] J. A. Muñoz, M. S. Lucas, O. Delaire, M. L. Winterrose, L. Mauger, C. W. Li, A. O. Sheets, M. B. Stone, D. L. Abernathy, Y. Xiao, P. Chow, and B. Fultz, Phys. Rev. Lett. **107**, 115501 (2011).

[56] O. Delaire, K. Marty, M. B. Stone, P. R. C. Kent, M. S. Lucas, D. L. Abernathy, D. Mandrus, and B. C. Sales, Proceedings of the National Academy of Sciences **108**, 4725 (2011).

[57] P. B. Allen, Phys. Rev. B **92**, 064106 (2015).

[58] A. Maradudin and A. E. Fein, Phys. Rev. **128**, 2589 (1962).

[59] R. Cowley, Rep. Prog. Phys. **31**, 123 (1968).

[60] L. D. Lloyd, R. L. Johnston, S. Salhi, and N. T. Wilson, Journal of Materials Chemistry **14**, 1691 (2004).

[61] A. Cowley and B. Woodward, Platinum Metals Review **55**, 98 (2011).

[62] R. Gaita and S. J. Al-Bazi, Talanta **42**, 249 (1995).

[63] I. Y. Sklyadneva, A. Leonardo, P. M. Echenique, S. V. Eremeev, and E. V. Chulkov, Journal of Physics: Condensed Matter **18**, 7923 (2006).

[64] B. Fultz, T. Kelley, J. Lin, J. Lee, O. Delaire, M. Kresch, M. McKerns, and S. H., `https://www.its.caltech.edu/~matsci/btfgrp/Inelastic_Neutron_Book.pdf` (2016), accessed: 2020-05-01.

[65] M. Kresch, M. Lucas, O. Delaire, J. Y. Y. Lin, and B. Fultz, Phys. Rev. B **77**, 024301 (2008).

[66] G. Kresse and J. Furthmüller, Comput. Mater. Sci. **6**, 15 (1996).

[67] G. Kresse and J. Hafner, Phys. Rev. B **47**, 558 (1993).

[68] G. Kresse and J. Furthmüller, Phys. Rev. B **54**, 11169 (1996).

[69] S. Baroni, S. d. Gironcoli, A. D. Corso, and P. Giannozzi, `http://www.pwscf.org` (2001), accessed: 2020-05-01.

[70] A. P. Miiller, Canadian Journal of Physics **53**, 2491 (1975).

[71] M. Palumbo, B. Burton, A. Costa e Silva, B. Fultz, B. Grabowski, G. Grimvall, B. Hallstedt, O. Hellman, B. Lindahl, A. Schneider, P. E. A. Turchi, and W. Xiong, physica status solidi (b) **251**, 14 (2014).

[72] M. Wierzbowska, S. de Gironcoli, and P. Giannozzi, eprint arXiv:cond-mat/0504077 (2005), cond-mat/0504077 .

[73] P. B. Allen, Phys. Rev. B **36**, 2920 (1987).

[74] B. Fultz, Progress in Materials Science **55**, 247 (2010).

[75] Y. Fei, J. Li, K. Hirose, W. Minarik, J. V. Orman, C. Sanloup, W. van Westrenen, T. Komabayashi, and K. ichi Funakoshi, Physics of the Earth and Planetary Interiors **143–144**, 515 (2004), new Developments in High-Pressure Mineral Physics and Applications to the Earth's Interior.

[76] S. Ono, J. P. Brodholt, and G. D. Price, Journal of Physics and Chemistry of Solids **72**, 169 (2011).

[77] P. I. Dorogokupets and A. Dewaele, High Pressure Research **27**, 431 (2007).

[78] M. Yoshihara, R. McLellan, and F. Brotzen, Acta Metallurgica **35**, 775 (1987).

[79] S. Collard and R. McLellan, Acta Metallurgica et Materialia **40**, 699 (1992).

[80] J. Arblaster, Platinum Metals Review **49**, 141 (2005).

[81] J. W. Arblaster, Platinum Metals Review **56** (2012).

[82] O. Eriksson, J. M. Wills, and D. Wallace, Phys. Rev. B **46**, 5221 (1992).

[83] M. Thiessen, International Journal of Thermophysics **7**, 1183 (1986).

[84] P. Steneteg, O. Hellman, O. Y. Vekilova, N. Shulumba, F. Tasnádi, and I. A. Abrikosov, Phys. Rev. B **87**, 094114 (2013).

[85] A. Miiller and B. Brockhouse, Canadian Journal of Physics **49**, 704 (1971).

[86] R. Ohrlich and W. Drexel, in *Neutron Inelastic Scattering Vol. I. Proceedings of a Symposium on Neutron Inelastic Scattering* (1968).

[87] O. Delaire, M. Kresch, J. A. Muñoz, M. S. Lucas, J. Y. Y. Lin, and B. Fultz, Phys. Rev. B **77**, 214112 (2008).

[88] T. R. Mattsson and A. E. Mattsson, Phys. Rev. B **66**, 214110 (2002).

[89] R. Doubble, S. M. Hayden, P. Dai, H. A. Mook, J. R. Thompson, and C. D. Frost, Phys. Rev. Lett. **105**, 027207 (2010).

[90] S. A. Wolf, D. D. Awschalom, R. A. Buhrman, J. M. Daughton, S. von Molnár, M. L. Roukes, A. Y. Chtchelkanova, and D. M. Treger, Science **294**, 1488 (2001).

[91] K. Yasukochi, K. Kanematsu, and T. Ohoyama, Journal of the Physical Society of Japan **16**, 429 (1961).

[92] N. S. Murthy, R. Begum, C. Somanathan, and M. Murthy, Solid State Communications **3**, 113 (1965).

[93] C. Wolverton and V. Ozoliņš, Phys. Rev. Lett. **86**, 5518 (2001).

[94] J. Feldman, L. Boyer, P. Edwardson, and J. Hardy, Phys. Rev. B **40**, 4105 (1983).

[95] O. Arnold, J. C. Bilheux, J. M. Borreguero, A. Buts, S. I. Campbell, L. Chapon, M. Doucet, N. Draper, R. F. Leal, M. A. Gigg, V. E. Lynch, A. Markvardsen, D. J. Mikkelson, R. L. Mikkelson, R. Miller, K. Palmen, P. Parker, G. Passos, T. G. Perring, P. F. Peterson, S. Ren, M. A. Reuter, A. T. Savici, J. W. Taylor, R. J. Taylor, R. Tolchenov, W. Zhou, and J. Zikovsky, Nuclear Inst. and Methods in Physics Research, A **764**, 156 (2014).

[96] getdos, `http://code.google.com/p/getdos` (2011), accessed: 2020-05-01.

[97] R. T. Azuah, L. R. Kneller, Y. Qiu, P. L. W. Tregenna-Piggott, C. M. Brown, J. R. Copley, and R. M. Dimeo, Journal of Research of the National Institute of Standards and Technology **114**, 341 (2009).

[98] A. Chumakov and W. Sturhahn, Hyperfine Interactions **123**, 781 (1999).

[99] W. Sturhahn and V. Kohn, Hyperfine Interactions **123**, 367 (1999).

[100] W. Sturhahn, Hyperfine Interactions **125**, 149 (2000).

[101] G. Kresse and D. Joubert, Phys. Rev. B **59**, 1758 (1999).

[102] J. P. Perdew, K. Burke, and M. Ernzerhof, Phys. Rev. Lett. **77**, 3865 (1996).

[103] A. Togo and I. Tanaka, Scr. Mater. **108**, 1 (2015).

[104] M. S. Lucas, J. A. Muñoz, O. Delaire, N. D. Markovskiy, M. B. Stone, D. L. Abernathy, I. Halevy, L. Mauger, J. B. Keith, M. L. Winterrose, Y. Xiao, M. Lerche, and B. Fultz, Phys. Rev. B **82**, 144306 (2010).

[105] F. C. Yang, O. Hellman, M. S. Lucas, H. L. Smith, C. N. Saunders, Y. Xiao, P. Chow, and B. Fultz, Phys. Rev. B **98**, 024301 (2018).

[106] D. S. Kim, O. Hellman, J. Herriman, H. L. Smith, J. Y. Y. Lin, N. Shulumba, J. L. Niedziela, C. W. Li, D. L. Abernathy, and B. Fultz, Proc. Natl. Acad. Sci. USA **115**, 1992 (2018).

[107] G. E. Grechnev, J. Kubler, and I. V. Svechkarev, Journal of Physics: Condensed Matter **3**, 7199 (1991).

[108] D. S. Kim, H. L. Smith, J. L. Niedziela, C. W. Li, D. L. Abernathy, and B. Fultz, Phys. Rev. B **91**, 014307 (2015).

[109] Z.-K. Liu, Y. Wang, and S. Shang, Sci. Rep. **4**, 7043 (2014).

[110] P. B. Allen, arXiv preprint arXiv:1906.07103 (2019).

[111] R. Mittal, M. Gupta, and S. Chaplot, Prog. Mater. Sci. **92**, 360 (2018).

[112] P. Nath, J. J. Plata, D. Usanmaz, R. A. R. A. Orabi, M. Fornari, M. B. Nardelli, C. Toher, and S. Curtarolo, Comput. Mater. Sci. **125**, 82 (2016).

[113] G. Grimvall, *Thermophysical properties of materials* (Elsevier, North-Holland, Netherlands, 1999).

[114] A. Quong and A. Liu, Phys. Rev. B **56**, 7767 (1997).

[115] K. Zakharchenko, M. Katsnelson, and A. Fasolino, Phys. Rev. Lett. **102**, 046808 (2009).

[116] C. W. Li, X. Tang, J. A. Muñoz, J. B. Keith, S. J. Tracy, D. L. Abernathy, and B. Fultz, Phys. Rev. Lett. **107**, 195504 (2011).

[117] A. Erba, M. Shahrokhi, R. Moradian, and R. Dovesi, J. Chem. Phys. **142**, 044114 (2015).

[118] V. Mitskevich, Sov. Phys. Solid State **3**, 2202 (1962).

[119] E. Cowley and R. A. Cowley, P. Roy. Soc. **287**, 259 (1965).

[120] R. Ewings, A. Buts, M. Le, J. van Duijn, I. Bustinduy, and T. Perring, Nucl. Instrum. Methods Phys. Res. A **834**, 132 (2016).

[121] C. W. Li, O. Hellman, J. Ma, A. F. May, H. B. Cao, X. Chen, A. D. Christianson, G. Ehlers, D. J. Singh, B. C. Sales, and O. Delaire, Phys. Rev. Lett. **112**, 175501 (2014).

[122] G. Kresse and J. Hafner, Phys. Rev. B **49**, 14251 (1994).

[123] V. Popescu and A. Zunger, Phys. Rev. B **85**, 085201 (2012).

[124] I. Errea, M. Calandra, and F. Mauri, Phys. Rev. B **89**, 064302 (2014).

[125] R. A. Cowley, Proc. Phys. Soc. **90**, 1127 (1967).

[126] J. A. Reissland, *The physics of phonons* (John Wiley and Sons, New York, 1973).

[127] O. L. Anderson, Phys. Rev. **144**, 553 (1966).

[128] Y. Sato-Sorensen, J. Geophys. Res. Solid Earth **88**, 3543 (1983).

[129] V. F. Sears, Phys. Rev. A **7**, 340 (1973).

[130] M. Gajdoš, K. Hummer, G. Kresse, J. Furthmüller, and F. Bechstedt, Phys. Rev. B **73**, 045112 (2006).

[131] X. Gonze and C. Lee, Phys. Rev. B **55**, 10355 (1997).

[132] P. M. Chaikin and T. C. Lubensky, *Principles of condensed matter physics* (Cambridge Univ. Press, Cambridge, UK, 1995).

[133] J. M. Ziman, *Electrons and phonons: the theory of transport phenomena in solids* (Oxford Univ. Press, Oxford, UK, 2001).

[134] M. E. Manley, D. L. Abernathy, N. Agladze, and A. J. Sievers, Sci. Rep. **1**, 4 (2011).

[135] M. Kempa, P. Ondrejkovic, P. Bourges, P. Marton, and J. Hlinka, Phys. Rev. B **89**, 054308 (2014).

[136] S. Pailhès, H. Euchner, V. M. Giordano, R. Debord, A. Assy, S. Gomès, A. Bosak, D. Machon, S. Paschen, and M. de Boissieu, Phys. Rev. Lett. **113**, 025506 (2014).

[137] M. E. Manley, J. W. Lynn, D. Abernathy, E. Specht, O. Delaire, A. Bishop, R. Sahul, and J. Budai, Nat. Commun. **5**, 3683 (2014).

[138] A. Rivière, S. Lepri, D. Colognesi, and F. Piazza, Phys. Rev. B **99**, 024307 (2019).

[139] A. A. Clerk, M. H. Devoret, S. M. Girvin, F. Marquardt, and R. J. Schoelkopf, Rev. Mod. Phys. **82**, 1155 (2010).

[140] T. J. Kippenberg and K. J. Vahala, Science **321**, 1172 (2008).

[141] K. Vahala, M. Herrmann, S. Knünz, V. Batteiger, G. Saathoff, T. Hänsch, and T. Udem, Nat. Phys. **5**, 682 (2009).

[142] J. Chan, T. M. Alegre, A. H. Safavi-Naeini, J. T. Hill, A. Krause, S. Gröblacher, M. Aspelmeyer, and O. Painter, Nature **478**, 89 (2011).

[143] F. Benz, M. K. Schmidt, A. Dreismann, R. Chikkaraddy, Y. Zhang, A. Demetriadou, C. Carnegie, H. Ohadi, B. de Nijs, R. Esteban, J. Aizpurua, and J. J. Baumberg, Science **354**, 726 (2016).

[144] R. Riedinger, S. Hong, R. A. Norte, J. A. Slater, J. Shang, A. G. Krause, V. Anant, M. Aspelmeyer, and S. Gröblacher, Nature **530**, 313 (2016).

[145] W. Renninger, P. Kharel, R. Behunin, and P. Rakich, Nat. Phys. **14**, 601 (2018).

[146] A. Tavernarakis, A. Stavrinadis, A. Nowak, I. Tsioutsios, A. Bachtold, and P. Verlot, Nat. Commun. **9**, 662 (2018).

[147] T. E. Markland and M. Ceriotti, Nature Reviews Chemistry **2**, 0109 (2018).

[148] N. Shulumba, O. Hellman, and A. J. Minnich, Phys. Rev. B **95**, 014302 (2017).

[149] Y. Shen, C. Saunders, C. Bernal, D. Abernathy, M. Manley, and B. Fultz, arXiv preprint arXiv:1909.03150 (2019).

[150] C. W. Gardiner and M. J. Collett, Phys. Rev. A **31**, 3761 (1985).